TRANSIENT INTRA- AND EXTRA-CELLULAR THERMOMETRY AS PROBES OF THERMOGENESIS

BY

MANJUNATH CHINNAPPAMUDALIAR RAJAGOPAL

DISSERTATION

Submitted in partial fulfillment of the requirements
for the degree of Doctor of Philosophy in Mechanical Engineering
in the Graduate College of the
University of Illinois at Urbana-Champaign, 2020

Urbana, Illinois

Doctoral Committee:

Associate Professor Sanjiv Sinha, Chair and Director of Research
Professor Rhanor Gillette
Associate Professor Daniel Llano
Professor Placid Ferreira

ABSTRACT

Temperature is a fundamental thermodynamic property affecting every biochemical reaction in cellular milieu. Thermometry in tissues has proven useful in understanding thermoregulatory neuronal circuits and cancer metabolism. In contrast, intracellular temperature changes are relatively less explored. Theoretical temperature changes in intracellular organelles are widely debated, due to lack of understanding of intracellular thermal resistances. There is thus a need for thermometry techniques that can probe within a cell. Such intracellular thermometry can inform theory, and more importantly, provide insight into the role of temperature as a physiological parameter in intracellular studies.

In this work, we describe an intracellular thermometry technique developed using silicon-based microelectromechanical techniques. We fabricated a 5 μm wide micro-thermocouple probe that has a calibration accuracy of 1% and a time constant of 32 μs. Through this probe, we measured transient temperature changes during stimulated mitochondrial proton uncoupling in neurons of *Aplysia californica*. We find that a transient proton motive force dissipation is more dominant than steady-state substrate oxidation in stimulated thermogenesis. Our measurements demonstrate the utility of transient intracellular thermometry in better understanding the thermochemistry of stimulated mitochondrial metabolism.

Using insights from intracellular thermometry, we theoretically examine the validity of thermal conductivity approximation and find that the thermal interfacial resistances might dominate in the sub-cellular region. We develop a generalized thermal resistance network model to analyze cellular-level temperature changes. We find that intracellular temperature changes could be useful to probe stimulated transient biochemical reactions that can produce higher intracellular temperatures, which may not occur endogenously. On the other hand, to probe endogenously thermogenic reactions, we find extracellular thermometry to be better suited, especially at length-scales > 1 cm, such as tissues or organs. To this end, we develop a wireless temperature measurement technique using magnetostriction based sensors that can potentially measure temperatures at tissues length-scales remotely. We identify material properties that influence temperature sensitivity and demonstrate a 5-fold improvement through optimal selection. We further develop techniques that reduce instrument complexity and discuss ways to miniaturize wireless sensors. Overall, this work advances intra- and extra-cellular thermometry techniques that potentially provide unprecedented insight into thermogenesis in cells.

ACKNOWLEDGEMENTS

This dissertation is an outcome of the efforts, love, and support from the people I am surrounded by. First and foremost, I am grateful to Prof. Sanjiv Sinha for giving me the flexibility and for trusting me to shape my dissertation work. Throughout this dissertation work, there were several failed attempts and months of standstills. In such difficult times, Sanjiv's support and his can-do attitude unarguably helped me move forward and take up new challenges. His attention-to-details, constructive criticism, and ability to convey complex scientific arguments in a clear and elegant style continue to inspire me and make me a better researcher.

I was truly fortunate to have met and worked with Dr. Jeffrey Brown. He was instrumental in setting up simultaneous thermometry and electrophysiology measurements. His scientific curiosity and dedication, especially during the initial and uncertain times, made this work possible. I would like to thank Prof. Rhanor Gillette for letting us use his lab for all the experiments. Over the years, Rhanor's curiosity and cheerful attitude have rubbed off on me positively. Prof. Daniel Llano's timely guidance and constructive criticism have helped me shape a better part of this dissertation work. Prof. Placid Ferreira's suggestions on fabrication techniques were invaluable in making the intracellular probe. I would like to thank Prof. Jonathan Sweedler and his group members Dr. Stanislav Rubakhin, Dr. Kevin Clark, and Dr. Ran Chen for providing me *Aplysia* neurons for several experiments. I would like to acknowledge the research funding sources, especially NSF, for funding this work, and the University of Illinois for providing a conducive and collaborative research environment.

Most of my fabrication skills were diligently taught to me by Krishna Valavala and Jun Ma. The office conversations and Jerusalem lunches I had with them and Dhruv Gelda helped me accustom to grad life and research. Dhruv has been my go-to person for discussing personal and professional issues since he has the knack of making anything sound hilarious. I am grateful to my colleagues Amulya and Rifat for taking over some of my work. I also cherish the time with the rest of the group members – Arpit, Akhilesh, Gowtham, Adreet, Daniel, Tim, Shuvankar, for all the group outings we have had. Beyond my colleagues, the vast social circle I was fortunate to be a part of at Champaign-Urbana helped me balance my work life. Special mentions to Shreyas, Kalyan, Nitin, and Vishaal for our memorable adventures together.

Last but not least, I am indebted to my loving wife – Rhinithaa, my parents and sister, who have all been immensely supportive through thick and thin.

To my family

TABLE OF CONTENTS

LIST OF FIGURES

CHAPTER 1

INTRODUCTION

Biochemical reactions are highly sensitive to the conditions in the cellular milieu. This includes temperature, concentration of ions, dopamine, pH, etc. – of which, temperature has been the primary focus on recent clinical studies [1]. The temperature difference between the arterial blood and the brain is as small as 200 mK [2] for complete removal of all metabolic heat from the brain. The presence of such small temperature gradients over large distances within the brain is essential for its functional activities. For instance, the degradation of memory encoding starts at 36.7°C, which is the normal body temperature, and goes up by 70% at a temperature of 34-35°C [3]. The apparent sensitivity to temperatures in the brain originates from the reactions at the intracellular level in the neurons. To understand the physiology of such reactions, there is a growing interest [4]–[6] in the measurements of intracellular temperatures in neurons. Given the temperature sensitivity of biochemical reactions in neurons, there is also a growing interest [7]–[12] in understanding the origin of mitochondrial thermogenesis, which helps to maintain the temperatures throughout the body, especially when in a cold environment.

In this work, we first developed an intracellular temperature measurement platform to measure and understand mitochondrial thermogenesis under stimulated conditions. We then experimentally observe and theoretically analyse heat release in cells during physiological conditions. We explored different thermometry techniques and their suitability for a given biochemical pathway. We found that intracellular transient thermometry under stimulated conditions and extracellular tissue-scale thermometry could provide useful physiological information. To this end, we develop a remote temperature measurement technique for centimetre length-scales using magnetostriction-based sensors, which we show to have the potential to measure tissue-scale temperatures. This chapter is organized as follows. In Section 1.1, we describe the two highly energy-intensive cellular biochemical processes, which form the motivation for this work. We describe the existing literature and highlight the open questions, which we address through this work. In Section 1.2, we discuss the challenges in measuring temperatures at cellular length-

scales. We also highlight the need to theoretically explore the expected temperature changes at cellular and tissue length-scales. In Section 1.3, we describe the overall organization of this thesis.

1.1 Energy-intensive cellular processes

At the cellular level, temperature changes are expressed in every reaction that is either endothermic or exothermic in nature. For instance, a series of endothermic reactions are activated in cells exposed to high temperatures [13]. They can alter gene expressions and activate ion channels, which propagate information to outer environments regarding the temperature increase [14]. On the other hand, to sustain cold environments, for instance, exothermic non-shivering thermogenesis is triggered at mitochondria [11] to produce heat. Here, we discuss two such biochemical reactions that are energy intensive. In Section 1.1.1, we discuss the biochemical reactions related to aerobic respiration that governs mitochondrial thermogenesis. In Section 1.1.2, we discuss the thermodynamics of action potential generation in neurons.

1.1.1 Aerobic respiration

Aerobic respiration is one of the dominant heat-releasing cellular processes that involve the breakdown of glucose to form CO_2, water, and the energy currency ATP. The entire sequence of reactions can be summed up as [15], [16],

$$C_6H_{12}O_6 + 6O_2 + nADP + nP_i \rightarrow 6\,CO_2 + 6\,H_2O + nATP$$

The free energy change (ΔG) during this reaction is ~2870 kJ/mol, and the enthalpy change (ΔH) is ~2808 kJ/mol. The number of ATP produced (n) is theoretically ~38 per glucose molecule [15]; however, due to losses during transport of pyruvates, ADP, etc., the practical yield is around 30 ATP per glucose [16]. Production of ATP typically consumes 41% of the total energy released from glucose oxidation. The remaining ~ 57% (~1635 kJ/mol) of free energy change is released directly as heat [15].

The sequence of glucose breakdown involves glycolysis, tricarboxylic acid (TCA) cycle, and oxidative phosphorylation [17] as shown in Figure 1.1. Roughly, the number of ATPs produced is 2 from glycolysis, 2 from the TCA cycle, and 34 from the electron transport chain. A significant portion of ATP production takes place at mitochondria (as also evident in Figure 1.1). Sugars enter mitochondria as pyruvates, which are formed from glycolysis in the cytosol [17]. Pyruvates undergo

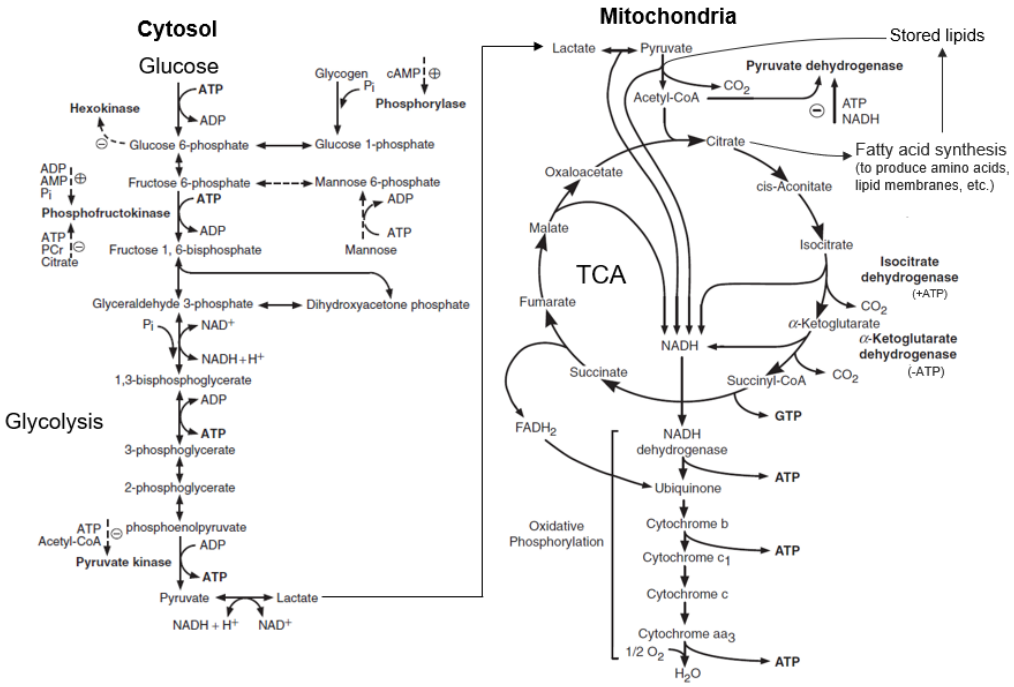

Figure 1.1: Schematic of the biochemical reactions associated with aerobic respiration. Adapted with permission from Ref.[17]

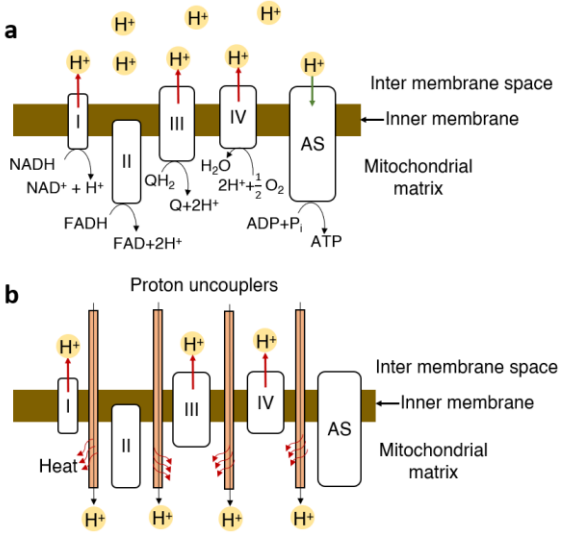

Figure 1.2 a). A schematic of the mitochondrial respiratory chain shows three protein complexes (I, III, IV) producing an H^+ gradient across the inner mitochondrial membrane. ATP synthase (AS) utilizes this H^+ gradient to synthesize ATP from ADP. b) Proton uncouplers allow diffusion of protons through the mitochondrial membrane.

TCA to form NADH, FADH2, and GTP. Through a series of subsequent enzymatic steps, ATPs are produced at the mitochondrial membrane.

Mitochondrial inner membrane houses the electron transport chain and oxidative phosphorylation as shown in Figure 1.2. Complexes I, III, and IV are powered by an electron transport chain. They expel protons across the mitochondrial membrane, maintaining a proton motive force of ~200 mV [18], which is required for ATP synthase (AS) to produce ATP (Figure 1.2a). ATP production consumes energy in the form of a proton gradient built up across the mitochondrial membrane. It is widely known that uncoupling proteins (UCP) dissipate the proton gradient, and convert the energy required to produce ATP as heat [9], [12]. Proton uncouplers like BAM15, FCCP, and CCCP are also known to uncouple protons from ATP synthase [19]. By uncoupling oxidative phosphorylation, aerobic respiration produces more heat and no ATP at the mitochondrial membrane (Figure 1.2b). During this uncoupling process, we would like to emphasize two separate mechanisms that generate heat: (1) proton motive force (pmf) dissipation, and (2) aerobic respiration without ATP production. By probing the transient intracellular temperature changes during the uncoupling process, we can predict the relative contributions and the thermal time constant of these reactions [20].

Previous reports typically probed heat release over longer time scales (~5 min or more) after mitochondrial proton uncoupling. Okabe et al [21] measured about ~ 1.02 K increase in average mitochondrial temperatures, 30 mins after stimulating COS7 cells (monkey kidney cells) through the proton uncoupler FCCP. Kiyonaka et al [22] reported a ~7 K rise, which was sustained for 10 min after stimulating proton uncoupling in HeLa cells through CCCP. Tsuji et al [23] reported up to a ~3 K rise by the end of 30 min after supplying FCCP to brown adipocytes. Tanimoto et al [4] reported a ~7 K rise in neurons and the temperature rise was sustained for 5 min after supplying CCCP. Sato et al [7] measured up to ~0.4 K, at ~120 min after norepinephrine stimulation of brown adipose cells. Further, most of the previous work does not report the temperatures to go back to room temperature, suggesting that the temperature rises are indefinite, which is theoretically implausible [24]. By probing longer time scales in the order of minutes, previous reports potentially measured the heat release from steady aerobic respiration [19] without ATP production due to proton uncoupling. On the other hand, the process of proton uncoupling itself could produce heat [9] while the proton shuttles back to the mitochondrial matrix (Figure 1.2b), and this typically lasts <1 s [20], [25].

In this work, in Chapter 3, we probe the transients (~sub-second) in intracellular temperatures during proton uncoupling to identify the component of heat due to proton currents.

1.1.2 Action potential

The presence of small temperature gradients over large distances within the brain is essential for its functional activities. For instance, a recent MRSI scan of the brain temperature map [26] shows a maximum temperature difference of around 3 K between the frontal and parietal lobes. Moreover, small temperature gradients at the axon terminals of neurons have been understood to influence pre- and post-synaptic events [12], [27]. Any external disturbances can lead to coupled changes in temperature, ion concentrations, and the resulting action potentials. Subsequently, several studies [28]–[35] attempted to measure and understand the coupling between temperature and the ions being transport during action potential generation in a single neuron.

The resting potential of a neuron is typically about -60 to -70 mV as shown in Figure 1.3. An action potential is initiated by a stimulus, typically a nearby depolarization of the membrane. Due to the local depolarization, when the membrane potential reaches about -55 mV, several Na^+ voltage-gated channels are activated to open. Na^+ ions entering the cell increases the membrane potential and makes it less negative. As a result, more Na^+ voltage-gated ion channels open, depolarizing the neuron further until the membrane potential reaches about 40 mV. The Na^+ ion channels then close due to a timed deactivation, which reduces the influx of Na^+. In a delayed response to the original stimulus, the K^+ voltage-gated channels open to expel K^+ ions to the extracellular region. The K^+ ions diffuse out reducing the membrane potential. The K^+ ion channels briefly hyperpolarize the membrane potential before deactivation. Finally, the Na^+/K^+-ATPase ion pump transports the Na^+ ions out of the cell and K^+ ions into the cell to restore the resting membrane potential.

Energy changes during an action potential propagation can be generally written as:

$$\frac{dU}{dt} = C_m \frac{dV_m}{dt} + \sum\nolimits_{i=ions} g_i (V_m - E_i)^2 + \frac{d\phi_{wave}}{dt} + \frac{dQ_{Na/K}}{dt} \qquad (1)$$

where, C_m is the membrane capacitance, V_m is the membrane potential, g_i is the conductance of ion (i), E_i is the Nernst potential of ion (i). The first two

components correspond to the Hodgkin-Huxley model [36], which was originally derived for action potential propagation in squid axon. Capacitive energy changes are reversible, while the Joule heating component produces irreversible dissipation of energy. Further, the capacitive component of energy changes is expected to be an order of magnitude lower than that of Joule heating [33]. The heat $Q_{Na/K}$ corresponds to the heat released or absorbed by the Na^+/K^+-ATPase pump that restores the ion balance toward the end of an action potential. The mechanical component (ϕ_{wave}) has been previously modelled under different assumptions

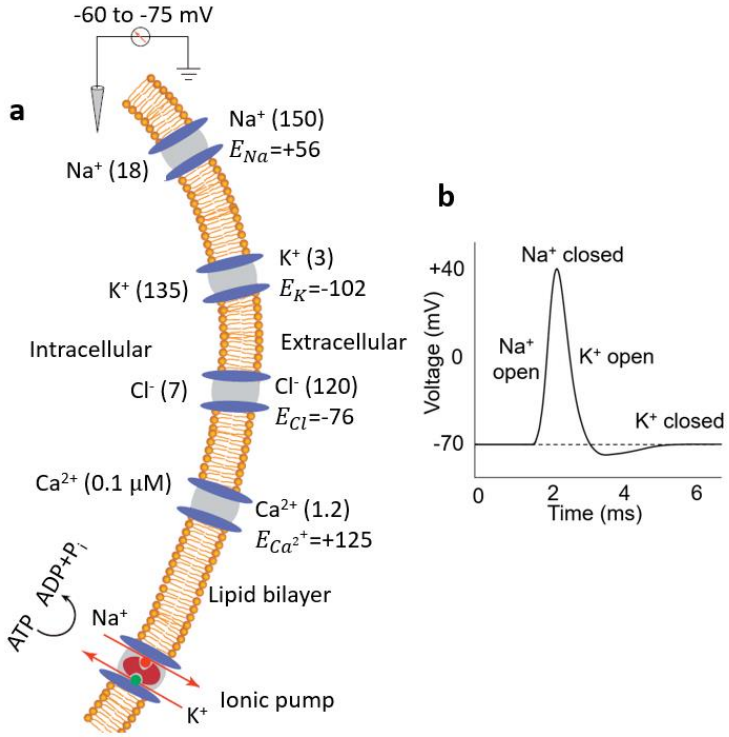

Figure 1.3. a) Schematic of the ion channels at the cell membrane of a neuron. Concentrations (in millimoles except that for intracellular Ca^{2+}) of the ions are given in parentheses; their Nernst potentials (E) for a typical mammalian neuron are indicated. Figure adapted with permission from Ref.[17]. b) A typical action potential voltage response is plotted

ranging from the action potential to be a nonlinear soliton excitation [37], [38], to a self-sustaining electromechanical excitation [39], and as a propagating axoplasmic pressure pulse [6]. Recently, Hady and Machta [6] reported a minimalistic mechanical model consisting of a surface wave propagation, in which the mechanical heat release was estimated as $T\alpha\kappa\big(l(z)+h(z)\big)$. T is the

temperature of the action potential, α is the thermal expansion coefficient, κ is the bulk modulus of the membrane, l and h are the length and height fields along the z direction of an axon. This surface wave model predicts an initial heat dissipation followed by partial heat absorption, resulting in a net positive heat release. The expected heat release rate for neurons of size 50 μm to 500 μm in diameter is about 0.1 nW to 10 nW, based on the predictions of Hady and Machta [6]. Correspondingly, the expected temperature changes are in the order of 10^{-5} K to 10^{-3} K, for isolated neurons in saline. Experimentally measuring such small temperature changes (μK to mK range) over few milli-seconds is challenging as explained below.

Previous experimental studies [28], [29], [31], [34], [35], [40] that report temperature changes during an action potential typically use a PVDF pyroelectric sensor, or stacked thermocouple bed (thermopile) to measure temperature changes. They typically used bundles of nerve fibers or multiple ganglia in an oxygen-filled chamber instead of saline to increase sensitivity to temperature changes. Such studies [28], [29], [31], [34], [35], [40] report temperature changes in the order of 10^{-6} K over few milli-seconds of an action potential. Although the measured temperature changes may seem to be in the range of theoretical predictions, the validity of the experimentally reported temperatures (which are in the order of 10^{-6} K) needs to be carefully examined. The state-of-the-art thermometry [41], as of writing this work, can measure temperature changes in the order of 240×10^{-6} K (corresponding sensitivity to heat is 0.2 nW), with a time constant of ~10 s. Such state-of-the-art thermometry techniques [41], [42] utilize multiple vacuum chambers to isolate the cell from surrounding ambient temperature fluctuations. In comparison, the previous reports used rudimentary techniques (such as calibration using a water bucket [29], bare uninsulated thermocouple probes [28], etc.) to measure the temperature changes during an action potential. The reported temperature changes [28], [29], [31], [34], [35], [40] of 10^{-6} K over 1-10 ms may very well be a result of external sources of errors such as ambient temperature changes, common-mode noise [43], etc. Despite the potential inaccuracies in temperature measurements, previous reports of temperature changes in garfish olfactory nerves or squid axons do not have a consensus [32], [44] on the temperature characteristics during action potential propagation in the axon. Some of the studies report a net positive heat release [28], [45], whereas some of the other studies report no net heat release [30], and others report a net heat absorption [35] during the action potential. Overall, there are several theories [6], [32], [33], [36] proposed for the thermodynamics of action potentials; however, previous

experimental temperature measurements [28], [29], [31], [34], [35], [40] are not significant enough to validate any of the proposed theories.

In this work, we experimentally attempt to measure the temperature changes during an action potential of a single neuron, which we explain in Appendix B. We accumulated data from >20,000 action potentials. By statistical averaging, we find that the temperature changes during an action potential are possibly < 5 mK during an action potential and the ambient noise (of ~30 dB) in the measurements potentially obscured our results. We therefore theoretically explore (in Chapter 4) the physiological temperature changes to find the length- and time-scales at which temperature measurement could potentially be a useful tool in understanding the biochemical reactions in biological systems. We briefly explain it in the next section.

1.2 Challenges in measuring temperature changes in biological systems

Temperature is a fundamental thermodynamic property, which governs all biochemical reactions. This also makes temperature a physiological parameter of interest to be measured. However, the temperature changes during a biochemical reaction may not always be measurable by a sensor. Specifically, the temperature measurability is dependent on the following: the length-scale (cellular vs tissues), the time-scale, and whether the biochemical reaction is endogenous or stimulated.

Under physiological and endogenous conditions, as discussed in the previous section for instance, the expected temperature changes during an action potential could be in the range of 10^{-5} K to 10^{-3} K over a few milliseconds. Such sub-mK temperature changes are not measurable over a few ms even using state-of-the-art thermometry [41], [46], mostly because the room temperature fluctuations dominate the measurement. Similarly, under physiological and unstimulated conditions, aerobic respiration is expected to result in 1- 2 mK of temperature change in an isolated cell due to 0.1-5 nW of heat [41]. Such temperature changes (~few mK) are only measurable through thermal isolation via multiple vacuum chambers, to reduce ambient temperature fluctuations [41], [42]. While the temperature changes due to aerobic respiration are only 1- 5 mK in an isolated cell, the temperature changes amplify with the number of cells reaching up to 1 K in a tissue of ~2 cm in size (discussed in Chapter 4). Such temperature changes in the order of 1 K are readily measurable and have previously proven

useful in understanding thermoregulatory neuronal circuits [47], [48], and cancer metabolism [49]–[52]. Since temperature measurements at tissues can provide useful physiological information, we develop a wireless temperature measurement technique for tissue-scale temperature sensing in Chapter 5. Overall, under endogenous conditions, temperature could be a useful and measurable physiological parameter, especially at larger length scales (> 1 cm) such as tissues or organs.

Certain biochemical reactions can be stimulated to produce higher temperatures that may not otherwise occur endogenously. For instance, mitochondrial thermogenesis can be stimulated by shuttling the protons into the mitochondrial matrix through chemical proton uncouplers [53]. Chemical proton uncouplers such as BAM15, CCCP, or FCCP can induce a drastic reduction in mitochondrial membrane potential [19], [54], [55] unlike the endogenous uncoupling proteins or UCPs. During the proton uncoupling process, we discussed in section 1.1 that heat could be released due to two sources: (1) proton currents (2) aerobic respiration without ATP synthesis. The former is expected to occur over < 1 s [20], [25], while the latter can be prolonged over a few minutes [19]. Previous reports [4], [7], [21], [22] typically probed longer time-scales in the order of 5 min or more and observed >1 K temperature change in isolated cells. Baffou et al [24] suggested that a transient response of 1 K rise over 1 s exceeds the typical glucose content in a cell by a factor of 10^1-10^2. Critics [56], [57] have pointed out incorrect values of cell thermal conductivity, glucose content, and length scale of heat sources in Baffou et al's work that potentially underestimated the temperature rise by 10^2- 10^3. In Chapter 4, we theoretically explore the validity of using an effective thermal conductivity at cellular length-scales and find that thermal interfacial resistances might dominate instead. Further, Baffou et al ignored the contribution of proton current to the overall heat release [9], [20]. Nonetheless, previous intracellular thermometry studies [4], [21], [23], [58]–[61] report a temperature rise for 5 min or more. In some studies [4], [21], [23], [58], [59], [61], the temperatures rises after proton uncoupling were never reported to go back to room temperatures. Such indefinite temperature changes could potentially be from non-specific signals like changes in pH, ion concentrations [24], cell micro-viscosity [62], illumination intensity [63], etc. that do not represent actual temperature changes. Therefore, the existing studies have not been able to identify the heat sources during mitochondrial proton uncoupling, despite stimulation by external proton uncouplers. In this work, in Chapter 2, we develop a chemically inert intracellular thermocouple probe [46], which we use during mitochondrial proton uncoupling to identify the heat

component from proton currents (as discussed in Chapter 3, [20]). We were able to measure the temperature changes during mitochondrial thermogenesis due to the use of an external proton coupler, which otherwise may not happen endogenously to the same extent. We show in Chapter 4 that only under stimulated conditions, the temperature changes inside a single cell can reach measurable limits (~ few K).

1.3 Thesis organization

The rest of the chapters in this thesis are organized as follows:

In Chapter 2, we develop an intracellular thermometry technique by fabricating a micro-thermocouple probe. We use silicon-based microelectromechanical techniques to fabricate a suspended thermocouple probe on a silicon nitride platform, which is chemically inert and biologically compatible. We also highlight our calibration technique that utilizes on-chip solid-state calibration to achieve ~1% calibration accuracy.

In Chapter 3, we utilize our micro-fabricated thermocouple probe to monitor intracellular temperatures during stimulated mitochondrial proton uncoupling in *Aplysia* neurons. We use a highly specific proton uncoupler, BAM15, to induce proton currents across the mitochondrial membrane. By analyzing the time scales of the measured temperatures, we identify a component that lasts over ~1 s and correspond well to proton currents during stimulated mitochondrial proton uncoupling.

In Chapter 4, we theoretically explore the expected temperature changes during endogenous and stimulated biochemical reactions in cells to identify which thermometry technique is suitable for a given biochemical pathway. We find that under endogenous conditions, the intracellular temperature changes are < 10 mK in intracellular organelles. We computationally show how the temperature changes amplify to ~ 1 K at tissue length-scales, where temperature measurements can be a useful physiological parameter to monitor endogenous biochemical reactions. We also critically examine the validity of commonly used effective thermal conductivity approximations at cellular length scales.

In Chapter 5, we develop a wireless temperature measurement technique that can be useful for centimeter-scale (tissue level) measurements. We use a magnetostriction based technique that can enable deep tissue measurements. We computationally model magnetostrictive materials to identify the material

properties that can enhance the sensitivity to temperatures. We also explore how the sensing scheme can be scaled down to sub-cm length scales.

In Chapter 6, we summarize the main research contribution of this dissertation. We present possible future extensions to our magnetostriction based temperature sensing techniques that resemble MRI type measurements to enable truly wireless temperature mapping of tissues. We also highlight other open questions in cancer research and neuroscience that can be addressed through temperature measurements.

CHAPTER 2

DESIGN AND FABRICATION OF THERMOCOUPLE PROBE FOR INTRACELLULAR THERMOMETRY

This chapter is adapted from *Rajagopal et al., Sensors and Actuators A: Physical (2018)*. doi.org/10.1016/j.sna.2018.02.004.

Measuring temperatures within a biological cell requires a sensor with small thermal mass and microscale or smaller size that is electrically and chemically inert to the cell's environment, and is thermally isolated from the surroundings. We investigate how such requirements can be satisfied in a microscale thermocouple probe that is fabricated using the techniques of silicon-based microelectromechanical systems. Previous reports of invasive probes lacked either the required spatial resolution (<5 μm) or response time (<4 ms). Here, we report 1 μm thick silicon nitride supported probes with a 5 μm tip that has a response time of 32 μs. These figures enable future transient thermometry of cell organelles. To reduce calibration errors, we devise an on-chip calibration in a vacuum cryostat. We find that the accuracy of our measurements is ~1% for 300 ± 10 K. This work paves the way toward future thermometry at a subcellular level.

2.1 Introduction

Temperature is a fundamental thermodynamic property affecting every biochemical reaction in cellular environments. Living cells undergo temperature mediated activities such as cell division [64], gene expression [65], protein stabilization [66] and metabolism [67], [68] Extracellular thermometry has been shown to be important in detecting cancer [69] and thyroid-related diseases [70], and for understanding multiple metabolic pathways [71]. In comparison, thermometry at the subcellular level is relatively less explored. The dominant heat generation reactions inside a cell include the mitochondrial respiratory chain (non-shivering), and the reactions that consume ATP (shivering), both of which are the

primary modes of thermal regulations in warm-blooded animals [10]. Temperature gradients can be established within a cell by the reactions associated with multiple organelles in a cell. The nucleus, mitochondria, and centrosomes have been found to be at a temperature of 0.5–1 ˚C higher than cytoplasm [21]. In addition to gradients, temperature transients also arise, for example, when a cell is subjected to external stimuli such as light [72], drugs [73], or during sudden neurophysiological activities in neuron cells [5]. To understand the physiology of such reactions, there is a growing interest in the measurements of intracellular temperatures, especially in adipose tissues, muscles, and neurons. Since the cell wall and cytoplasm smoothen out the temperature fluctuations arising within the cell, an intracellular probe is necessary for such measurements.

Intracellular thermometry can be invasive or non-invasive. Typically, non-invasive techniques rely on fluorescence lifetimes or intensities that are temperature-dependent. Okabe et al. [21] used the fluorescence lifetime of a polymer to map temperatures in a cell with an estimated calibration resolution of 0.18–0.58 K. However, the accuracy of measurement was greatly reduced by the presence of a significant temperature gap between the optical setup in the microscope and the sample. The resulting errors were estimated to be as high as 0.35–1.3 K [21]. In a different study, a bio-compatible green fluorescent protein (GFP) has been used as an intracellular temperature probe by using its fluorescence polarization anisotropy (FPA) [74]. The FPA of GFP was calibrated for thermometry using a temperature-controlled bath with an accuracy of 0.4 K. However, the readings within a cell show an error of 1.2 K over few seconds of laser heating [74]. Recently, the fluorescence intensity of quantum dots has been used to measure intracellular temperature variations in a neuron [4]. It was observed that each quantum dot particle of the same type exhibited different sensitivities of the fluorescence intensity to temperature. Since it was not possible to follow a single quantum dot for both calibration and measurements, a mean sensitivity obtained from calibration of multiple quantum dots was used in the measurements. This serves to reduce the accuracy of the measurements. The reported measurement uncertainty is around 1 K. Non-invasive thermometry techniques typically have accuracies ~1 K. They also suffer from non-specific signals recorded as temperature. Such signals arise from photobleaching [4], variations in ion concentrations, pH, light intensity [63], and microscale viscosity changes within the cell milieu [24], [63].

Invasive thermometry utilizes a chemically inert sensor that is typically formed using a micropipette. One of the earliest attempts involved platinum wires

inside micropipettes that were coated on the outside with gold to form a thermocouple junction at the tip [75]. Watanabe et al. [76] made a similar attempt but with both metals coating the outside of a micropipette. These earlier studies did not report any sensible measurements in biological cells. Recent attempts involved thermocouple junctions in microcapillaries [77] or tungsten-based thermocouple probes [58], [59]. However, both approaches suffer from critical deficiencies. Metal-filled microcapillaries have been reported to have a thermal time constant around 600 ms [77], which is two orders of magnitude larger than the typical time constants of action potentials in neuron cells [78]. Tungsten-based probes have a junction that is 7–10 μm [59] in length at the tip. This is problematic for cells with a typical size of 10 μm. Another issue is that past work utilized a water bath for calibration [58], [77], [79] where local convection effects, temperature differences between the reference sensor and the probe, as well as errors from the reference sensor introduce calibration errors. While these errors are insignificant in typical applications, they gain significance when measuring small (500 mK) temperature changes in intracellular thermometry. In summary, current sensing techniques measure temperature changes in excess of ∼1 K with no emphasis on smaller gradients or transient responses.

An invasive intracellular thermometer should be smaller than ∼5 μm to avoid fatal cell damage [80]. A further restriction on size arises from the fact that transient responses of interest occur on time scales 4 ms [78]. The latter places a constraint on the thermal mass of the sensor. In this chapter, we design and fabricate a thermocouple junction, 1 μm in diameter, on a suspended silicon nitride cantilever of 5 μm tip diameter for measuring intracellular temperature changes in vitro. The design yields a thermal time constant as small as 32μs. The junction diameter of 1 μm offers spatial resolution sufficient for intracellular measurements. We avoid using a water bath for calibration, and instead devise an on-chip calibration using a gold resistor on the chip. We show that the calibration error can be reduced to be comparable to the noise floor. The fabrication process allows for batch fabrication, making it possible to produce multiple (16 in this work) probes from a 4inch silicon wafer. This chapter is organized as follows. Section 2.2 presents the fabrication steps. Section 2.3 discusses the technique used for on-chip calibration. Section 2.4 discusses testing of the probe and provides estimates of the time constant of the probe.

2.2 Fabrication

Starting from a double-side polished (100) wafer that is p-doped to a resistivity of 10–20 Ω.cm, we deposited a stress-free, 1 μm thick silicon nitride using plasma-enhanced chemical vapor deposition (PECVD) on STS Mesc Multiplex PECVD operated at a mix of 13.56 MHz and 380 kHz. The silicon nitride layer, as shown in Figure 2.1a, forms the material for the cantilever that eventually supports the metal lines forming a thermocouple. Among common cantilever materials such as silicon carbide, doped silicon, and flexible polymers [81], we chose silicon nitride for this work since it provides excellent thermal isolation of the thermocouple junction from the base of the cantilever, and is also an electrical insulator. Its compression strength of ~600 MPa [82] with an Young's modulus of ~152 GPa [83] enable the cantilever to easily overcome a cell wall's puncture stress of ~1 MPa [84].

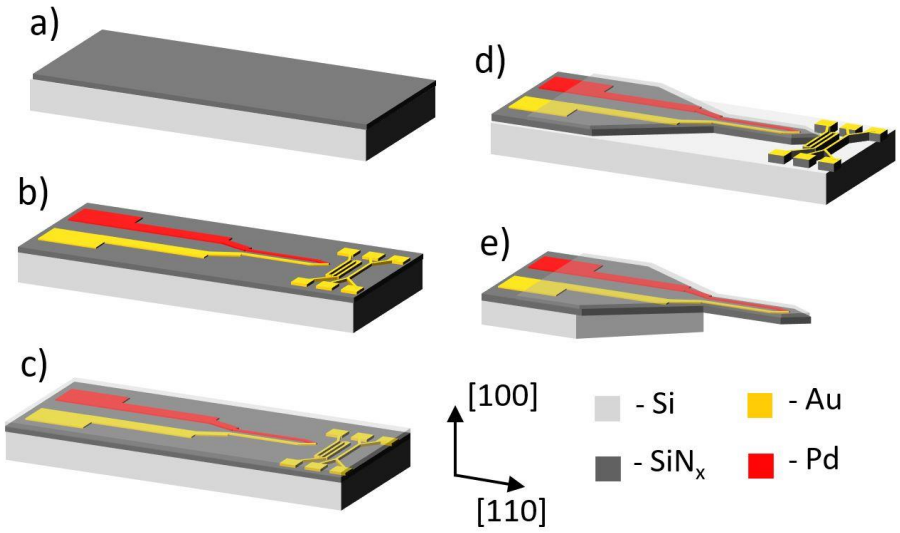

Figure 2.1: Fabrication of the probe starts with (a) deposition of SiN_x using PECVD, followed by (b) deposition of thermocouple metal lines, and resistors for calibration. The thermocouple is calibrated as discussed in Section 2.3. This is followed by (c) deposition of a thin SiN_x layer to protect the thermocouple, (d) reactive ion etching of SiN_x to get the required profile using a patterned photoresist mask, and finally, (e) aq. KOH etching of silicon to suspend the probe.

Electron beam metal evaporation (Temescal FC-2000 deposition system) was used to deposit 70 nm thick, 400 nm wide gold and palladium films on top of the 1 μm thick silicon nitride layer. The films were defined using a combination of UV photolithography (Karl Suss MJB3) and electron beam lithography (Raith eLine) to the dimensions of the thermocouple. We chose gold and palladium for the thermocouple since they are resistant to KOH etching that is subsequently used to release the cantilever. Following the deposition of the metal films for the thermocouple, 300 nm thick metal films were deposited to form heaters and thermometers for calibrating the thermocouple junction, as shown in Figure 2.1b. The reference thermometer and thermocouple junction were both 12 μm away from heater. We calibrated the thermocouple prior to releasing the probe from the wafer. After calibration, we deposited a 200 nm thick PECVD silicon nitride layer on top of Si/SiN_x /metal-junction to protect the calibrated thermocouple junction. The second nitride layer, shown as a translucent layer in Figure 2.1c, protects the chrome adhesion layer used for metal lines from aqueous KOH etching. A photoresist was patterned to the desired shape of the probe. Using the photoresist as a mask, the nitride was etched using reactive ion etching (PlasmaLab systems Freon RIE) until silicon was exposed. Multiple RIE steps were performed until a profile such as the one shown in Figure 2.1d was obtained. The protective nitride layer only at the contact pads was etched away carefully to expose contact pads for electrical connections. The metal electrodes that were used for calibration were unaffected by RIE. However, they were removed in the subsequent step. The design of the metal electrodes, and the pattern of the probe profile ensure that the tip is oriented along [110]. The nitride tip that extends along [110] has a convex edge and is on top of the silicon substrate. These features collectively enhance the etch rate of silicon under the tip when aq. KOH is used. Bulk silicon etching was performed using 45% aq. KOH at 80°C bath temperature. The samples were held by clamps for about 40–50 min while etching. By the end of the etch process, a tip of length ~451 μm was suspended, as shown in Figure 2.1e. Figure 2.2 shows an SEM image of the fabricated probe. Silicon nitride being a poor thermal conductor, isolates the tip from temperature fluctuations in the silicon substrate, and therefore from the external surroundings. During intracellular thermometry, we expect only the suspended part to enter the cell, which enhances thermal isolation. Electrical continuity of the probe after suspension was verified by measuring the thermocouple's resistance before and after etching. Further tests to verify the probe's measurements are discussed in Section 2.4.

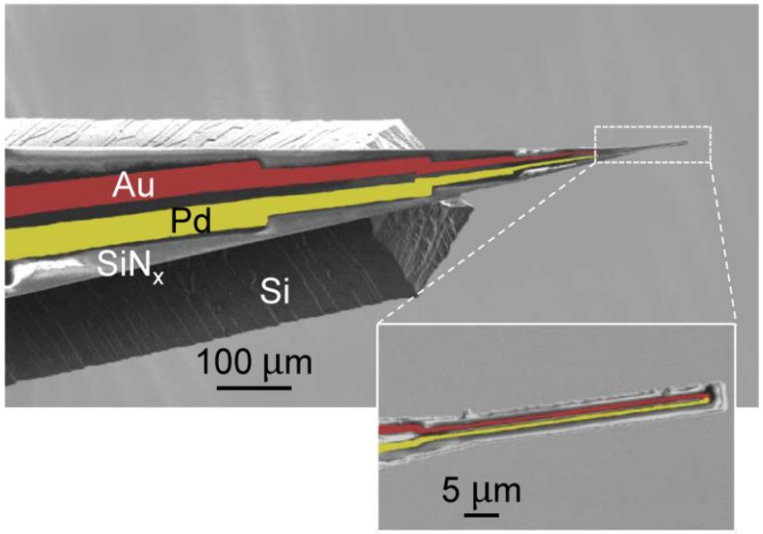

Figure 2.2: Scanning electron microscopy images (false-colored) of the fabricated thermocouple on a cantilever. The tip diameter is ~5 µm. The suspended region is ~451 µm long. The silicon substrate seen underneath the nitride has (111) planes exposed everywhere.

2.3 Calibration

In previous work, thermocouples for cellular thermometry were calibrated in a water bath. However, as discussed in Section 2.1, this can lead to significant error due to convection effects in calibration for a probe meant to measure 500 mK changes. Here, we avoid this issue through an in-situ calibration process that follows the deposition of metal lines as shown in Figure 2.1b, and prior to etching the bulk silicon. The calibration is done in a vacuum cryostat using a heater and a reference thermometer on-chip, as shown in Figure 2.3. The heater line is 12 µm away from both the thermocouple junction and the reference junction. The close proximity of the sensors and vacuum conditions ensure heat conduction to be the dominant heat transfer mechanism. Therefore, an on-chip calibration method minimizes local convection currents and provides an accurate calibration of both the reference thermometer and the thermocouple junction.

The calibration is a two-step process where a reference electrical resistance thermometer is itself first calibrated in a vacuum cryostat. The thermocouple is then calibrated in the second step using the calibrated resistance sensor. In the first step,

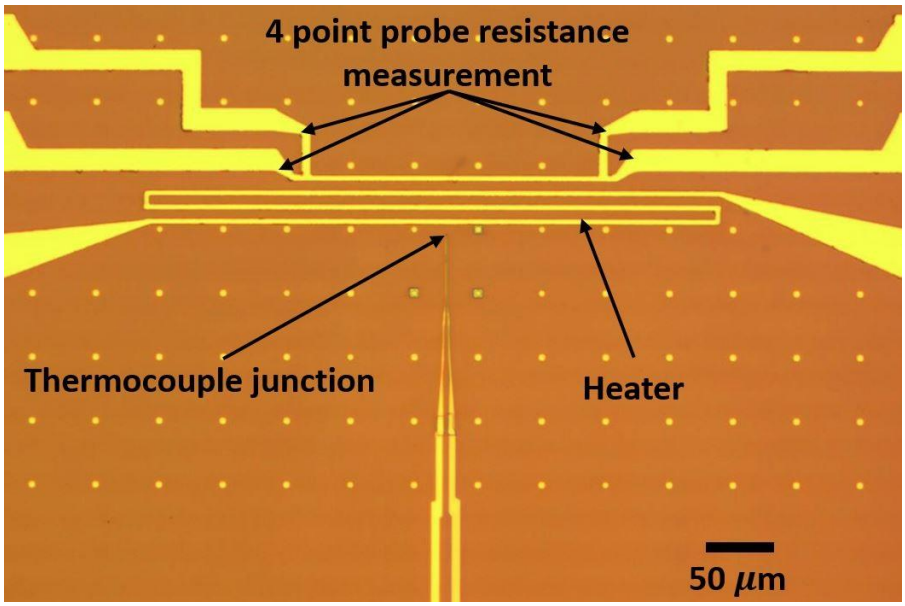

Figure 2.3: Calibration of the thermocouple junction is done using two thin film gold resistors that act as heater and temperature sensor. The measurements are done in a temperature-controlled cryostat under high vacuum conditions ($<10^{-6}$ bar).

the temperature coefficient of resistance (TCR) of the resistor line is calibrated by measuring changes in electrical resistance at different bath temperatures of the cryostat. The bath temperature of the cryostat has an accuracy of 1 mK. The electrical resistance of the resistor is measured using a 4-point probe method with two SR830 lock-in amplifiers. In the second step, a Keithley DC current source provided current to a serpentine heater line equidistant from the resistor and the thermocouple tip, as shown in Figure 2.3. As a first approximation, the temperature rise at the thermocouple tip and the resistor respectively can be assumed to be the same. We later examine the validity of this assumption. A Keithley nanovoltmeter measured the potential difference across the thermocouple junction. The change in resistance at the resistor increases quadratically with the current at the heater, confirming that the resistance change is indeed due to increased temperatures. Figure 2.4 shows the resistance change with DC heating current.

The Seebeck coefficient of the thermocouple junction is obtained by fitting a straight line between the potential difference measured at the junction and the temperature rise measured at the resistor, as shown in Figure 2.5. We obtained a Seebeck coefficient of 1.18 V/K for the Au/Pd junction. This is comparable to previously reported estimates for few-nm thick metal lines [85]. Any differences in

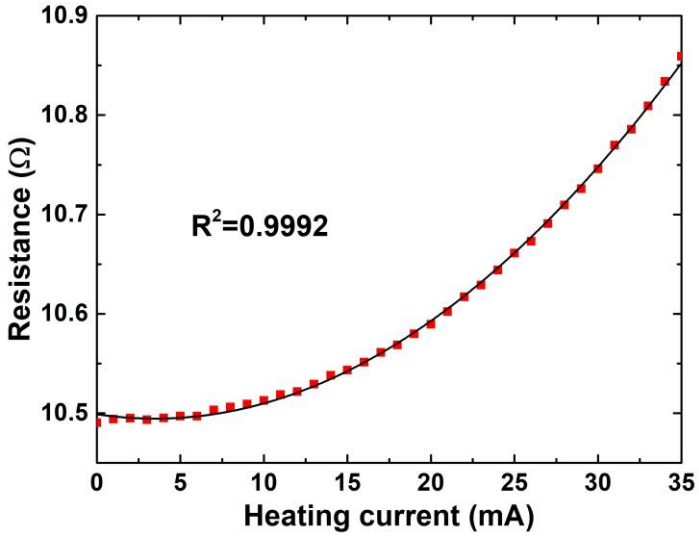

Figure 2.4: The resistance of the thin film resistor is plotted against the heating current. The data points shown in red squares fit well to a quadratic curve with a coefficient of determination (R^2) of 0.9992.

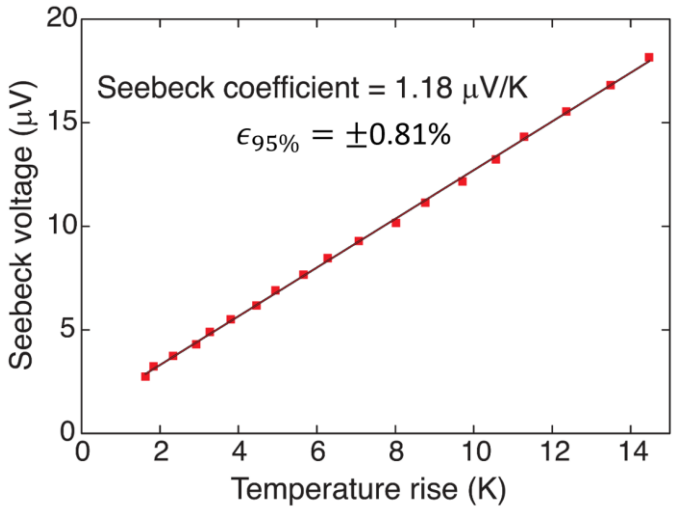

Figure 2.5: The Seebeck voltage across the Au/Pd junction is recorded as its temperature is increased by a heater. Temperature at the thermocouple junction is assumed to be the same as the thin film resistor. The data points are shown in red squares. Seebeck coefficient of the junction is the slope of a straight line fit to these points.

the observed Seebeck coefficient and previously reported values could be attributed to the thickness and quality of the metal films. The estimated error in the slope is ±0.81%, corresponding to the 95% confidence interval. This calibration process was performed on each probe. We found the Seebeck coefficient to vary within the range 0.8–1.3 μV/K over a wafer.

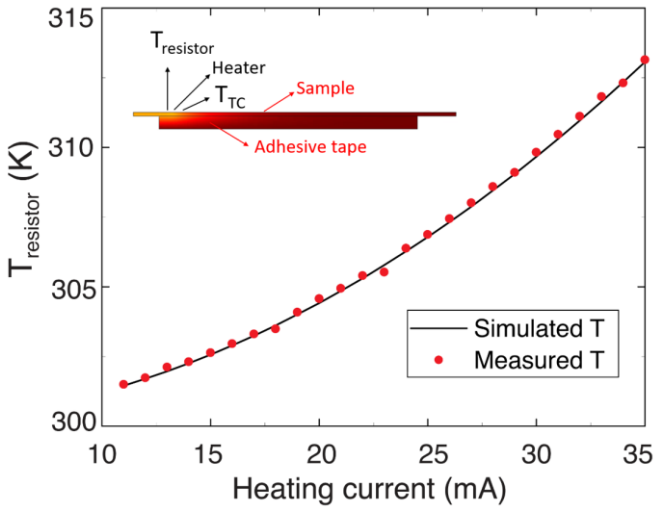

Figure 2.6: The simulated temperature rise at the resistor ($T_{resistor}$) is compared against measurements for increasing current at the heater. $T_{resistor}$ is obtained from 4pp resistance and the TCR of the thin film resistor. $T_{cryostat}$ = 300 K. (Inset) The geometry used for the simulation.

A subtle issue in the calibration arises from the fact that the temperatures at the thermocouple junction and thin-film resistor may not be identical due to asymmetry. To investigate this issue, we performed finite element simulations of the calibration process in COMSOL to understand whether the asymmetry introduces a significant calibration error. The inset of Figure 2.6 shows the geometry of the model. The serpentine heater line shown in Figure 2.3 produces a temperature distribution that is symmetric along a (110) plane parallel to the length of the probe that bisects the heater and resistance sensor lines. For numerical simulations, we utilize this symmetry to model a 2D cross-section of the sample along the symmetry plane. While calibrating the sample in a vacuum cryostat, the sample was fixed to an adhesive tape on a chip holder. The exposed sides of the adhesive tape and the sample are the outer boundaries of this geometry. The cryostat's bath temperature ($T_{cryostat}$) yields the boundary condition at the bottom of the system. Adiabatic boundary conditions apply elsewhere since the system is in

vacuum. The heater line is modeled as a constant heat source whose magnitude is equal to that of the heating power used in the measurements. The thermal properties of the materials are taken from the literature: $k_{Au\ film}$ = 225 W/(m.K) [86], k_{SiNx} = 0.8 W/(m.K) [87], k_{Si} = 126.8 W/(m.K) [87], and k_{tape} = 1.4 W/(m.K) [88]. The thermal contact resistance between the thin films (SiN_x /Si, Au/Cr/SiN_x) is on the order of 10^{-8} m^2 K/W [89], [90], and is insignificant compared to the resistance of the adhesive tape (~10^{-3} m^2 K/W) itself. The contact resistance on either side of the adhesive tape is also assumed to be negligible [91].

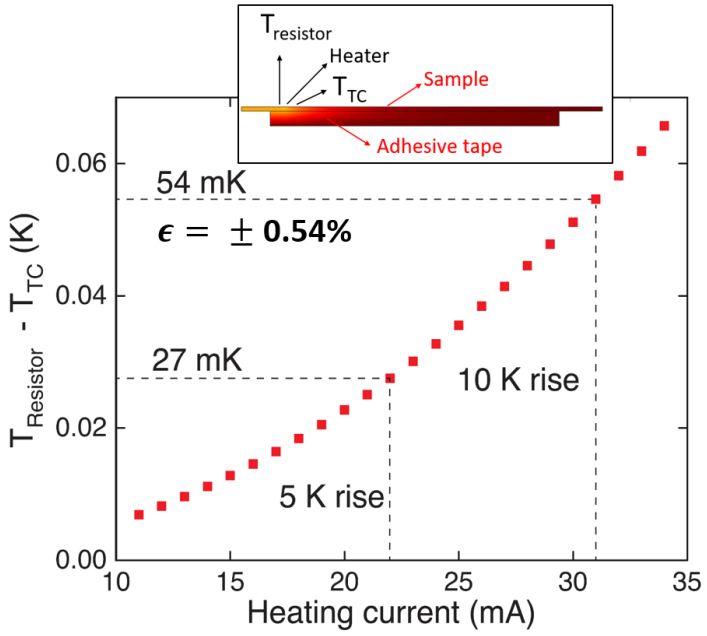

Figure 2.7: The temperature difference between the thermocouple tip and the thin film resistor is calculated at different heating currents. 31 mA heating current is estimated to produce 10 K rise at the resistance sensor. The error due to assuming symmetricity is 54 mK when the measured temperature rise from ambient ($T_{cryostat}$ = 300 K) is 10 K.

We first compare the temperature rise at the thin film resistor estimated from simulations against our measurements in Figure 2.6 as a validation step. The simulated rise closely follows the measured values with a maximum deviation of 0.63% at the highest heating current. This confirms that the thermal properties and boundary conditions used in the simulation adequately represent the calibration setup. Using this validated model, we now estimate the temperature differences between the thermocouple tip (T_{TC}) and thin-film resistor ($T_{resistor}$) during calibration.

Figure 2.7 shows the difference in temperature between the resistor and the thermocouple junction at different heating currents. The bath temperature of the cryostat is fixed at $T_{cryostat}$ = 300 K in these calculations. For a 10 K rise in temperature at the junction, we find the error in calibration to be 54 mK. The error decreased to 27 mK for a 5 K rise from $T_{cryostat}$. The simulations help to determine the maximum heating current to be used in calibration for the desired accuracy. For operating at 300 K, the accuracy of calibration is ± 0.54%. Combining this with the 95% CI for the slope in Figure 2.5, the total error in calibration is ~± 0.97%. When operating at 300 ± 10 K, the error is ±54 mK. We note that this figure is ~2 orders of magnitude larger than the apparent temperature resolution of 0.85 mK possible with the probe when using a nanovoltmeter with 1 nV resolution. Further, we show experimentally in Section 2.4 that the noise floor is comparable to this calibration error. Hence, the calibration approach described here helps to reduce the overall measurement uncertainty to approach the noise floor.

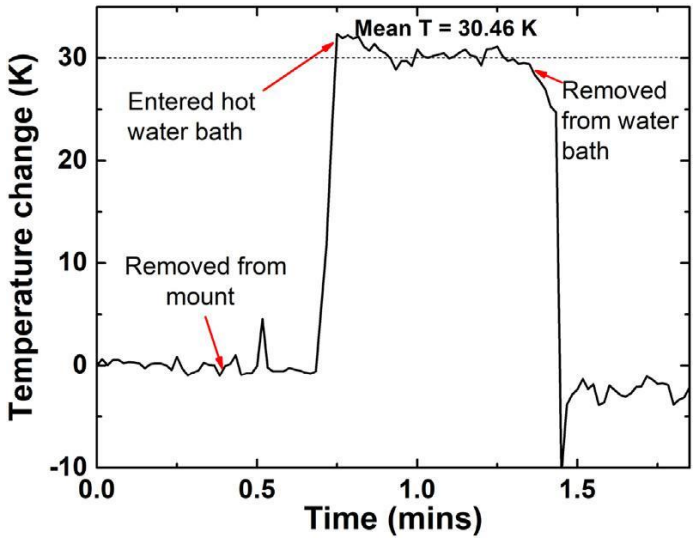

Figure 2.8: Transient temperature change measured in a hot water bath at a frequency of 1 Hz.

2.4 Thermal response

To observe the probe's temperature response after fabrication, we subjected it to a sudden temperature difference by dipping it in a water bath that was kept at 30 K above room temperature. The water bath's temperature was measured independently using a commercial Type-K thermocouple from Omega. Figure 2.8 shows transient temperatures at the probe, measured using a nanovoltmeter

connected to the probe. From time t < 0 to t = 0.4 min, the probe remained stationary, fixed to a mount. The probe was removed from the mount at t = 0.4 min and slowly moved towards the water bath. Sudden spikes in temperature readings were observed when the probe was manually moved. This is likely due to vibrations at the external solder joints while the probe was moved. As the probe touched the hot water surface at t = 0.7 min, the measured temperature rose almost instantaneously on the time scale of Figure 2.8. The probe measured an average temperature of 30.46 K during the 40 s it was inside the hot water bath. At t = 1.4 min, the probe was removed from the water bath, which briefly induced evaporative cooling that resulted in a sudden decrease in temperature. We measured the noise floor in a quiescent water bath at room temperature to be around 42 mK over a few minutes. The noise floor increased in air to ~211 mK. The temperature oscillations are possibly due to natural convection around the probe.

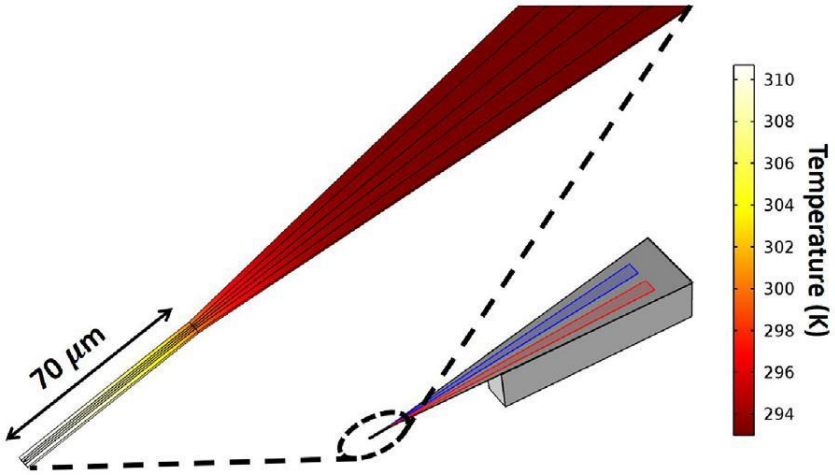

Figure 2.9: The simulated temperature contour of the probe at t = 5 µs. An initial temperature of 313 K is applied to the tip, while the ambient is at 293 K. (Inset) The geometry used for the simulation.

The data acquisition rate in the experiment shown in Figure 2.8 is not sufficient to characterize the thermal response time of the probe. Typical thermal time constants of action potential pulses in neuron cells range from 4 to 100 ms [78]. To reliably measure stimuli at such time scales, we designed the thermal time constant of the sensor to be at least an order of magnitude lower. Here, we report numerical simulations in COMSOL to obtain the value. The geometry of the simulation is shown in the inset of Figure 2.9. In this case, the symmetry plane

defined in Section 2.3 is no longer a plane of symmetry since the width of the suspended probe gradually increases along the plane. Therefore, we extend the validated simulation model discussed in Section 2.3 to model a 3D geometry that resembles our probe. The 70 μm long probe tip was initially given a temperature of 313 K at t = 0 s. It is assumed to cool in water at 293 K for t > 0, and the time it takes to reach ambient conditions (293 K) is calculated. A natural convection boundary condition is applied to all the exposed surfaces except for the 70μm tip region. We use a convection coefficient of 50 W/m^2 K corresponding to natural convection in water. The convection coefficient along the microscale tip structure is typically much larger than at large scales. So, for the outer surfaces of the tip, we use a heat conduction boundary condition, pointed out by Hu et al. [92] to be appropriate for microfabricated structures. The specific heat capacity of the materials used in the model are taken from the literature: $C_{Metal\ film}$ = 0.13 J/g K [93], C_{SiNx} = 370 J/kg K [94], and C_{Si} = 672 J/kg K [95]. Other required material properties are the same as discussed in Section 2.3.

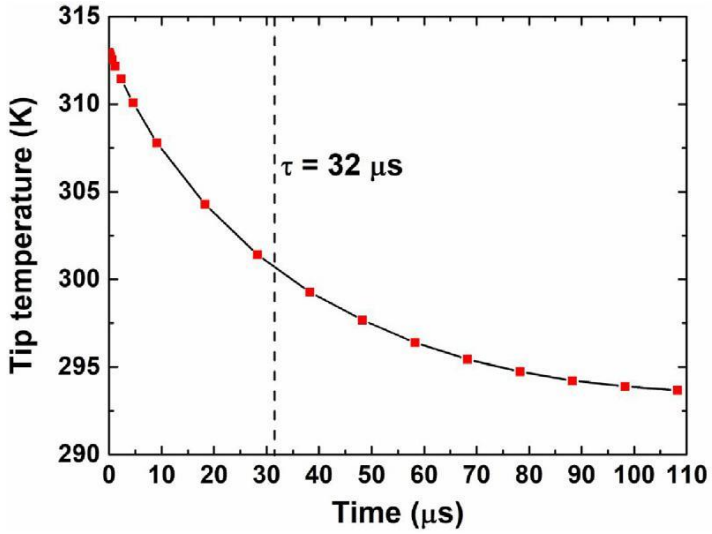

Figure 2.10: The simulated tip temperatures plotted against time as the probe cools down in water. The simulated points are shown in red squares. An exponential line fit to these points is used to obtain the thermal time constant of the probe.

We solved a transient three-dimensional heat conduction equation using the finite element method. A snapshot of the temperature profile at t = 5 μs is shown in Figure 2.9. We calculate the temperature at the thermocouple tip over time as shown in Figure 2.10. The thermal time constant of the probe is the time taken to change

the temperature by a factor of 1/e. From Figure 2.10, the value is 32 μs, which is comparable to and better than the typical time constants of microscale thermal probes [77], [79]. The material and the small length scales of our thermocouple probe thus make it possible to have a thermal response time that is a few orders of magnitude smaller than the stimuli in a typical neuron cell [78].

2.5 Conclusion

In summary, we fabricated a thermocouple junction of 1 μm diameter in a silicon nitride cantilever of tip diameter 5 μm to serve as an intracellular thermometer. The low thermal conductivity, high stiffness and chemical inertness of silicon nitride make it a good choice for such a probe. We calibrated the thermocouple using an on-chip resistance sensor in a vacuum cryostat to obtain a calibration accuracy of ±0.97%. A detailed error analysis of the calibration process shows that the accuracy can be further improved by limiting the heating current used for calibration. We demonstrated the use of the probe in an aqueous environment and found the noise floor to be 42 mK, which is comparable to the calibration error for 300 ± 10 K. The sensor has a low thermal mass with a calculated thermal time constant of 32 μs, much smaller than the time constant of a neuron. This work advances the design and fabrication of thermometers for intracellular measurements. Additional details on the recipe for fabrication is described in detail in Appendix A and elsewhere [46], [96].

CHAPTER 3

TRANSIENT HEAT RELEASE DURING INDUCED MITOCHONDRIAL PROTON UNCOUPLING

This chapter is adapted from *Rajagopal et al., Communications Biology (2019).* nature.com/articles/s42003-019-0535-y.

Non-shivering thermogenesis through mitochondrial proton uncoupling is one of the dominant thermoregulatory mechanisms crucial for normal cellular functions. The metabolic pathway for intracellular temperature rise has widely been considered as steady-state substrate oxidation. Here we show that a transient proton motive force (pmf) dissipation is more dominant than steady-state substrate oxidation in stimulated thermogenesis. Using transient intracellular thermometry during stimulated proton uncoupling in neurons of *Aplysia californica*, we observe temperature spikes of ~7.5 K that decay over two timescales: a rapid decay of ~4.8 K over ~1 s followed by a slower decay over ~17 s. The rapid decay correlates well in time with transient electrical heating from proton transport across the mitochondrial inner membrane. Beyond ~33 s, we do not observe any heating from intracellular sources, including substrate oxidation and pmf dissipation. Our measurements demonstrate the utility of transient intracellular thermometry in better understanding the thermochemistry of stimulated mitochondrial metabolism.

3.1 Introduction

Biochemical reactions are sensitive to variations in temperature, pH, O_2, glucose, etc., of which temperature has been the focus of several studies by clinical neuroscientists [1]. Temperature fluctuations in the brain on the order of 1-2 °C can impact memory encoding, effect behavioral changes, and generate autonomic

responses [1]. The apparent sensitivity to overall brain temperature originates from reactions at the level of individual neurons. To counteract large external temperature fluctuations, animal cells have evolved certain thermoregulatory mechanisms. For instance, heat shock has been shown to trigger compensatory intracellular endothermic reactions [13] that can alter gene expressions and activate signaling cascades [14]. On the other hand, in adapting to cold environments, for instance, exothermic non-shivering thermogenesis is induced at mitochondria [11], [97], [98] to produce heat. Despite recognition of the fundamental involvement of temperature in eliciting biochemical changes, specific molecular mechanisms for

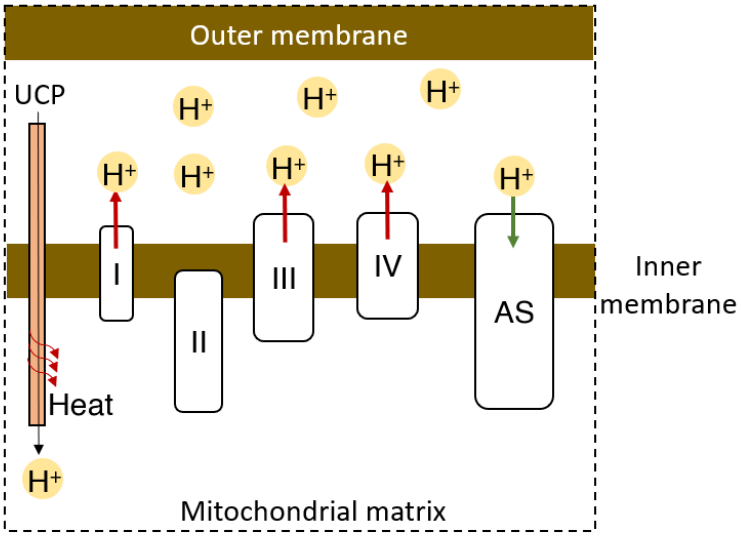

Figure 3.1 Proton uncoupler in action at the mitochondrial inner membrane. A schematic of the mitochondrial respiratory chain shows three protein complexes (I, III, IV) producing an H^+ gradient across the inner mitochondrial membrane. ATP synthase (AS) utilizes this H^+ gradient to synthesize ATP from ADP. Proton uncouplers such as uncoupling proteins (UCP), BAM15, or CCCP allow diffusion of protons through the mitochondrial membrane. This sudden diffusion into the mitochondrial matrix results in a proton current that can generate heat.

heat evolution in cells are still not clearly identified experimentally [24], [56], [57], [99]. It is widely known that biological uncoupling proteins (UCP) uncouple oxidative phosphorylation, thereby converting the energy required to synthesize ATP into heat [12], [17]. This steady-state substrate oxidation is expected to produce only ~10^{-5} K temperature increase per cell [24], [56], [57], [99]. However,

at the onset of proton uncoupling (Figure 3.1), a transient proton motive force (pmf) dissipation occurs before enhancing substrate oxidation. In this work, we experimentally demonstrate for the first time that chemically induced pmf dissipation can result in large intracellular temperature spikes of ~4.8 K over a short duration of ~1 s in *Aplysia* neurons.

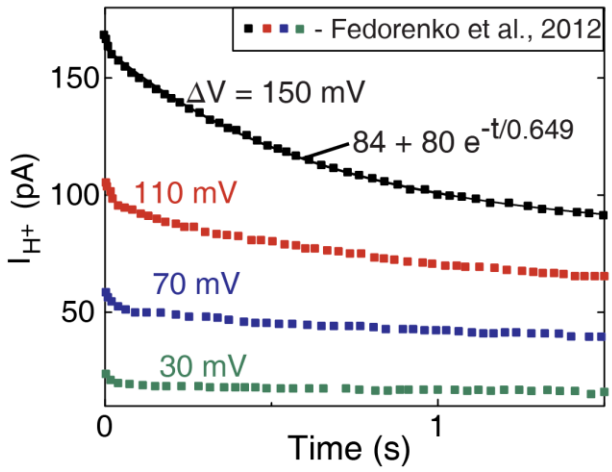

Figure 3.2 Measured proton currents from mitochondrial voltage patch clamp are plotted from experiments performed by Fedorenko et al [25]. At t = 0 s, the set voltage V is changed from 0 to 30 mV, 70 mV, 110 mV, and 150 mV. The voltage step generates a proton current that slowly saturates over time. We fit the current for the most relevant data set (ΔV = 150 mV, because mitochondrial proton motive force is typically ~150-200 mV) to an exponential decay function with offset, since current need not be zero at $t \rightarrow \infty$. We find that the proton current has a time constant ~0.65 s.

Proton uncoupling has been hypothesized to result in transient electrical heating [9] (Figure 3.1). The electrochemical proton motive force (Δp) generated by proton pumps (Figure 3.1) are typically 150-200 mV [9], [18], [55]. By sharply dissipating the whole mitochondrial potential (~150 mV) using a patch-clamp, previous studies [25], [100] experimentally reported an exponentially decreasing proton current (I_{H^+}) with a maximum current ~150 pA (Figure 3.2)[25]. We can theoretically estimate the maximum proton flux (j_{H^+}) using the buffering power (β) of mitochondrial matrix. Using measured values for β_{mito} (~110 mM/pH-unit, [101]) and ΔpH_{mito} (~ 0.5, [54]), the proton influx is on the order of ~10^8 s^{-1} ($j_{H^+} = \beta_{mito} \cdot \Delta pH_{mito}$, for a 2 µm mitochondria, [102]). This corresponds to I_{H^+} ~100

pA that matches well with previous experimental measurements [25], [100]. Further, the mitochondrial membrane potential dissipation is almost instantaneous (on the order of a few seconds) when exposed to proton uncouplers [55]. The resulting heat ($\dot{Q} \sim \Delta p \cdot I_{H^+}$) can cause a temperature rise in a single mitochondrion at a rate of ~4.8 K/s at the onset of proton motive force dissipation [9]. This heat pulse is expected to be < 1 s owing to the short duration of proton currents (Figure 3.2) [25]. We note that the previously reported magnitudes of I_{H^+} and Δp, and the duration of proton current may vary across different cell lines depending on the expression of UCP [100] and the proton pool. However, irrespective of UCP expression, chemical proton uncouplers can similarly increase the permeability [53] of protons across the inner membrane of mitochondria, resulting in a short-lived proton motive force dissipation and associated heating. Previous thermometry on proton uncoupling probed longer temporal scales of ~5 min or more [4], [21]–[23], [103], [104] but missed information on short-term pmf dissipation effects. To record transients during pmf dissipation, a thermometry technique that combines low thermal time constant (< 1 s) with high accuracy (< ± 1 K), as well as chemical and electrical inertness, is necessary.

Previous reports of non-invasive thermometry [4], [21], [74] using temperature-dependent fluorescence lifetimes or intensities typically had accuracies $\gtrsim$ 1 K [46]. They also suffered from off-target signals [4], [24], [63] that came from photobleaching [4], variations in microscale viscosity, ion concentrations, and intracellular pH changes within the cellular environment [24]. Chemically inert micro-fabricated thermocouples [105] were previously made that measured extracellular, but not intracellular temperatures. Invasive intracellular thermometers have been made from micropipettes [75]–[77], [79] and tungsten-based probes [58], [59]. Metal-filled micropipettes [77] have a thermal time constant ~0.6 s, which is high for measuring transient pmf dissipation over < 1 s. Tungsten probes that have a long 7-10 μm junction [59] measure spatially averaged temperatures inside a cell. Invasive thermometers that are also electrically bare [58], [59], [75]–[77], [79] suffer from common mode noise [43], when used in an electrically active cellular milieu. Moreover, previous reports [58], [59], [75]–[77], [79] typically used a water bath for calibrating the temperature response of the sensors. This can result in errors arising from local convection effects, and temperature differences between the reference sensor and the probe. Overall, existing sensing techniques lack the required chemical and electrical inertness, accuracy (< ±1 K), and low thermal time constant (< 1 s) to measure transient pmf dissipation.

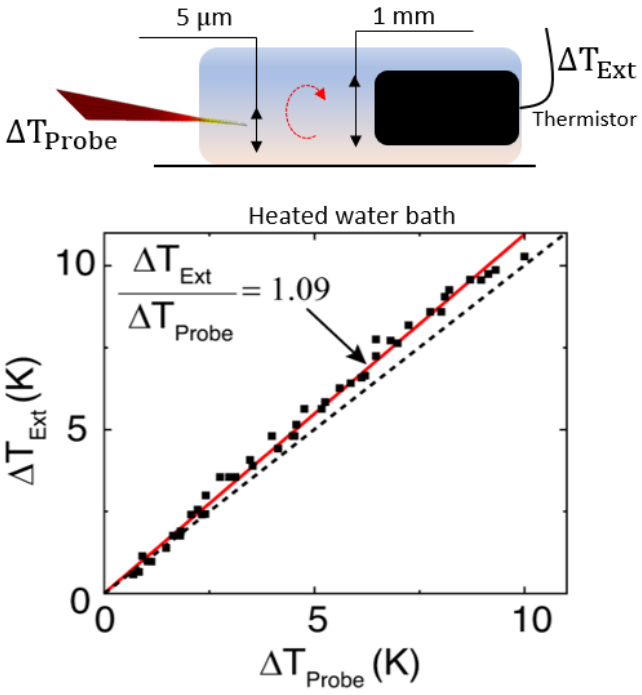

Figure 3.3: Using a heated microscopy stage, we measured the temperature changes using the microthermal probe (ΔT_{Probe}) placed inside a neuron of buccal ganglion and also an external thermistor (ΔT_{Ext}) placed in the saline bath ~1 cm away from the ganglion. An omega thermistor (TH-44032-40-T) was used in conjunction with a recording device (Measurement Computing USB-TEMP) to measure ΔT_{Ext}. We heated the culture dish by 10 K over a period of 1 hour in steps of 2-3 K. The Seebeck voltage from the microthermal probe yielded ΔT_{Probe}, using prior calibration. The bath's temperature rise (ΔT_{Ext}) was obtained from the external thermistor. We repeated the measurements three times with different step sizes; all data points are shown on the graph. The red line is a linear fit to the measured data, whereas the black dashed line corresponds to a slope of 1. The temperature measurement from the external thermistor is different from the microthermal probe's reading by ~9.5%. The difference, in magnitude, is as large as ~300 mK at the largest temperature rise of ~10 K. We attribute this difference to arise from convection currents inside the bath.

Here, we employed a microscale thermocouple probe to capture such transients in intracellular temperatures. Figure 2.2 shows the probe, fabricated using the techniques of silicon-based microelectromechanical systems (MEMS). Details of the fabrication are explained in Chapter 2 and in our previous work [46]. We performed an on-chip calibration in a vacuum cryostat (Figure 2.3), and

determined the calibration accuracy to be ~±0.97% at 300 K. We note that we do not use a heated culture medium, as was done in previous studies [58], [59], [75]–[77], [79], for calibrating the thermal probe. However, we tested our probe in a heated culture medium to confirm the temperature response (Figure 3.3). The temperature-sensitive Au/Pd thermocouple junction is 1 μm in diameter. It is supported by a 1 μm thick silicon nitride cantilever tip of 5 μm width. We calculated the time constant of the probe [46] to be 32 μs. The probe is electrically insulated with ~300 nm of silicon nitride. In Figure 3.4, we show that the probe is insulated

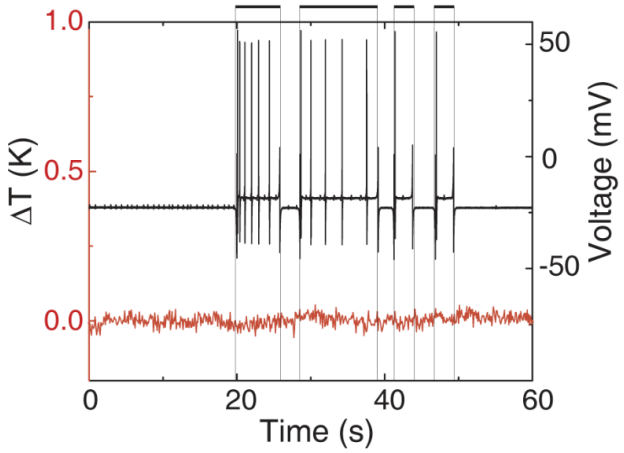

Figure 3.4: We tested the common mode noise response of the thermal probe by changing a neuron's potential with respect to ground. We placed both the thermal probe and the sharp microelectrode inside a neuron. The voltage plot shows the microelectrode reading that was high-pass infinite impulse response filtered to remove offsets from the electrode resistance. Starting at t = 20 s, we repeatedly depolarized the neuron by passing a constant current through the microelectrode; durations of the current are represented using dashed lines above the plot. This can result in a common mode signal on the two electrodes of the thermal probe that is also inside the cell. If the thermal probe was not insulated enough from the common mode signal in the neuron, a corresponding signal in the form of a voltage differential would be observed from the Nanovoltmeter [43]. For instance, a common mode signal of ~100 mV can result in 0.1 μV apparent Seebeck voltage that corresponds to ~0.1 K. Since, we observe < 20 mK temperature changes during depolarization and action potentials in the neuron, we can assume that the ~300 nm silicon nitride electrically insulates the probe from the typical electrical activity in neurons during our experiments.

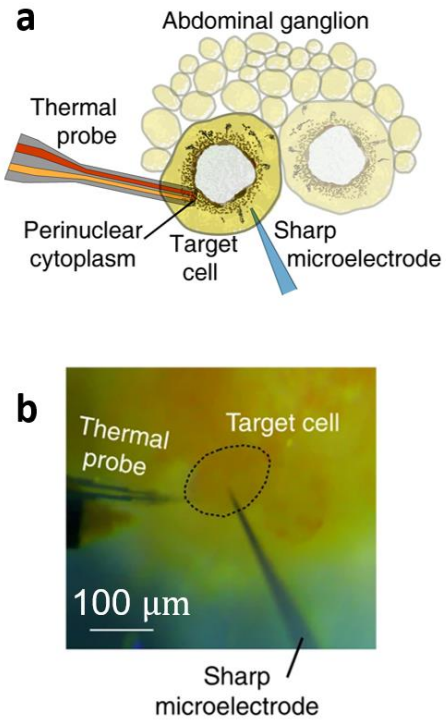

Figure 3.5**:** a) A schematic of the setup used for measuring temperature changes inside the cell while concurrently monitoring the membrane potential using a KCl sharp microelectrode. The brown patches in the perinuclear cytoplasm are representative of mitochondrial sites in *Aplysia* neurons. b) An optical image of the abdominal ganglion of *Aplysia*. The two probes are inside the target cell R15. Scale bar corresponds to 100 µm.

from common-mode signals, resulting in < 20 mK noise in a typical electrically active neuron.

We made intracellular measurements on neurons from the sea slug *Aplysia californica*. The animal's abdominal ganglion, which constitutes parts of a distributed central nervous system, possesses neurons that can reach up to ~1 mm in diameter [106], with nuclei [107] as large as ~800 µm. The perinuclear cytoplasm is enriched with mitochondria [108], [109]. The *Aplysia* neurons found superficially in the abdominal ganglion are typically hundreds of microns in diameter, which renders them favorable to penetration with our thermal probe that is ~5 µm wide. Unless mentioned otherwise, we used neurons from the abdominal ganglia throughout the study. We also utilized a sharp voltage microelectrode to record the

real-time membrane potential of the neuron as a metric of cell health (Figure 3.5). More details on the microelectrode and culture dish preparation are in the Methods section. Figure 3.5b shows an optical microscope image of the culture dish with the thermal probe and voltage microelectrode inside a neuron.

In this work, we measure transient intracellular temperature changes during proton motive force dissipation, which is induced by chemical proton uncouplers. We first identify off-target responses to the proton uncouplers. Then, we extract intracellular temperature responses from proton motive force dissipation.

3.2 Methods

Figure 3.6 shows the overall schematic of the measurement setup. We explain the components individually in the following sub-sections.

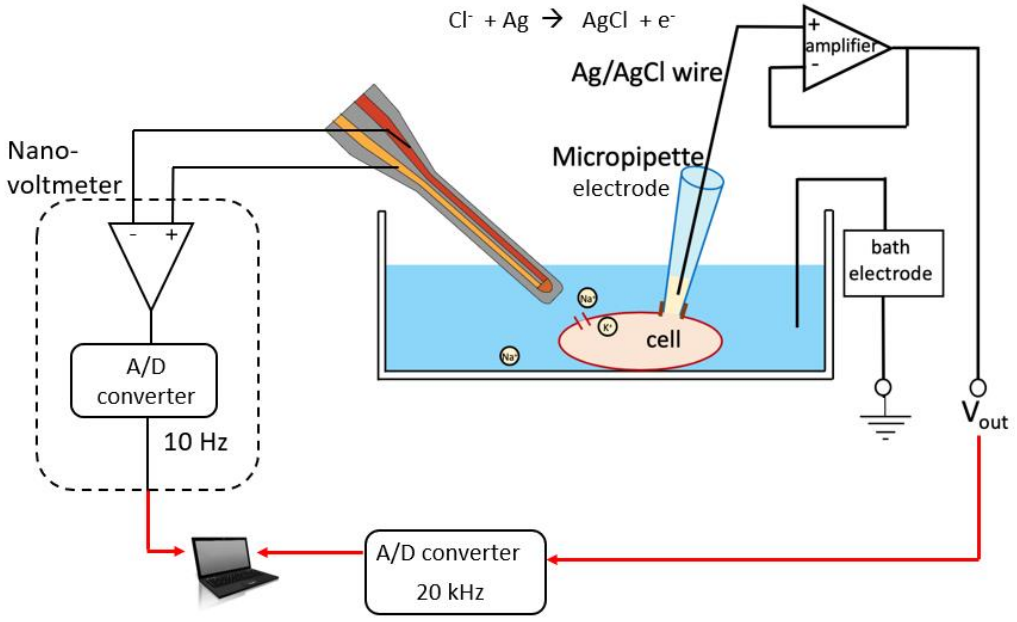

Figure 3.6 Overall schematic of the measurement setup used to measure the intracellular temperature changes in *Aplysia* neurons during mitochondrial proton uncoupling.

3.2.1 Culture dish preparation

We utilized neurons from the abdominal ganglion of *Aplysia californica*. Animals were obtained from the NIH/University of Miami National Resource for Aplysia Facility (Miami, FL) and housed at the University of Illinois in a 200-gallon closed marine system maintained at 12-13°C. Animals were anesthetized through injections of 330 mM $MgCl_2$ and the abdominal ganglion was dissected out. The abdominal ganglion was placed in a culture dish filled with room-temperature saline (composition, in mM: 420 NaCl, 10 KCl, 25 $MgCl_2$, 25 $MgSO_4$, 10 $CaCl_2$, 10 HEPES buffer, pH=7.5) and secured using insect pins. After microdissection and de-sheathing, the cells were accessible to the electrodes. The ventral aspect of the ganglion was carefully dissected to provide access to the neurons of interest. We prepared 1 mM solutions of BAM15 (Sigma-Aldrich) in 100 µL DMSO, which would form a final concentration of ~10 µM when added to the culture dish containing saline ~10 mL. We ensured consistency in temperatures of BAM15 and saline using external thermocouple probes (Omega Type-K).

3.2.2 Microelectrode preparation

Intracellular voltage recordings were made using borosilicate microelectrodes filled with 3 M KCl and pulled to a resistance of 11-16 MΩ. Intracellular microelectrodes were connected to an intracellular amplifier (Model 1600, A-M Systems, Sequim, WA), which were in turn connected to a data acquisition system (PowerLab 8/30, ADInstruments, Dunedin, New Zealand). Real-time voltage recordings were digitized and recorded in LabChart 7.3 (ADInstruments) at sampling rates of 20 kHz.

3.2.3 Intracellular temperature measurements

To measure intracellular temperature changes, we first penetrated the target neuron with a voltage electrode. We then penetrated the same neuron with the thermal probe. In this process, the neuron released an injury discharge response as shown in Figure 3.7b, and slowly returned to a healthy resting potential. In conjunction with a visual inspection of the probe tip's position, this served as an additional confirmation that the thermal probe successfully entered the target cell. During the injury discharge response, we also observed the temperatures to change (Figure 3.7a), possibly due to the saline bath warming up to room temperatures. We,

therefore, performed all experiments after the temperatures stabilized post-insertion of the probes (roughly ~30 min). A Keithley nanovoltmeter (2182A) was used to measure the Seebeck voltage, which is calibrated to be read as temperature changes. The sampling frequency was limited to 10 Hz by the external electronics.

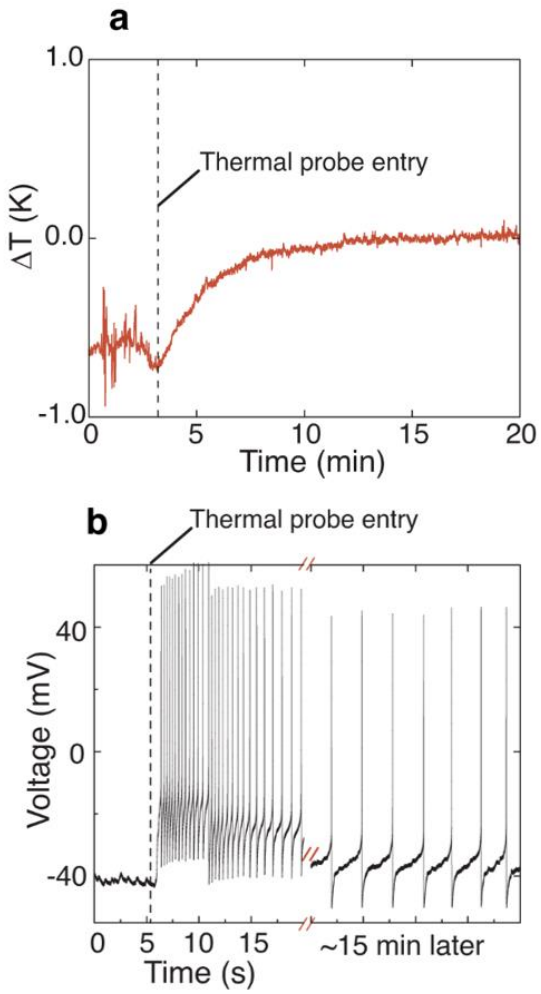

Figure 3.7 a) We show the temperature response from the microthermal probe as it penetrates the cell. After penetration into the cell, it takes about ~10 min for the temperature to stabilize. The rather long stabilization time (~10 min) can be attributed to saline warming up to room temperatures. b) The neuron produces high-frequency discharge following the thermal probe entry. After ~15 min, the discharge frequency reduces, and the resting membrane potential is partly recovered. All the experiments reported in this work were performed only after the temperature and electrical activity stabilized within the cell.

3.2.4 Statistics and reproducibility

Information on statistics and the number of trials are shown in the corresponding figure or figure captions. Where necessary, data points are representative of mean values with s.d. shown as error bars. *p* values were estimated using a *t*-test.

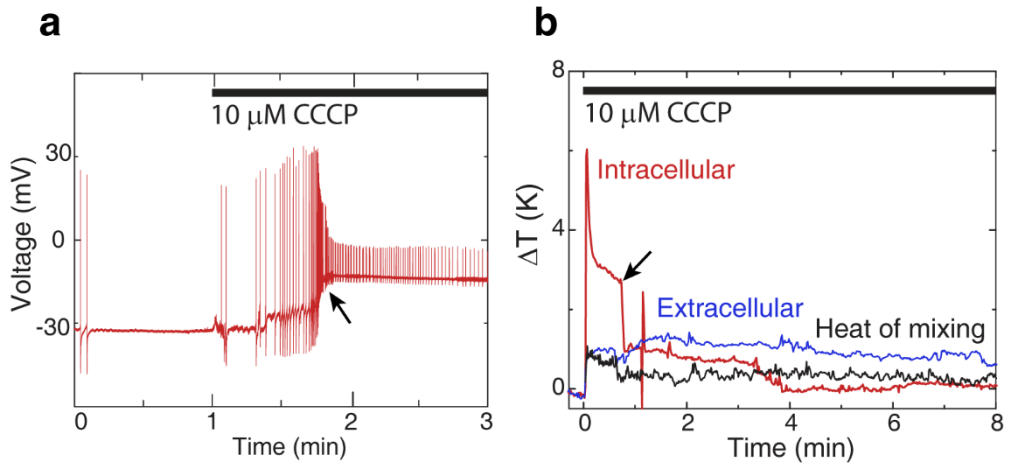

Figure 3.8 a) Representative intracellular voltage recording from a KCl electrode during the addition of CCCP (representation of n=2 experiments). The neuron was penetrated by the thermal probe at-least 30 min before CCCP addition. b) Temperature changes measured following CCCP exposure at t = 0 min. The initial intracellular temperature response ~6.1 K rise is higher than that of extracellular and saline response (heat of mixing). We mark an apparent depolarization event in black arrows that roughly occurred 1 min after CCCP exposure in both figures. This apparent depolarization could be from a combination of endogenous depolarization of the cell, and from electrode and thermal probe movement due to contraction of smooth muscle in the connective tissue. To avoid such off-target activities caused by the widely used proton uncoupler CCCP, we opted instead to use BAM15, a less cytotoxic proton uncoupler, to dissipate the mitochondrial proton motive force. Further, the maximum temperature rise of ~ 6.1 K from CCCP appears to be comparable to our experiments from BAM15 (Figure 3.11b), suggesting that heat from Ca^{2+} currents is negligible in comparison to proton currents.

3.3 Results

3.3.1 Identifying suitable reagents

Carbonyl cyanide m-chlorophenyl hydrazine (CCCP) is a widely known protonophore [53], [110] that is also a positive control [4], [22] for eliciting a temperature rise inside a cell (Figure 3.8). However, CCCP produces undesirable off-target [19], [111], [112] effects including cytotoxicity, which manifests in neurons as rapid membrane depolarization [111] (Figure 3.8a). In order to observe temperature changes that originate from proton motive force dissipation, we instead choose BAM15 (5-N,6-N-bis(2-fluorophenyl)-[1,2,5]oxadiazolo[3,4-b]pyrazine-5,6-diamine) [19] to uncouple protons. Unlike CCCP, BAM15 does not exert the same degree of off-target effects [19]. This is consistent with our observation of unperturbed neuronal membrane potential (Figure 3.9), which is also a confirmation that mitochondrial Ca^{2+} buffers were undisturbed [113]. Therefore, we used BAM15 (10 µM) throughout this study to dissipate the proton gradient.

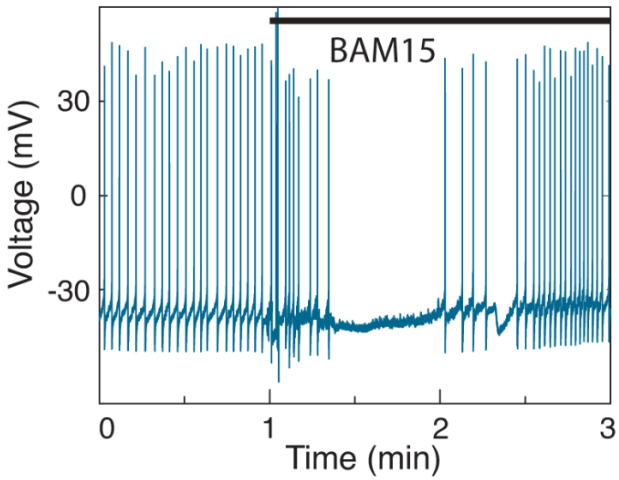

Figure 3.9 Representative plot of membrane potential before, during, and after the addition of 10 µM of the proton uncoupler BAM15 (n=6). The neuron was penetrated by the thermal probe before the addition of BAM15.

3.3.2 Identifying off-target heat sources

We first measured the heat of mixing BAM15 in a saline bath without cells. As shown in Figure 3.10, the heat of mixing could elevate the temperature by a maximum of 1.2 K ± 0.2 K (n=6) over ~10 min. Remarkably, the observed temperature rise of ~1.2 K from the heat of mixing without cells is comparable to a previously reported [21] temperature change (~1 K) from mitochondrial thermogenesis (on COS7 cells) that ignored contribution from the heat of mixing (Figure 3.10, Figure 3.8). To further characterize extraneous sources of heat, we measured the extracellular temperature rise due to BAM15 by placing the thermal probe immediately outside the membrane of a healthy neuron whose membrane potential was simultaneously recorded. At the extracellular level, the BAM15-triggered temperature elevations could be a result of bulk heating of all cells in the ganglion, and off-target effects from connective tissues, probes, and saline. As shown in Figure 3.10, the extracellular temperature increased to a maximum of 1.2 K ± 0.6 K (n=6), which then closely followed the response from the heat of mixing. We thus observed that extraneous heat sources can result in extracellular temperature changes that decay slowly with a time constant, τ_e = 7.93 min $\pm$ 3.62 min (shown in blue, Figure 3.10).

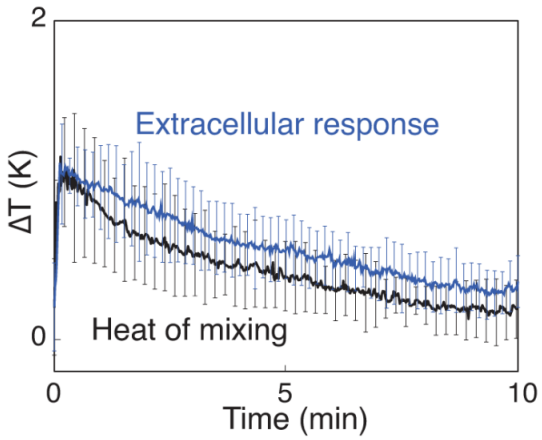

Figure 3.10 Control experiments with BAM15 show a maximum extracellular temperature rise of 1.2 K± 0.6 K that decays over ~8 min. Extracellular responses were measured with the thermal probe placed just outside the cell membrane of a target neuron (n=6). Heat of mixing between BAM15 and saline was measured in the absence of a ganglion (n=6).

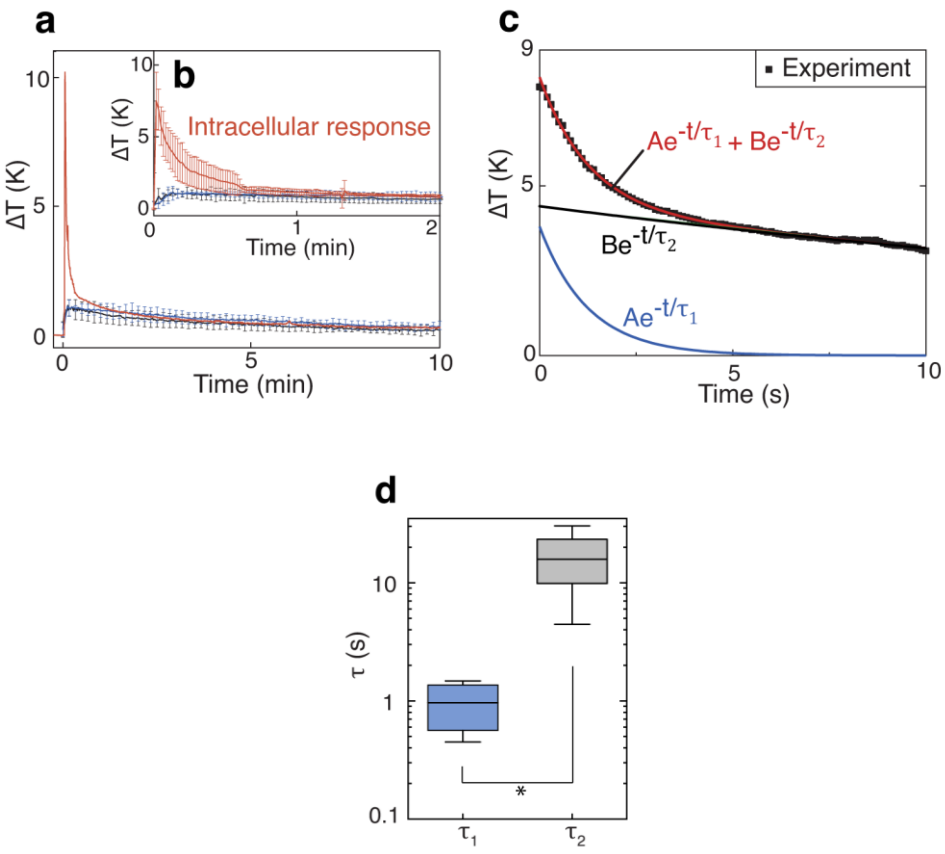

Figure 3.11: Identification of transient heat shock from mitochondrial proton uncoupling. a) Representative data for an intracellular response with 10 μM BAM15 is plotted (red) along with the control experiments (extracellular responses in blue, and heat of mixing in black). b) A statistically averaged intracellular response from n=6 trials is shown with the mean and the SD, and plotted along with control experiments. BAM15 responses begin at t =0 min. (p < 0.001 between intracellular and extracellular responses.) c) Representative ΔT measurement (n=6) following BAM15 exposure is fit to a biexponential function (red). The intracellular temperature signals are a mix of two exponential decays: one with a short time constant, τ_1, and other with a long time constant, τ_2. d) Time constants τ_1 and τ_2 (*p < 0.05) extracted from the measured ΔT data shown in Figure 3.11a. The data are represented on a logarithmic scale.

3.3.3 Intracellular responses to proton uncoupling

Once the thermal probe was inside the neuron (Figure 3.7), we measured the cell's response to the protonophore BAM15 (10 μM). In Figure 3.11a, a representative intracellular response (in red) to BAM15 shows a large temperature spike at time *t*=0 min. In the inset, Figure 3.11b, we show a statistically averaged intracellular response for the first two minutes following the addition of BAM15 (n=6). We observed a transient pulse of 7.5 K ± 2.0 K rise in intracellular temperatures after exposure to the proton uncoupler. On the other hand, control (Figure 3.10) and further experiments on vibration artifacts (Figure 3.12), and unhealthy cells (Figure 3.13), showed maximum $\Delta T \lesssim$ 2.3 K over 10 min. From the latter, we conclude that the temperature changes of 7.5 K ± 2.0 K in Figure 3.11b (shown in red, $p <$ .001) corresponded to specific intracellular responses to chemical proton uncouplers. We also observed that the temperature changes are roughly linearly proportional to the concentration of BAM15 we used (Figure 3.14). We analyzed the relative magnitudes and time constants of the signals to understand the origin of the temperature response. Shown in Figure 3.11c are representative data of the initial 10 s of thermal response to 10 μM BAM15. We fit the data to a biexponential curve $Ae^{-\frac{t}{\tau_1}} + Be^{-\frac{t}{\tau_2}}$ to separate the short-term transients from the rest of the signal. The obtained time constants are shown in Figure 3.11d. For the short-term component $Ae^{-\frac{t}{\tau_1}}$, we found A = 4.8 K ± 3.0 K with τ_1= 1.0 s ± 0.4 s. The component with the longer time constant ($Be^{-\frac{t}{\tau_2}}$) had B = 4.7 K ± 0.9 K and τ_2 = 16.6 s ± 9.2 s. The time constants of intracellular responses (τ_1, τ_2) are an order of magnitude shorter than those associated with extracellular measurements (τ_e).

3.4 Discussion

We first discuss the possible source of the temperature component $Ae^{-\frac{t}{\tau_1}}$. Any transients recorded in our experiments follow from transients in heat release and diffusion. Since the thermal time constant of the probe (~32 μs) [46] is much smaller than τ_1 and τ_2, any heat release in the vicinity of the probe invokes an instantaneous response at the probe. We find the temporal response of $Ae^{-\frac{t}{\tau_1}}$, with $\tau_1 \approx$1.0 s to be in close agreement with proton currents for which we calculated the time constant (τ_{H^+}) to be ~0.65 s from the data reported by Kirichok group [25]

(see Figure 3.2). Even though the duration of proton currents (τ_{H^+}) may vary across different cell lines, we find the time constant (τ_1) to have a similar order of magnitude as τ_{H^+} (Figure 3.2) [25], suggesting that $Ae^{-\frac{t}{\tau_1}}$ may arise from pmf dissipation in mitochondria, in close proximity to the probe.

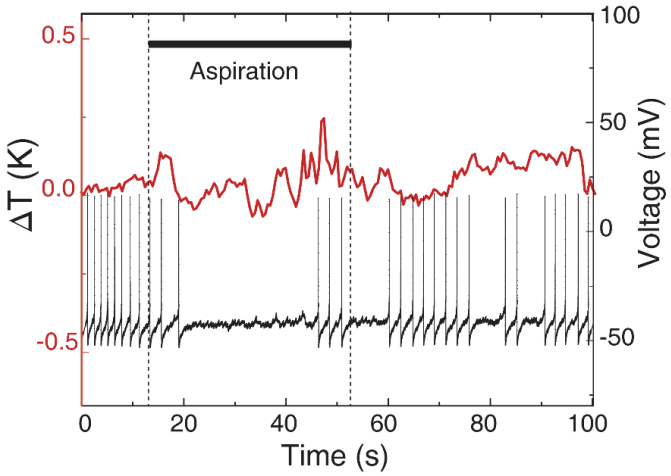

Figure 3.12 We emulate the injection and stirring of BAM15 by repeated aspirations of saline with an empty Pasteur pipette to observe the possible thermal artifacts arising from stirring. Temperature changes were measured inside a neuron using the micro-fabricated thermal probe. We also measure the intracellular electrical activity of the cell using a sharp microelectrode. Shown here is a representative response from stirring. No significant temperature or electrical activity changes were observed from repeated experiments (ΔT <0.5 K, n=6).

While the temporal response (τ_1) of the measured temperature change is consistent with predicted pmf dissipation time (τ_{H^+}), the magnitude of the temperature rise remains puzzling. A previous report [9] predicted a maximum temperature rise rate of ~4.8 K/s during pmf dissipation but assumed adiabatic conditions and ignored heat diffusion from the mitochondria. We can estimate the heat release rate ($\dot{Q}_p$) necessary to obtain the observed magnitude ($\Delta T = A \approx 4.8$ K) at our probe in the presence of heat diffusion. The temperature change occurred over a length scale of ~50 μm (Δx) along the length of the probe that has a cross-sectional area ($\Delta y \cdot \Delta z \sim 5$ μm^2). We can assume that temperature isotherms are spherically symmetric inside the cell given the similarity in the thermal conductivity (k) of the cell (~0.6 Wm^{-1}K^{-1}) [114] and the probe tip (k_{SiNx}~0.8 Wm^{-}

$^{1}K^{-1}$) [87] respectively. This leads to an estimated (initial) heat flow through the

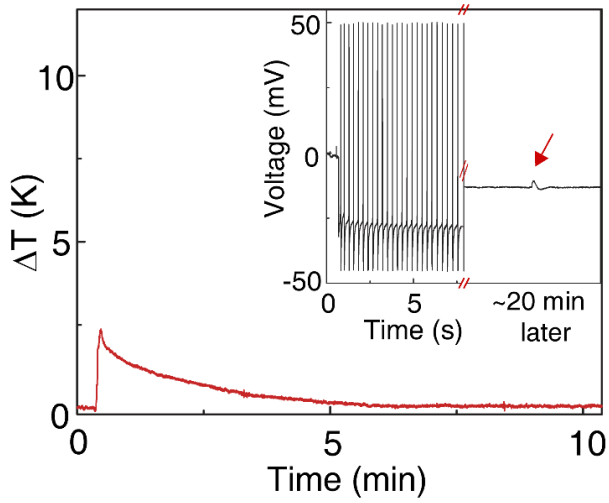

Figure 3.13 Intracellular response to BAM15 from a less viable cell shows a thermal shock of ~2.3 K, which is significantly lower than the mean ΔT ~7.5 K shown in Fig. 3.11a. This ganglion was kept refrigerated for ~3 days after removal from the host *Aplysia californica*. In the inset, the initial half of the electrophysiological recording shows that the resting potential is ~ -25 mV when the microelectrode entered the neuron. The latter half of the recording corresponds to conditions following thermal probe entry and before BAM15 addition. The neuron occasionally showed excitatory postsynaptic potential (shown in red arrow) but no action potentials, and the resting potential increased to ~ -13 mV. The electrophysiological recordings show that this neuron is less viable than usual. All the experiments reported in Figure 3.11 were from neurons that had a resting potential <-30 mV, with action potential magnitudes ~70 mV (representative data in Figure 3.9), which is typical for neurons that were tested within four hours after removal from the host *Aplysia*.

probe of $\dot{Q}_p \sim k_{SiNx}\, \Delta y\, \Delta z\, \Delta T/\Delta x$ ~400 nW. (We provide a more detailed analysis of the estimated heat flow through the probe in Chapter 4.) In comparison, the electrical heat at the onset of pmf dissipation from a single mitochondrion is ~20 pW ($\dot{Q}_{\mathrm{m}} \sim \Delta p \cdot I_{H^+}$) [9], which may be dependent on the cell lines, and the proton pool. The density of mitochondria in axons [115] can be as high as 0.6 μm^{-2}. However, in the soma of *Aplysia* neurons, there can be a reticulum [116], [117] of several functionally fused mitochondria as well as numerous individual mitochondria [118], [119]. A quantitative estimate of the typical number of mitochondria in the soma is not apparent [117]. Therefore, the gap between the

predicted heat ($\dot{Q}_{\mathrm{m}}$) and the measured heat flow ($\dot{Q}_p$) through the thermal probe could be due to the presence of numerous heat sources (mitochondria) that cannot be directly accounted for.

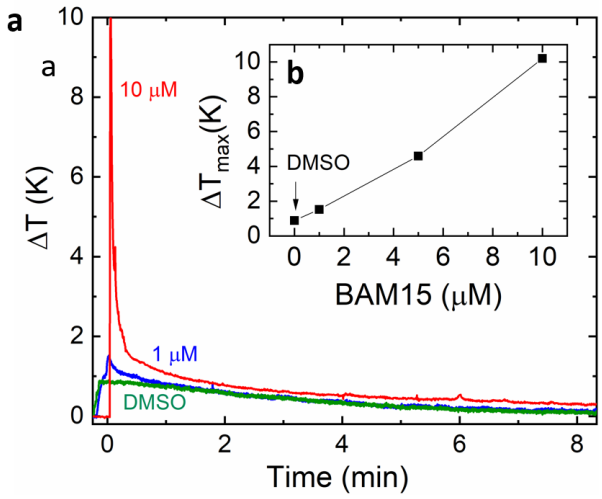

Figure 3.14. a) The effect of BAM15 concentration on the elicited intracellular temperature change is shown in this plot. We did not attempt to use BAM15 with > 10 μM concentration, since it resulted in precipitation when introduced into the saline. b) Inset shows the peak intracellular temperature change for every concentration of BAM15 we attempted. 0 μM BAM15 corresponds to the solvent DMSO.

We now discuss the second component of the temperature rise. The slower decay component, $Be^{-\frac{t}{\tau_2}}$ (with $\tau_2 \approx 16.6$ s) can arise from a combination of glucose catabolism, heat of mixing, and a cumulative response of pmf dissipation in mitochondria at sites that either had delayed exposure to BAM15 or were more distant from the probe. The latter could be due to a heat diffusion time (τ_D) of ~5 s ($\tau_D \sim L^2/D$, D = 0.2 $\mathrm{mm^2 s^{-1}}$) [114] across a cell of ~1 mm diameter. Previous reports of large temperature changes over prolonged durations of ~5 min or more [4], [21]–[23], [103], [104] have been criticized on the theoretical implausibility of the prolonged temperature rise and the inaccuracies inherent in the non-invasive measurement techniques used [24], [46], [56], [57], [63], [99]. Proton uncouplers like BAM15 and CCCP result in enhanced oxygen consumption and substrate oxidation that are typically sustained for ~20 min [19], [120], or more after exposure. Since we did not observe any appreciable intracellular temperature rise

beyond ~33 s ($2\tau_2$), we either did not have prolonged substrate oxidation in the mitochondria of *Aplysia* neurons, or the temperature rise from substrate oxidation was negligible as suggested by Baffou *et al* [24], [99].

The overall temperature rise observed in our experiment is on the same scale as those that have previously been shown to produce therapeutic heat shock responses by inducing heat shock proteins (Hsps) [121]–[124]. Hsps can protect against protein misfolding in disorders such as Huntington's disease, amyotrophic lateral sclerosis, and Parkinson's disease [123]. Moreover, heat shock can protect neurons from programmed cell death by apoptosis [124]. Previously, heat shock responses have been observed due to ~4 K rise within 30 s of heating [125] from a microscopy stage. In our work, the observed transient temperature rise ~7.5 K occurs intracellularly, which gives an added spatiotemporal advantage over external heating. Since the magnitude (~7.5 K) and time constant ($2\tau_2$~33 s) are comparable to the required conditions [125] for a heat shock response, the impact of stimulated pmf dissipation on secondary heat shock responses remains an open question for further study.

In this work, we used the proton uncoupler BAM15 to induce the mitochondrial proton gradient dissipation, which otherwise may not occur under normal physiological circumstances in *Aplysia* neurons. Possible targets for future investigations are natural thermogenic cells such as inguinal, epididymal, and brown fat cells [100] in which the uncoupling protein UCP1 is endogenously expressed. Such adipocytes may occasionally dissipate proton gradients using UCP1s, depending on the demand for heat production [97]. However, the thermal probe used in this work is too large (~5 μm wide) for measurements in adipocytes ($\lesssim$50 μm). Moreover, to measure the mitochondrial proton motive force (Δp), fluorescent probes for both the mitochondrial membrane potential ($\Delta\psi_m$) and the mitochondrial pH difference are required [54]. Existing fluorescent probes have undesirable effects that can result in electron transport chain toxicity [54], and temperature-[55] and plasma membrane potential ($\Delta\psi_p$)-dependence [54] of the measured mitochondrial potential $\Delta\psi_m$. Thus, future studies that can combine nonperturbative proton motive force (Δp) measurement with an electrically inert, smaller (<1 μm) invasive intracellular thermal probe may provide more information on endogenous heat release through pmf dissipation by UCP1.

In this work, we also experimentally attempted to measure the temperature changes during an action potential of a single neuron, which we explain in Appendix B. We accumulated data from >20,000 action potentials. By statistical

averaging, we find that the temperature changes during an action potential are possibly < 5 mK during an action potential and the ambient noise (of ~30 dB) in the measurements potentially obscured our results. Therefore, in the next chapter, we theoretically explore the expected temperature changes in cells, by developing a generalized heat transport model.

3.5 Conclusion

In summary, temperature measurements using an inert and high-speed microthermal probe reveal fundamental thermogenesis mechanisms that were previously missed in time-averaged fluorescence-based techniques [58], [59], [75]–[77], [79]. We observe a transient thermal shock of ~7.5 K at the onset of stimulated proton uncoupling. Upon decomposing the signal into individual components, we detect a component of the signal with a large magnitude (~4.8 K), and a small time constant (~1.0 s) that correspond well to the proton diffusion time scale during proton transport across the mitochondrial inner membrane. As the observed transient thermal shock (~4.8 K) dominates the steady-state processes, transient pmf dissipation stands out as a viable candidate for therapies targeting stimulated non-shivering thermogenesis. Further studies with biological UCPs could reveal additional insights for physiologically relevant pmf dissipation rates during endogenous homeostatic thermogenesis.

CHAPTER 4

CELLULAR THERMOMETRY CONSIDERATIONS FOR PROBING BIOCHEMICAL PATHWAYS

Temperature is a fundamental thermodynamic property that not only governs the rate of biochemical reactions but can also serve as a probe of such reactions. Consequently, extracellular thermometry studies identified certain thermoregulatory neuronal circuits and cancer metabolic pathways from a 1-2 K temperature increase in tissues, consistent with theoretical predictions. In contrast, previous intracellular thermometry studies are primarily disputed due to reports of > 1 K intracellular temperature rises over 5 min or more that contradict theoretical predictions. It remains unclear what insights intracellular thermometry could offer and under what circumstances it could do so. In this Chapter, we revisit the approach of intra-/extra-cellular thermometry and identify the conditions under which they could provide meaningful insights into the underlying biochemical reactions. We first develop a generalized framework for modeling cellular heat diffusion. Our model emphasizes the significance of thermal interfacial resistances that arise from the biomolecular complexes in the cellular milieu. We then use our model to find that the local intracellular temperature changes reach measurable limits only when exogenously stimulated. On the other hand, extracellular temperatures can be measurable (> 0.1 K) in tissues even from endogenous biochemical pathways. We provide a comprehensive approach to choosing an appropriate cellular thermometry technique by analyzing thermogenic reactions of different heat rates and time constants across a range of sub-cellular to tissue length-scales. Overall, this chapter provides clarity on the cellular heat diffusion modelling and the required thermometry approach for exploring thermogenic biochemical pathways.

4.1 Introduction

Cells contain a variety of biomolecular complexes ranging from proteins and nucleic acids to membranes and cytoskeleton to organelles such as lysosomes and mitochondria. Due to collisions with other macromolecular compounds in the cytosol, molecular diffusion in the cytosol has been estimated to be four times

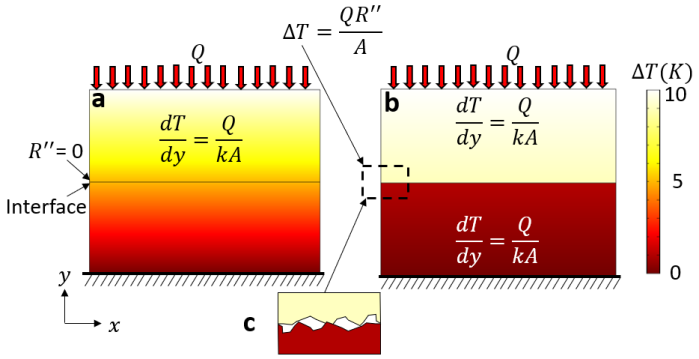

Figure 4.1 a) The temperature contour for an ideal interface between two dissimilar materials, with no interfacial resistance, is shown. b) The temperature contour due to a finite interfacial resistance (R'') results in a temperature discontinuity at the interface. c) Schematic of an interface between two dissimilar materials. Interfacial resistance (R'') could arise due to (1) the differences in vibrational and electronic states of the materials on either side of an interface, and (2) due to air gaps at the interface.

smaller than pure water [126]. The diffusion of heat, on the other hand, has been relatively unexplored at sub-cellular length-scales [24], [56], [57], [99], [127]. Resistance to heat diffusion not only stems from the intrinsic material resistance, but also due to dissimilar material interfaces (Kapitza resistance, R''_{TIR}) which often results in a discontinuous temperature jump across the interface [128]. We schematically explain this in Figure 4.1. Without an interfacial resistance R'', the temperature gradient due to a heat flow Q is linear (Figure 4.1a) across the two contacting materials. On the other hand, if there is a finite interfacial resistance R'', there will be discrete temperature jump across the interface (Figure 4.1b). The cellular milieu is home to numerous dissimilar interfaces from the biomolecular complexes suspended in the cytosol. Proteins are suspended in cytosol due to the hydrophilic side chains that are exposed to the water, while the hydrophobic chains are curled away from water. Such hydrophilic-water interfaces are expected to have thermal interfacial resistance (R'') of ~10^{-8} $K.m^2W^{-1}$ [129], [130]. For a hydrophobic-water interface, the interface resistance is typically higher and is

~2×10^{-8} K.m^{2}W^{-1} [131]. Highly hydrophobic materials such as carbon nanotubes have a thermal interfacial resistance of ~2×10^{-7} K.m^{2}W^{-1} with water [132]. The interfacial resistances (R'') from numerous biomolecular complexes are typically approximated through the use of an effective thermal conductivity for the intracellular region. By definition, an effective thermal conductivity (k_{eff}) represents the equivalent thermal conductivity of a medium, with no local interfacial resistances (R''), which produces the same temperatures or temperature gradients as that of a medium with a thermal conductivity k and interfacial resistance R''. We provide a more accurate definition of k_{eff} in Section 4.2. Since the interfacial resistances (R'') in intracellular regions are largely unknown, the effective thermal conductivity forms the basis of several intracellular and extracellular calorimetry techniques [7], [41], [42], and related theoretical bioenergetic calculations [24], [56], [57], [99], [127]. In the intracellular region, an effective thermal conductivity (k_{eff}) would approximately represent a combination of local interfacial resistances (R''_{TIR}), the resistance from the solute (proteins, k_p~0.1-0.2 Wm^{-1}K^{-1}) [133], [134] and the solvent (water, k_{med}~0.58 Wm^{-1}K^{-1}). When the interfacial resistances dominate the overall resistance to heat diffusion, the effective thermal conductivity (k_{eff}) would be less than that of proteins (k_p~0.1-0.2 Wm^{-1}K^{-1}). This could happen at sub-cellular length-scales and has recently been observed in an intracellular effective thermal conductivity measurement [135], which reported a k_{eff}~ 0.07-0.13 Wm^{-1}K^{-1}. When local interfacial thermal resistances dominate the overall resistance, the validity of k_{eff} has been questioned [57], [127], but it has never been fully explored. In this work, we show that a k_{eff} could become length-dependent, especially when the interfacial resistances dominate. Then, we systematically show how k_{eff} could fail to capture the true temperature changes, given a certain heat.

Temperature changes in organelles are dictated by both local thermal resistances and the magnitude of heat released. Previous non-invasive thermometry studies have reported steady-state changes of >1 K in the temperatures (ΔT) across intracellular organelles under endogenous conditions [4], [21]. However, we show in this work that irrespective of the local thermal resistance, under endogenous and physiological conditions, the steady-state temperature changes across intracellular organelles cannot exceed 10 mK. Further, we systematically show how endogenous thermogenesis amplifies the temperatures from a single-cell with a ΔT < mK to a ΔT~1-2 K in tissues of ~few mm length-scale. Our predictions are compared against bio-heat transport model [136], [137] that was previously developed for

tissue-scale heat transport. Overall, we connect the micro-scale cellular thermogenesis picture to macro-scale tissues, to provide insight on the length-scale dependence of thermal properties, expected heat release and temperature changes, and the role of blood perfusion. Given the increasing number of recent reports on intracellular thermometry [21]–[24], [56]–[59], [74], [99], [127], [135], we analyze the typical intracellular and extracellular temperature changes. We identify the appropriate length-, time-scales, and biochemical reactions where intracellular thermometry could provide valuable information.

Our theoretical investigation on the length-scale dependence of thermal properties and temperature changes would be useful in applications that require the functional relationship between heat input and temperature to be known a priori. This includes applications such as nanoparticle heating of cryopreserved tissues [138], [139], thermal ablation of tumor cells [140]–[142], thermometry-based bioenergetics studies [20], [41], [42], [46], etc. To this end, we organize our work as follows. In Section 4.2, we introduce an approximate thermal resistance network model for cellular heat diffusion. There is no unique way to represent cellular heat diffusion, but we show that our approximate model can still reasonably capture the thermal property variation across all length-scales. Using our resistance network model, in Section 4.3, we show that the effective thermal conductivity approximation could result in under- or over-prediction of temperatures at length-scales where the interface thermal resistances dominate. Despite local thermal interfacial resistances, we show in Section 4.4 that endogenous heat sources are insufficient to raise the local temperatures of organelles by more than 10 mK. We then show how the tissues produce sufficient temperature changes of 1-2 K which contribute toward thermoregulation during cold climatic conditions. In Section 4.5, we explore different thermometry techniques to identify which biochemical pathways can be measurable. We separately treat steady-state and transient temperature changes to identify which thermometry scheme would be best suited for a given biochemical reaction.

4.2 Equivalent thermal resistance network

4.2.1 Defining a resistance network:

Figure 4.2a shows a partial picture of the cellular components across a ~0.1 μm^2 area near the cell wall [143]. The cytoskeleton components such as Actin, intermediate filaments, and microtubules are roughly 6 nm, 10 nm, 25 nm in

diameter [144]. A steady-state heat diffusion across this subcellular space is subjected to a thermal resistance from the medium (t/k_{med}), the intrinsic resistance of proteins in the filaments (t/k_p) and the interfacial resistances of the filaments

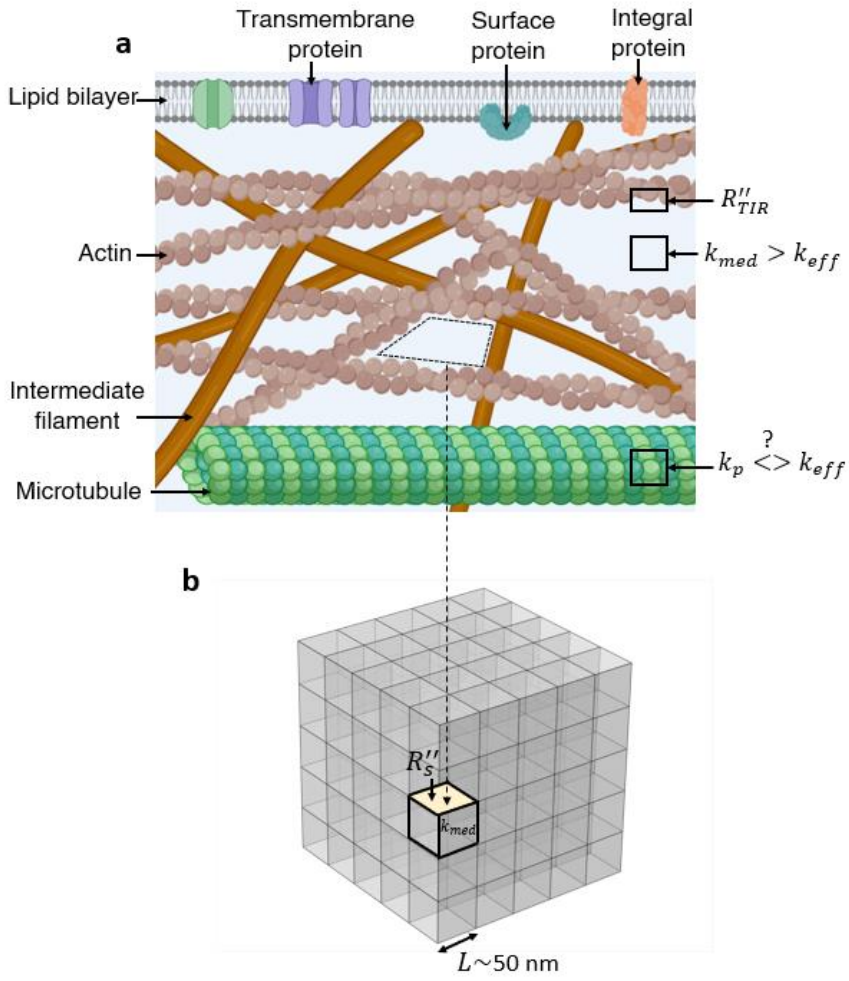

Figure 4.2 a) Schematic of typical cytoskeleton components in a roughly 0.1 μm^2 area near the cell wall. k_{eff} is the effective thermal conductivity of all the components shown here. If k_p>k_{eff}, the thermal interfacial resistance (R''_{TIR}) dominate the k_{eff}. b) A simplified representation of the thermal resistance network. The medium is assumed to have a thermal conductivity of k_{med}, surrounded by surfaces on all sides with a resistance of R''_s (K.m^{2}W^{-1}). The image was custom made using biorender.com and obtained with permission.

(R''_{TIR}), where t is the corresponding thickness. The thermal resistance network in the cellular environment can be visualized as numerous pockets of polyhedrons (filled with water) surrounded by protein chains. This can be approximated as cuboidal pockets of medium surrounded by surfaces of proteins with a lumped

resistance R_S'', as shown schematically in Figure 4.2b. The validity and impact of this approximation are discussed later, but we first explain the physical meaning of this lumped resistance R_S''. The resistance R_S'' can be assumed to be a lumped representation of all the intracellular components and their interfacial resistances. A mathematical representation of R_S'' could be:

$$R_S'' \approx A \sum_i \frac{t_i}{k_{p_i} A_i} + \frac{R''_{TIR_i}}{A_i} - \frac{t_i}{k_{med} A_i} \tag{2}$$

where, t_i is the thickness of a lipid/protein/organelle i with a thermal conductivity k_{p_i}, effective surface area A_i, with an interfacial resistance R''_{TIR_i}, and A is the surface area of the individual unit (~L^2) along which R_S'' is borne (Figure 4.2b). The last term in Eqn. (2) is to account for the reduction in the medium's resistance due to the displacement of the medium by the material i. Any advection thermal resistance can also be considered to be a part of Eqn. (2). We henceforth call this resistance R_S'' as equivalent thermal resistance at a length-scale L, since from Eqn. (2) we can see that R_S'' is a strong function of the length-scale ~At_i/A_i. At a length-scale of L~50 nm, R_S'' is representative of the resistances from protein chains; whereas, at a length-scale L~50 μm, R_S'' represents all the proteins in the cell as an equivalent lumped resistance at the cell-wall. Thus, R_S'' can be higher at 50 μm than at 50 nm. We now discuss the implications of a cuboidal resistance network approximation. Unless stated otherwise, we assume in this work that the pockets are filled with a medium, whose k_{med} = 0.58 $Wm^{-1}K^{-1}$, corresponding to that of water. The real picture could be better represented by a k_{med} that is < 0.58 $Wm^{-1}K^{-1}$, due to the dispersed proteins and ions, and R_S'' could be $\sum_i R_{TIR_i}$, instead of Eqn. (2). However, since an accurate spatial distribution of k_{med} and R''_{TIR} is not available for a heterogeneous cellular environment, we assume that all the additional resistances are lumped along the surface as R_S'' (Eqn. (2)). Further, we assume a rectilinear topology (cuboid) for the unit cell of the resistance network as shown in Figure 4.2b. The real topology could be complex (with entangled resistance network and high interfacial resistances) or simpler (with a homogenous dispersion of proteins and low interfacial resistances). Our cuboidal resistance network may not be a unique representation, but we show in this work that it serves as an example to understand the cellular heat diffusion picture.

4.2.2 Defining an effective thermal conductivity:

To test the feasibility of the cuboidal resistance network, we first define an effective thermal conductivity. An effective thermal conductivity, k_{eff}, approximates the local thermal resistances such that under a known amount of steady heat transport (Q), the temperature change (ΔT) can be predicted using a single thermal property, k_{eff}. The effective thermal conductivity is a function of the type of heat input (line, surface, or volumetric) [145], and the location of the temperature measurement. Typically, the measured temperatures can be volume averaged (T_{v-av}), surface average (T_{s-av}), volume maximum (T_{v-m}), or surface maximum (T_{s-m}). For bio-heat transport studies, especially for calorimetry-based bioenergetics studies, a

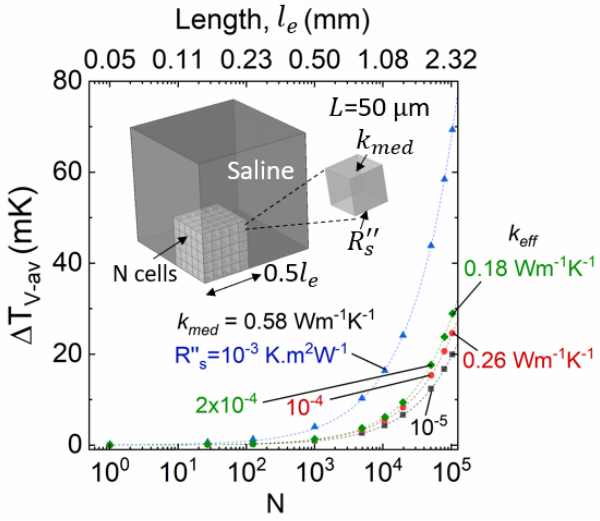

Figure 4.3. Volume averaged temperature change (ΔT_{v-av}) of the stack of cells is plotted against the number of cells, N, in the stack. The total edge length of the stack of cells is given by l_e, which is ~$(NL)^{0.33}$, where L is the length of each cell surrounded by R_s''. The ΔT_{v-av} are shown for 4 combinations of k_{med} and R_s'', as shown inside the graph. For lengths, l_e> 1 mm, the plotted ΔT_{v-av} also correspond to a stack of cells with an effective thermal conductivity, k_{eff}, as noted outside the graph using the corresponding colors. Each cell is assumed to release heat of 2.5 nW. Only 1/8th of the domain is shown in the schematic.

useful and an often-measured parameter is the average temperature in a volume (T_{v-av}). Such temperatures could be representative of an average temperature measured using fluorescent dyes, or dispersed nanoparticles. If the heat input is known (say, endogenous heat source, or laser), the average temperature change can

be used to estimate the local effective thermal conductivity, k_{eff} [135], [146]. Thus, in this current study, we assume k_{eff} as the effective (or measured) thermal conductivity calculated using the volume averaged temperature (T_{v-av}) for a known volumetric heat source. We later discuss how the location of temperature measurement and the type of heat source affect the effective thermal conductivity k_{eff}. If k_{eff} is known, we denote the temperature changes as ΔT_{keff}, calculated using the known k_{eff}. Similarly, we denote the temperature changes predicted using the cuboidal resistance network (k_{med} and R_s'', Figure 4.2b) as ΔT_R. In this work (in Section 4.3), we show that ΔT_{keff} deviates from ΔT_R at small length-scales, especially if $k_{eff} < k_p$, in which case ΔT_R is also representative of the true temperature changes.

4.2.3 Testing the cuboidal resistance network:

Using the above-mentioned definition of effective thermal conductivity, k_{eff}, we now discuss how the cuboidal resistance network can reasonably approximate k_{eff} that were previously measured experimentally. We begin by considering cellular and tissue length-scales, and then discuss the feasibility of approximation at sub-cellular length scales.

Consider a stack of N cuboidal cells (Figure 4.3), representing a multi-cellular tissue. Each cell has an edge length, L=50 μm, roughly corresponding to an adipose cell size [147]. The cells are filled with a medium of thermal conductivity k_{med}, surrounded by an equivalent surface resistance, R_s''. The stack of cells is surrounded by saline. A constant outer surface temperature (20°C) is assumed at the saline far from the tissue. At large length scales, $l_e \gg R_s'' k_{med}$, where $N \to \infty$, the effective (or measured) thermal conductivity of the tissue can be analytically approximated as,

$$k_{eff} = \frac{L}{R_S'' + \frac{L}{k_{med}}} \tag{3}$$

We computationally confirm the effective thermal conductivity approximation (Eqn. (3)) using Figure 4.3. We use finite element simulations that were validated for interfacial resistance modelling in our previous work [46], [148], [149] and for transients modelling in the Appendix C. A volumetric heat of 2.5 nW is assumed to be released per cell, which corresponds to a typical cell metabolism rate [41],

[150]. We plot in Figure 4.3 the volume-averaged temperature change (ΔT_{v-av}) in the cell stack against the number of cells, N, in the stack. ΔT_{v-av} is plotted for different equivalent resistances, R_s'' from 10^{-3} to 10^{-5} K.m^{2}W^{-1}. We also plot the corresponding temperature changes without an equivalent resistance R_s'', but with an effective thermal conductivity k_{eff} (0.18 and 0.26 Wm^{-1}K^{-1}), for l_e> 1 mm, as marked outside the graph in Figure 4.3. We specifically choose a k_{eff} of 0.18 Wm^{-1}K^{-1} and 0.26 Wm^{-1}K^{-1} since previous studies report the effective thermal conductivity for adipose tissues to be in the range 0.18-0.26 Wm^{-1}K^{-1} [137], [151]. From Figure 4.3, we find that the predicted temperatures (ΔT_{v-av}) using k_{eff} of 0.18 Wm^{-1}K^{-1} and 0.26 are indistinguishable from the predicted ΔT_{v-av} for a cuboidal resistance network with k_{med}=0.58 Wm^{-1}K^{-1}, R_S'' of 2×10^{-4} and 10^{-4} K.m^{2}W^{-1}, respectively. In other words, a k_{eff}= 0.18-0.26 Wm^{-1}K^{-1} that was previously measured for adipose tissues is equivalent to a tissue made up of cells of L=50 μm each with a k_{med}=0.58 Wm^{-1}K^{-1} and $R_s'' = 2\times10^{-4} - 10^{-4}$ K.m^{2}W^{-1}, respectively, as also predicted by Eqn. (3). Further, from our previously published experimental data, we find that an equivalent resistance R_s'' of 3×10^{-4} K.m^{2}W^{-1}–7×10^{-4} K.m^{2}W^{-1} at L= 50 μm (Appendix C.2) is able to capture our experimentally measured temperatures at cellular length-scales. Thus, the cuboidal resistance network consisting of k_{med} and R_s'' reasonably approximates the thermal properties at tissue and cellular length-scales.

At sub-cellular length-scales, a recent report [135] measured the thermal conductivity to be 0.07-0.13 Wm^{-1}K^{-1} with a spatial resolution of 200 nm inside a cell. Since the measured k_{eff} is less than protein's thermal conductivity, k_p (~0.1-0.2 Wm^{-1}K^{-1}), the interfacial resistances (R_{TIR}'') possibly dominated at sub-cellular length-scales. We approximated the cellular heat diffusion picture to a cuboidal resistance network specifically to account for the interfacial resistances (R_{TIR}''). Consequently, a low k_{eff} can be explained using the cubic resistance network if the lumped resistance R_s'' is in the range 10^{-7}-10^{-6} K.m^{2}W^{-1} (Appendix Figure C.4) at L~ 50 nm. Therefore, the cuboidal resistance network can provide a reasonable approximation to the thermal properties at all length-scales. In the next section, we show in detail how the cuboidal resistance network could simultaneously explain the effective thermal conductivity at different length-scales.

4.3 Length-scale dependence of thermal properties

The effective thermal conductivity, k_{eff}, could be a function of the length-scale at which it was estimated (Figure 4.4), especially if the local thermal interfacial resistances dominate the total thermal resistance. If the local thermal resistances (R_s'') are in the order of 10^{-4} K.m^{2}W^{-1} at a length-scale of 50 µm, the effective thermal conductivity is a strong function of the length scale varying from 0.05 Wm^{-1}K^{-1} to 0.25 Wm^{-1}K^{-1}, over 50 µm to 2 mm. Figure 4.4 suggests that the effective

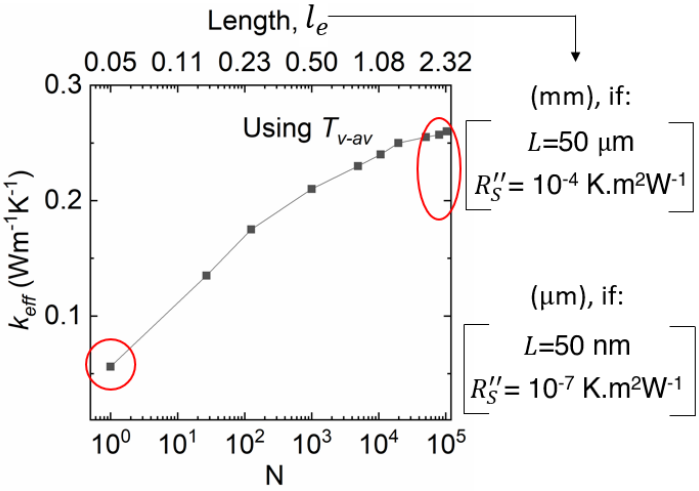

Figure 4.4. Effective thermal conductivity (k_{eff}) is a function of the length-scale at which it is measured. We find the k_{eff} at each length scale, l_e, by matching the volume averaged temperature (T_{v-av}) for a stack of N cells with a resistance network of k_{med} and R_s'' to that of a stack with a k_{eff}. We assumed a constant volumetric heat of dissipation per cell. The shown plot is true for two different scenarios: (1) R_s'' = 10^{-4} K.m^{2}W^{-1} for a length-scale of L=50 μm for the cells, or (2) R_s'' = 10^{-7} K.m^{2}W^{-1} for a length-scale of L=50 nm. The unit for the top-axis is mm or µm, respectively. The region in red corresponds to some of the previous experimental data points [135], [137], [151].

thermal conductivity could be as low as ~0.05 Wm^{-1}K^{-1} at cellular length-scales (~50 µm), which is in close agreement with a recent report [135] of intracellular k: 0.07-0.13 Wm^{-1}K^{-1}. Further, from a fit to our previous experimental data, we approximately estimate an effective thermal conductivity of ~0.05-0.07 Wm^{-1}K^{-1} at cellular length-scales (~50 µm). We mark the experimentally reported thermal conductivities in red circle in Figure 4.4 at N~1. For adipose tissues, the thermal conductivity is typically in the range 0.18-0.26 Wm^{-1}K^{-1} [137], [151], which is also

highlighted in red in Figure 4.4 at larger length-scales (l_e~2 mm) where the effective thermal conductivity saturates. Notably, our resistance network model provides a link between the thermal conductivities at two different length-scales. The data shown in black line in Figure 4.4 corresponds to our specific assumption of a cuboidal topology for the resistance network. In general, the true functional relationship between effective thermal conductivity and length-scale could be determined by mapping the true topology of the resistance network in the system. Our cuboidal topology serves as an example to show that the local interfacial resistances could be responsible for the reduction in effective thermal conductivity at smaller length-scales.

The equivalent resistance (R_S'') is responsible for reducing the effective thermal conductivity at lower length-scales. The value of this resistance R_S'' scales directly with the length-scale (L), as evident from Eqn. (3). A resistance, R_S'', of ~10^{-4} K.m^{2}W^{-1} at a length-scale L=50 μm may seem high; however, it scales down to an equivalent resistance, R_S'' of ~10^{-7} K.m^{2}W^{-1} at a length-scale L=50 nm, where the contribution of R''_{TIR_i} can no longer be ignored in R_S''. At sub-cellular length scales ~50 nm, if the local resistance R_S'' is on the order of 10^{-7} K.m^{2}W^{-1}, k_{eff} could vary from 0.05 Wm^{-1}K^{-1} to 0.25 Wm^{-1}K^{-1} over length scales of 50 nm to 2 μm (Figure 4.4). The interfacial resistance (R''_{TIR}) contribution to the lumped resistance R_S'' cannot be ignored at a length-scale l_e where $R_S'' \sim \sum_i R_{TIR_i} \sim l_e/k_p$ could be all in similar orders of magnitude. The exact length-scale l_e at which R''_{TIR} dominates cannot be known for certain since we do not have any information on the TIR of multiple interacting protein chains or organelles. So, in the following section, we look at two different range of length-scales: 50 μm – 2 mm and 50 nm – 2 μm separately to identify the possible impact of assuming an effective thermal conductivity (k_{eff}) where the thermal interfacial resistances could be dominant.

4.3.1 Consequences of using effective thermal conductivity:

In this section, we look at the potential consequences of assuming an effective thermal conductivity in the cellular medium. Typically, if a temperature change, say T_{v-av}, is known, the heat release (Q) can be estimated if the thermal conductivity is also known. Conversely, if the heat input (Q) is known, the temperature change (say T_{v-av}) can be predicted if the thermal conductivity is known. Throughout section 4.3, we utilize the latter for convenience: we try to predict the temperature change for a known amount of heat input Q, assuming that

the effective thermal conductivity is also known. Our analysis can be similarly extended to the former functional relationship as well. Specifically, in this section, we analyze the impact of using an effective thermal conductivity (k_{eff}) to predict temperature changes at (1) small length-scales, and (2) when $k_{eff} \ll k_{med}$ due to high interfacial resistances.

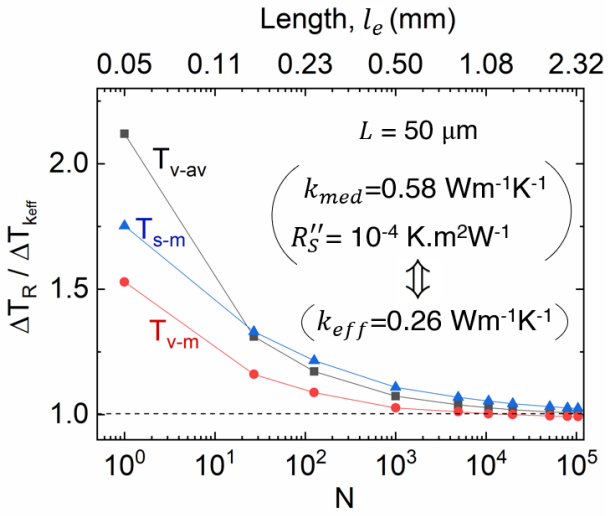

Figure 4.5. The discrepancy in the predicted temperature as a function of the number of cells, N, in the stack. At a length-scale, l_e~ 2 mm, an effective thermal conductivity of 0.26 Wm^{-1}K^{-1} is equivalent to a stack of cells of length L~ 50 μm, with a k_{med}=0.58 Wm^{-1}K^{-1} surrounded by R_S''=10^{-4} K.m^{2}W^{-1}. The predicted temperature change using k_{eff} is denoted by ΔT_{keff}, and the corresponding temperature change predicted by k_{med} and R_S'' network is denoted by ΔT_R. s-m: surface maximum, v-m: volume maximum, v-av: volume average.

If we use an effective thermal conductivity, which was previously measured at l_e (say, 2 mm), in length-scales smaller than l_e, the temperature changes could be under-predicted. Figure 4.5 shows the magnitude of under-prediction in ΔT at cellular length-scales (~50 μm) when using a k_{eff}, which was measured at tissue length-scale l_e (~2 mm). ΔT_R corresponds to the predicted temperature change using a combination of k_{med} and R_S'' for a cell of length L, while ΔT_{keff} corresponds to the temperature change assuming an equivalent effective thermal conductivity for the cell (k_{eff}). The ratio $\Delta T_R/\Delta T_{keff}$ is independent of the magnitude of heat released (Q). Since k_{eff} was assumed to be determined using the temperatures measured at l_e~ 2 mm, both the models predict the same temperature changes at l_e ~ 2 mm (Figure 4.5). However, at lower length-scales

(lower N), the temperature changes predicted using an equivalent k_{eff} for the entire cell is lower than that predicted using k_{med} and R_s'' by a factor of up to 2 at a single cell. If ΔT_R is representative of true temperature change in a cell, then a k_{eff} measured at l_e~ 2 mm cannot be used at l_e~ L=50 μm. Notably, the converse is also true. If an effective thermal conductivity was measured at l_e~ L=50 μm, then using the same k_{eff} at l_e~ 2 mm will over-predict the true temperature change (Figure 4.6).

The error in predicting the true temperature could be higher if the effective (or measured) thermal conductivity, k_{eff}, is lower than that of the medium, k_{med} and proteins, k_p. This is true especially at length-scales lower (or higher) than that used to measure k_{eff}. As an example, consider k_{eff} as the effective thermal

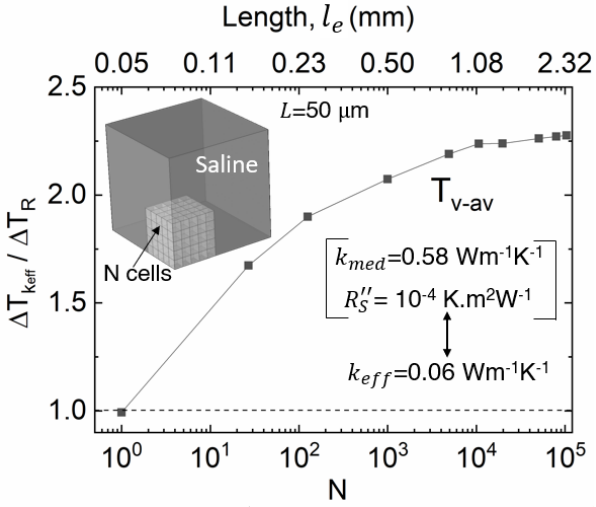

Figure 4.6 Using k_{eff} estimated at cellular length-scales (l_e=L=50 μm) can over-predict the temperature changes at tissue length-scales (2 mm). The k_{eff} at 50 μm length-scale is ~0.06 Wm^{-1}K^{-1}, which is equivalent to a k_{med}=0.58 Wm^{-1}K^{-1} and a cuboidal resistance R_S'' = 10^{-4} K.m^{2}W^{-1}. The predicted temperature change using k_{eff} is denoted by ΔT_{keff}, and the corresponding temperature change predicted by k_{med} and R_s'' network is denoted by ΔT_R

conductivity measured at a length-scale l_e~ 1 μm. At smaller length-scales, say at 50 nm (=L), the predicted temperature using k_{eff}, which is ΔT_{keff}, could be 5 times lower than the true temperature (ΔT_R) if k_{eff}~ 0.07 Wm^{-1}K^{-1} (Figure 4.7). Such a low k_{eff} of 0.07 Wm^{-1}K^{-1} is within the range of previously measured values ([135] and Appendix C.2). The lower the measured k_{eff}, the higher is the potential for discrepancy. Since a k_{eff} of 0.07 Wm^{-1}K^{-1} is less than protein's thermal

conductivity, k_p (~0.1-0.2 $Wm^{-1}K^{-1}$), the interfacial resistances (R''_{TIR}) possibly dominates the overall resistance (R''_S). At length scales of 50 nm (=L), to reduce the effective thermal conductivity from k_{med} to a k_{eff}~0.05-0.2 $Wm^{-1}K^{-1}$, the relevant equivalent resistance (R''_S) has to be in the range of 10^{-7}-10^{-6} Km^2W^{-1}, which could be dominated by R''_{TIR} from hydrophobic-water interfaces. The plots shown in Figure 4.7 is generalizable to any length-scale (L), and the above argument is for a specific case where L = 50 nm. Therefore, the error in predicting the true temperature could be higher if we use an effective thermal conductivity $k_{eff} \ll k_{med}$, where the interfacial resistances R''_{TIR} could dominate the overall thermal resistance.

We note here that throughout this work we assumed the true temperature change to be ΔT_R, corresponding to a cuboidal resistance network, which is one of the many possible topologies. The real picture could be worse (with entangled resistance network and high interfacial resistances) or better (with a homogenous

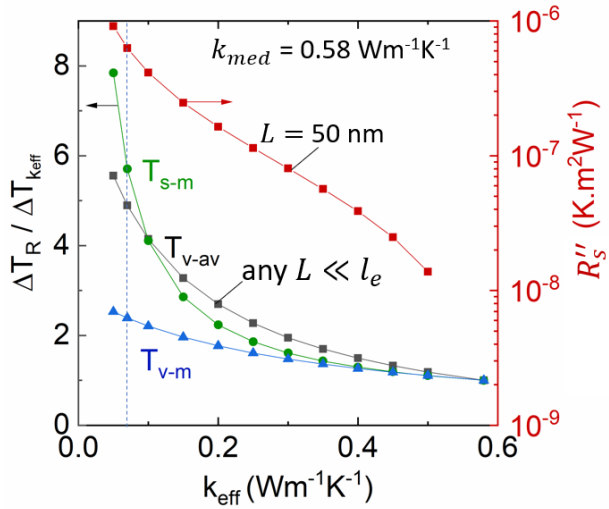

Figure 4.7. The discrepancy in the predicted temperature as a function of the effective thermal conductivity k_{eff} that was measured at l_e. At a length-scale L ($\ll l_e$), the true temperature (ΔT_R) deviates from ΔT_{keff} if the k_{eff} is lower than k_{med} (=0.58 $Wm^{-1}K^{-1}$ here). The discrepancy in T_{s-m}, T_{v-av}, are T_{v-m} are plotted on the left axis. The equivalent resistance R''_s at L=50 nm is plotted on the right axis.

dispersion of proteins, low cell packing density, and low interfacial resistances). The former is more likely since it could potentially reduce the effective thermal conductivity to values below that of typical proteins (Figure 4.4).

4.3.2 Reexamining the use of effective thermal conductivity:

By definition, the effective thermal conductivity, k_{eff}, is also dependent on the type of input heat source (volumetric or surface), and the location of the measured temperature. For calorimetric studies, we assumed that a k_{eff} is typically measured using the average temperature change over a volume (ΔT_{v-av}) for a known

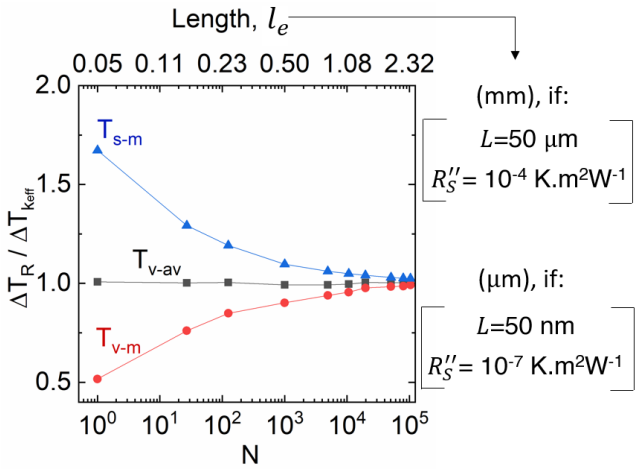

Figure 4.8. Effective thermal conductivity (k_{eff}) cannot capture the temperature gradients at smaller length-scales. We use the k_{eff} shown in Figure 4.4, for this plot. This plot is true for two different scenarios: (1) R_S'' = 10^{-4} K.m^{2}W^{-1} for a length-scale of L=50 µm for the cells, or (2) R_S'' = 10^{-7} K.m^{2}W^{-1} for a length-scale of L=50 nm. The unit for the top-axis is mm or µm, respectively. s-m: surface maximum, v-m: volume maximum, v-av: volume average.

volumetric heat input, Q. However, if the length-scale l_e of effective thermal conductivity k_{eff} measurement is in the order of L, the length-scale of local resistances (R_S''), the k_{eff} approximation may fail to capture the true local heterogeneity in the temperatures (ΔT_R), as shown in Figure 4.8. If the effective thermal conductivity is defined using the average temperature (ΔT_{v-av}), the true local surface temperatures (ΔT_{s-m}) could be higher by 67%, or the true overall maximum temperature (ΔT_{v-m}) could be lower by 51% for the conditions shown in Figure 4.8. Similarly, an effective thermal conductivity k_{eff} could not simultaneously capture our previous experimental temperature measurements inside and outside of a cell (Appendix C.2). Only at length-scales $l_e \gg L$, as shown in Figure 4.8, an effective thermal conductivity could capture the local temperature heterogeneities.

To understand why k_{eff} fails to capture the true heterogeneities in temperature changes, we provide few temperature contours in Figure 4.9. The left panel (Figure 4.9a-c) corresponds to the true temperature changes due to a thermal interfacial resistance R_S'' of 10^{-4} K.m^{2}W^{-1} at the outer surface of a cell with a k_{med}=0.58 Wm^{-1}K^{-1}. The right panel (Figure 4.9d-f) are the respective temperature

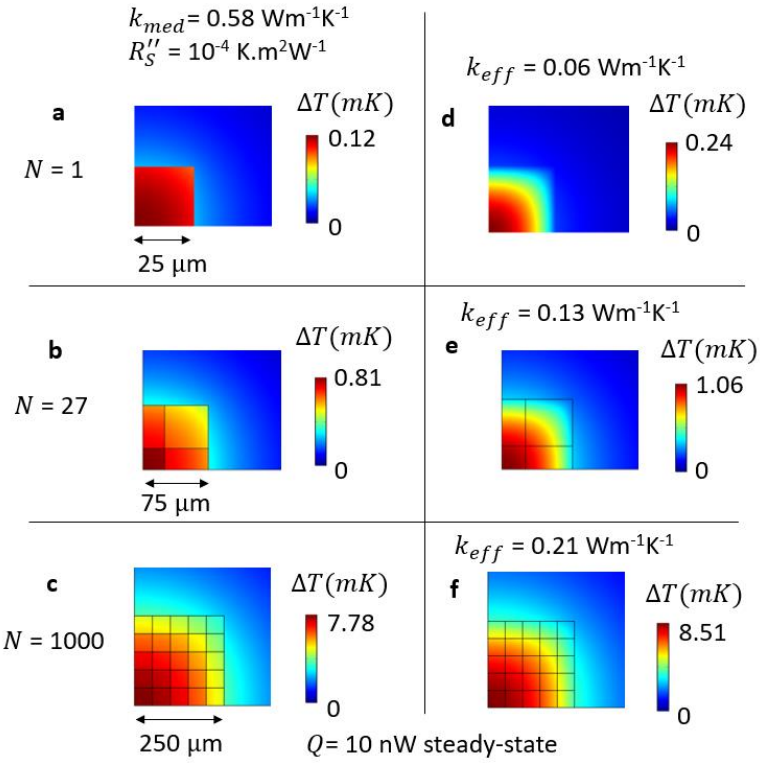

Figure 4.9 a)-c) Temperature contours when the cell has a surface resistance R_S'' of 10^{-4} K.m^{2}W^{-1} with a k_{med} of 0.58 Wm^{-1}K^{-1}. d)-f) Temperature contours due to an equivalent effective thermal conductivity k_{eff} and no surface resistance. The effective thermal conductivity k_{eff} used here corresponds to the data plotted in Figure 4.4. A heat of 10 nW is released per cell (L= 50 µm). Only 1/8th of the domains were simulated, utilizing symmetry. k_{eff} can capture the temperature heterogeneities only when the length scale $l_e \gg L$.

contours due to an equivalent effective thermal conductivity (k_{eff}, plotted in Figure 4.4) that was calculated using the volume averaged temperature (T_{v-av}). The volume averaged temperatures (T_{v-av}) are equal for the two cases in each row of the panel (i.e., ΔT_{v-av} is the same for Figure 4.9a and d; Figure 4.9b and e; Figure 4.9c and f), which is also plotted in Figure 4.8. Even though the effective thermal conductivity (k_{eff}) approximation ensures that the volume averaged temperatures

are matched (Figure 4.8), k_{eff} fails to capture the true temperature heterogeneities at length-scales $l_e \sim L$, as evident from the temperature contour differences in Figure 4.9.

Typical calorimetry techniques [41], [42] for biological cells measure the temperature of the surrounding medium to estimate the total heat released from a cell. Such techniques inherently assume an effective thermal conductivity for the cell and the surrounding medium during the calibration of the thermal resistance of the calorimetry cell using an external heater. We discussed in this section that the effective thermal conductivity is a function of the location of the heat source, the location of the measured temperature, and the local interface resistance network (Figure 4.8). Since the resistance to heat flow for an external heater may be different in comparison to any intracellular heat sources, calorimetry techniques [41], [42] may not be able to capture the true intracellular heat release via externally measured temperatures.

Throughout Section 4.3, we used a cuboidal resistance network with k_{med} and R_s'' at different length-scales L and l_e, to understand the possible discrepancies that could result from approximating the local thermal resistance (R_s'') as an effective thermal conductivity (k_{eff}). We assumed a constant k_{med} of 0.58 $Wm^{-1}K^{-1}$ corresponding to water (k_{water}) and concentrated all the resistances from the proteins or organelles to be at R_s''. However, realistically, cellular heat diffusion could be from a combination of k_{med} ($< k_{water}$, due to a homogeneous distribution of proteins and ions) and R_s'', where $R_s''(=\sum_i R_{TIR_i})$ could be less than that used in Figures 4.2-4.9. Similarly, the increase in thermal conductivity at large length-scales could be due to low packing density of cells in tissues. Further, lipid bilayers and other proteins undergo phase change near room temperatures [152], [153], which may influence the local thermal resistances. For instance, the resistance R_s'' that we extracted from our previous experiment (Appendix C.2) is potentially higher due to intermediate phase changes. In addition, certain biological structures can change their morphology and surface characteristics [154]–[156] dynamically due to strain or hydration. Thus, the effective thermal conductivity (k_{eff}) of biological milieu may likely depend not only on the length-scale but also on the configuration, temperature, etc. We refer the readers to other engineering instances [149], [157]–[159] where thermal interfaces play a dominant role, and how they are typically measured [148], [158], [160]. Likewise, future intracellular thermometry studies can provide insights on the length-scale and temperature dependence of thermal properties (k_{eff} and R_s'') by measuring the local temperature changes

across a range of length-scales 50 nm – 100 µm using a certain known heat input. Spatial distribution of the local thermal interfacial resistances can be known if spatial temperature distributions can also be measured across the cellular medium.

4.4 Typical endogenous temperature changes

4.4.1 Organelle-scale steady-state temperature changes:

In the previous section, we discussed the potential impact of effective thermal conductivity assumption and found that the local temperatures (ΔT_{keff}) could be under-predicted relative to the true temperature changes (ΔT_R) due to interfacial resistances. We limited our analysis to the ratio of temperature changes ($\Delta T_R/\Delta T_{keff}$), which is independent of the magnitude of heat (Q). In this section, we look at the absolute magnitude of the temperature changes (ΔT_R) in organelles with interfacial resistances. An estimate of the typical temperature changes in organelles could help determine the sensitivity of measurement techniques to observe intracellular temperature changes.

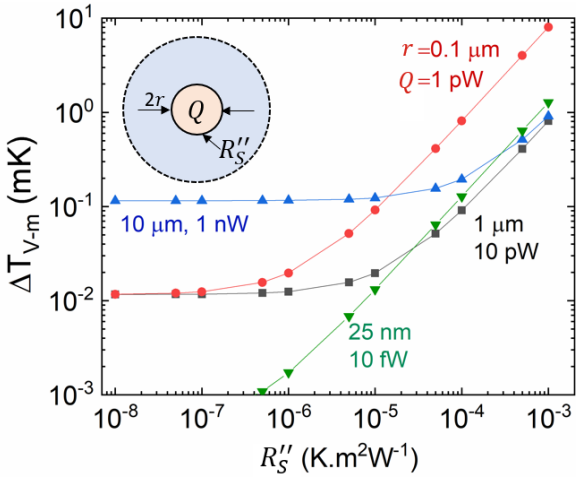

Figure 4.10. Maximum temperature changes of an organelle as a function of its equivalent surface resistance, R_s''. The schematic shows an organelle of radius r, with a surface resistance R_S'' in an infinite medium dissipating heat Q. A conservative thermal conductivity of k_{med}=0.1 Wm^{-1}K^{-1} was assumed for the organelle and the medium.

The magnitude of temperature change (ΔT) is governed by both the thermal properties (k_{med} and R_s'') and the magnitude of heat release (Q). Endogenous heat release in cells are in the range of 1–10 nW from a 50 µm cell (~1-20 kW/m^3) [41],

[137], [150]. Assuming the total heat release to be concentrated (~0.2- 200 MW/m^3) in organelles or organelle clusters (~0.05-20 μm), we show in Figure 4.10 that even with a high thermal resistance of 10^{-3} $K.m^2W^{-1}$, the maximum intracellular temperature increases are expected to be less than 10 mK under steady-state physiological conditions. On the other hand, exogenously applied stimulants such as proton uncouplers (BAM15, CCCP), laser, resonating magnetic nanoparticles, etc. can be used to increase the heat in cells by several orders of magnitude (Appendix C.2 and [7], [20], [139], [161]). Only under such stimulated conditions, the intracellular temperature changes can exceed 10 mK. Under physiological and endogenous circumstances, the heterogeneity in intracellular temperature is therefore expected to be $\ll$ 10 mK at steady state in isolated cells. Overall, despite high interfacial resistances of cellular components, the intracellular temperature changes in organelles are expected to be less than 10 mK unless they are stimulated exogenously.

4.4.2 Tissue-scale thermogenesis:

A few nanowatts of intracellular heat cannot raise the temperature of a single isolated cell by a few mK as evident from Figure 4.3 and Figure 4.10. However, it is well known that brown adipose tissue (BAT) cells contribute toward increasing the local temperatures by 1-2 K [47], [48], especially under cold-induced conditions. In this section, we systematically show how the temperature changes amplify from a single cell to a tissue length-scale by extrapolating our cubic resistance network for cells and comparing it against a bioheat transport model for tissues.

For a typical heat of 2.5 nW per cell, we previously discussed using Figure 4.3 that the average temperature increases with the number of cells, N. The temperature changes, ΔT_{V-av}, in Figure 4.3 roughly follows a power-law, $\Delta T_{V-av} \propto N^{\gamma}$, where $\gamma = 0.63$-0.67, which is consistent with previous analytical estimates [24], [162]. By extrapolating this fit, in Figure 4.11a, we predict the corresponding temperature changes at tissue length-scales of ~20 mm. The thermal conductivity of adipose tissue is typically in the range of 0.18-0.26 $Wm^{-1}K^{-1}$. The corresponding ΔT_{V-av} is expected to be in the range of 2-3 K for a tissue of size ~ 20 mm (Figure 4.11a). We compare this prediction to a 3D bio-heat transport model that was developed for tissues to include the effects of blood perfusion. Details of this model are available in previous studies [136], [137], and also in

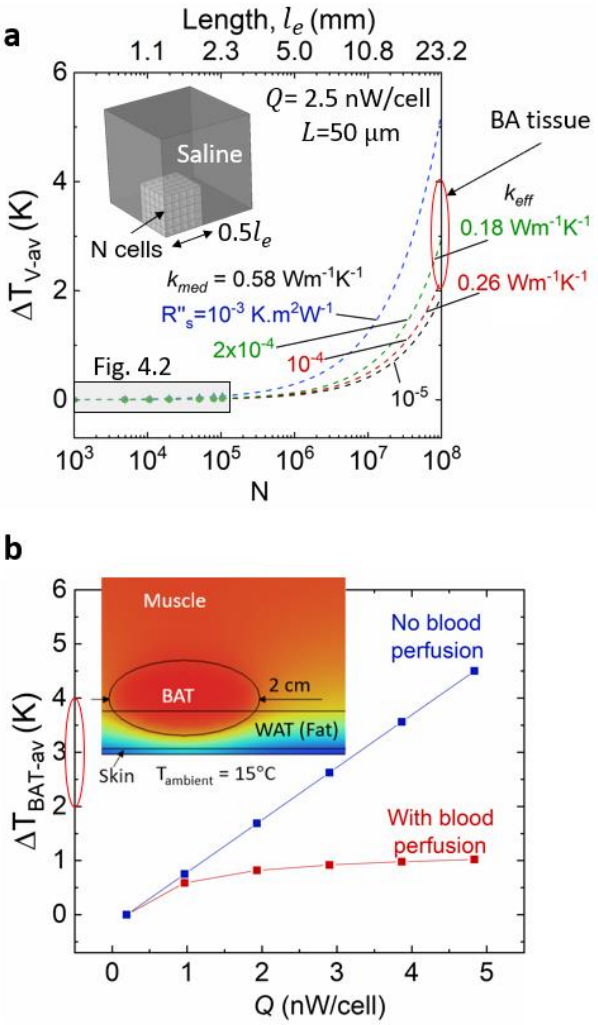

Figure 4.11. a) Average temperature of the stack of cells increases with the number of cells, N, and reaches ~2-4 K at a length-scale of ~20 mm. We extrapolated these curves from Figure 4.3. b) Average temperature change in the BAT deposit is shown for 5, 10, 15, 20, 25-fold increase in BAT metabolism. The x-axis shows the heat released in the tissue in nW per cell (of dimension 50 µm x 50 µm x 50 µm). The "no blood perfusion" case assumed ω_b to be zero. More details on this bio-heat transport model can be found in Appendix C.4.

Appendix C.4. Briefly, the bioheat transport model accounts for volumetric metabolic heat production (Q'''_{met}) at tissues and blood associated thermoregulation (Q'''_{blood}). The blood perfusion rate is expressed as ω_b in s^{-1}. The volumetric heat supplied or removed by the blood is then given by, $Q'''_{blood} = \rho_b \omega_b C_b (T_b - T)$,

where C_b is the specific heat capacity, ρ_b is the density of the blood, T_b is the arterial blood temperature, and T is the local tissue temperature. In Figure 4.11b, we use the bio-heat transport model to predict the expected temperature changes in brown adipose tissue (BAT) deposits during a cold-induced ($T_{ambient}$=15°C) thermogenesis. BAT volumes vary depending on age, location, and weight of the individual. Here, we choose a 2 cm^3 ellipsoidal BAT as representative of supraclavicular region [137], [163], [164]. We used previously reported thermal and physical properties for blood, fat (BAT and WAT), and muscle, which we also summarize in Table C.1 in Appendix C. Our previous prediction of ΔT_{v-av}~2-3 K rise in a stack of cells (Figure 4.11a) is equivalent to a scenario in BAT (Figure 4.11b, Q=2-3 nW/cell) with no blood perfusion. Notably, we were able to predict the temperature change in tissues by using a framework built from single cells (with k_{med} and R_s'') each producing ~2.5 nW of heat. The ΔT from a stack of cells (Figure 4.11a) did not include the effects of blood transport. Blood perfusion is responsible for the nutrient transport required to sustain the thermogenesis. Considering the effects of blood perfusion, we expect the tissue's temperature to rise by ~1 K (Figure 4.11b). This is also consistent with previous experimental reports that studied thermoregulatory circuits to find a maximum temperature change in the order of ~1-2 K in BAT deposits [47], [48]. Therefore, what starts out as a few mK temperature change in an isolated cell (~50 μm), could result in a 1-2 K change at tissue length-scales of ~10 mm.

4.5 Choosing the right thermometry technique

In this section, we examine intracellular and extracellular temperature changes during endogenous biochemical reactions to explore when the temperature changes can be above the detection limits. We perform this analysis over a range of length-scales l_e by varying the number of cells N, as shown in Figure 4.12 and Figure 4.13. We define ΔT_{int} as the maximum intracellular temperature that could be measured through intracellular probes (say nanoparticles or molecular probes) inside a single cell at the surface of a tissue of N cells. We define ΔT_{ext}, as the temperature measured by an extracellular probe (say RTD or thermocouple) of 50×50×50 μm^3 size, which is at the surface of a tissue of N cells. We first compare the steady-state temperature changes (ΔT_{int} vs. ΔT_{ext}) across a range of length-scales and heat release rates. We then compare the transient temperature changes (ΔT_{int} vs. ΔT_{ext}) across a range of length- and time-scales.

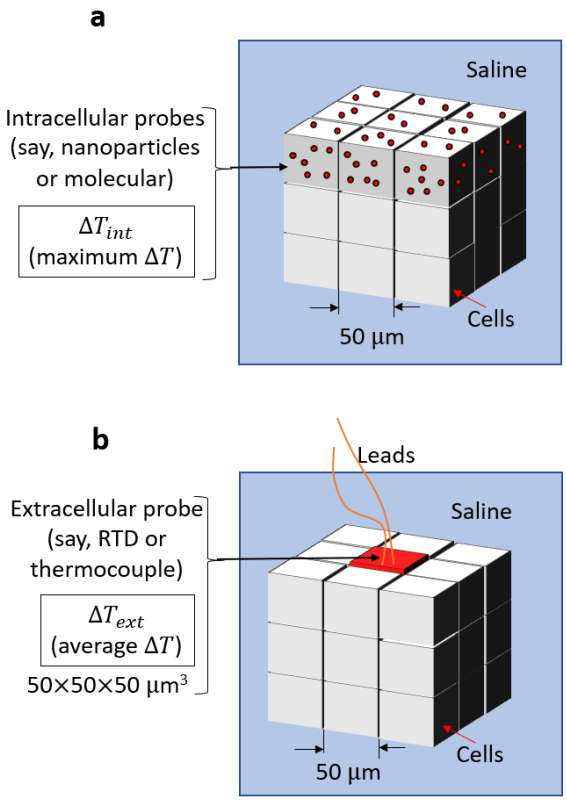

Figure 4.12 a) Schematic of an intracellular temperature measurement is shown, defining ΔT_{int} as the maximum intracellular temperature from a cell at the surface of N number of cells. b) Schematic of a typical extracellular temperature measurement is shown, defining ΔT_{ext} as the extracellular temperature measured at a location of size (50×50×50 μm^3), replacing one cell with the extracellular probe.

4.5.1 Steady-state temperature changes

We compare the steady-state temperature changes expected to be measured by extracellular (ΔT_{ext}) and intracellular (ΔT_{int}) probes, in Figure 4.13. We assumed a steady heat release of 10 nW per cell of size 50 µm, typical of brown adipose tissue cells under cold-induced thermogenesis. From Figure 4.13, we find that the ΔT_{ext} and ΔT_{int} closely follow each other on the scale of 0 to 100 mK over a range of length-scales. However, if we observe the ratio $\Delta T_{int}/\Delta T_{ext}$, it reaches a

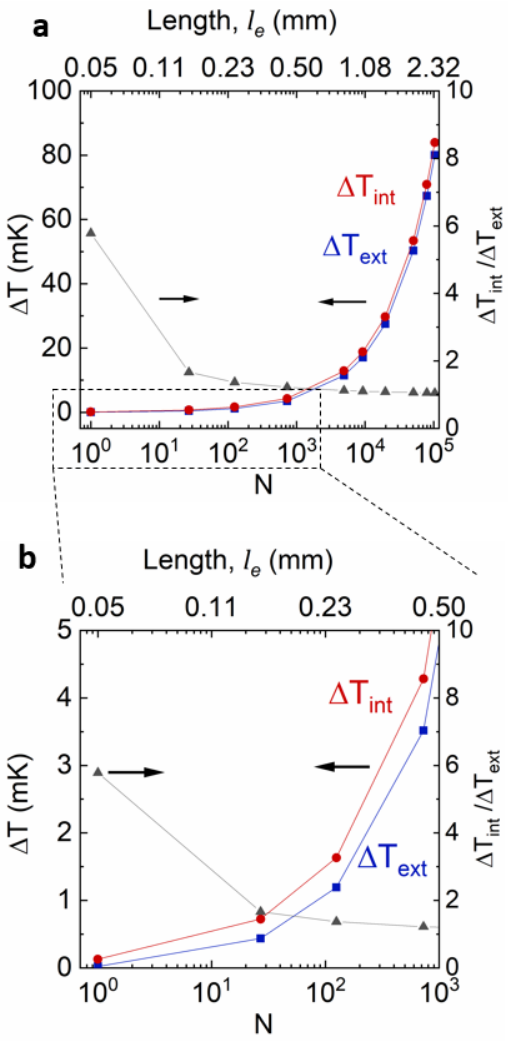

Figure 4.13 a) The simulated extracellular (ΔT_{ext}, blue points) and intracellular (ΔT_{int}, red points) temperature changes during endogenous thermogenesis (10 nW, steady-state per cell) are plotted on the left y-axis. The ratio $\Delta T_{int}/\Delta T_{ext}$ (black points) are plotted on the right y-axis. b) The temperature changes over N=1 to 1000 is plotted separately to clearly show the magnitude of temperature changes at small length-scales. Even though the intracellular temperature changes are up to 5.8 times higher than extracellular temperature changes in an isolated cell, the magnitude of temperature changes is sub-mK. We assumed the cell to have edge length L=50 μm. The ratio $\Delta T_{int}/\Delta T_{ext}$ is independent of the magnitude of heat.

maximum of about 5.8 when N=1, or in an isolated cell. We find the ratio $\Delta T_{int}/\Delta T_{ext}$ to remain under 2 for N>25 cells. This shows that using an intracellular probe to measure temperature changes is advantageous, especially if the number of

cells in the study is less than 10. In other words, intracellular probes could be useful for *in vitro* studies in a petri dish setting, where the temperature changes inside a cell could be up to 5.8 times higher than that outside of a cell. This is also evident from our stimulated mitochondrial proton uncoupling study reported in Chapter 3.

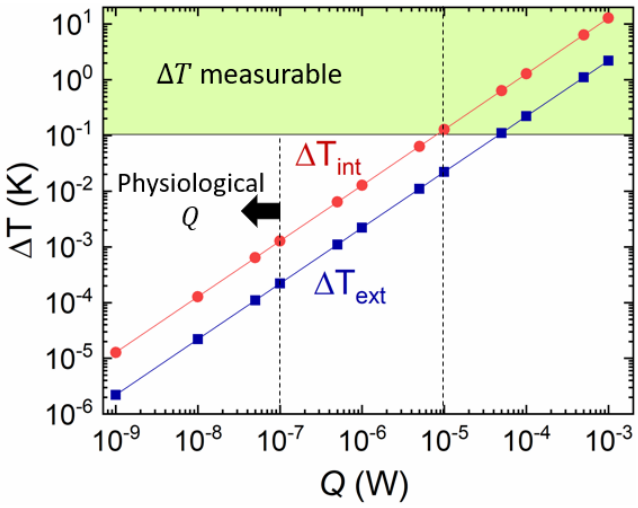

Figure 4.14 For a single isolated cell in an infinite saline medium, the intracellular (ΔT_{int}, red) and extracellular (ΔT_{ext}, blue) temperature changes are plotted for various steady-state volumetric heat release rates, Q. Typical physiologically epxected heat release rates are < 100 nW. Typical intracellular temperature measurement range is > 0.1 K, in an *in vitro* petri dish setting.

Even though intracellular temperatures could be 5.7 times higher than extracellular temperatures in an isolated cell, the absolute magnitude of steady-state physiological temperature changes is in the order of 0.1 mK (Figure 4.13b). The absolute magnitude of temperature changes is strongly governed by the amount of heat released and local thermal resistances. For the temperatures reported in Figure 4.13, we used a nominal resistance R''~ 10^{-4} K.m^{2}W^{-1}, and a heat release per cell of ~10 nW, which, for instance, corresponds to cold-induced thermogenesis in brown fat cells [137]. Since the temperature changes in < 10 cells are < 1 mK, they are typically not measurable, unless the cells are isolated and thermally insulated through multiple vacuum chambers [41], [42]. On the other hand, the temperature changes amplify with the length-scale as evident from Figure 4.13. At larger length-scales, the extracellular probe could very well measure the maximum thermogenesis induced temperature changes, and there is little advantage to using intracellular probes at larger length-scales (> 1 mm). Therefore, extracellular

temperature probes could provide useful physiological information on thermogenesis-related activities at larger length-scales in the order of tissues that are > 1 mm. This is also evident from previous studies that utilized mm-scale thermometers to study thermoregulatory neuronal circuits [47], [48], and cancer metabolism [49]–[52].

Under physiological and steady-state conditions, intracellular temperature changes are usually limited to sub-mK values, which are not directly measurable in a petri dish setting by intracellular probes, unless the cells are thermally isolated by vacuum chambers. However, if the intracellular heat release can be stimulated by external agents, the intracellular temperature changes can reach measurable limits, as we show in Figure 4.14. We plot the expected steady-state temperature changes (ΔT_{int} and ΔT_{ext}) in an isolated cell sitting in an infinite water bath, for a range of uniform volumetric heat release Q inside the cell. Conservatively, any physiological heat release rate is < 100 nW [41], [42], [137], [150] as marked in the Figure 4.14. To increase the expected temperatures to measurable limits (conservatively, 0.1 K), the intracellular heat release needs to be stimulated exogenously to > 10 μW. Our stimulated mitochondrial proton uncoupling (reported in Chapter 3, and Appendix C.2) is one such example, where the heat release is stimulated by an external proton uncoupler. Only when the intracellular heat release is stimulated, such intracellular thermometry techniques can provide useful physiological information about the stimulated biochemical reaction. Therefore, intracellular temperature probes could be useful for steady-state measurements *in vitro*, especially if the intracellular heat release could be stimulated exogenously.

4.5.2 Transient temperature changes:

Biochemical reactions such as proton motive dissipation, action potential generation, synaptic transmission, etc. are transient reactions that occur over $\ll 1$ s. To observe the length-scale dependence of transient heat releases, we plot the maximum volumetric temperature change (ΔT_{V-m}) in Figure 4.15, for a transient release with a time constant, $\tau \sim 3$ s. Typically, steady-state temperature changes increased with the number of cells as $\sim N^{\gamma}$. However, we find that the transient temperature changes do not necessarily increase with length-scale beyond a few mm. We fit a logistic curve $\Delta T_{V-m} = \frac{-a}{1+\frac{N^{\gamma}}{N_0}} + b$, shown in dashed lines, to the points plotted in Figure 4.15. We find that the $\Delta T_{V-m} \to 24$ mK as $N \to \infty$. This is

expected since the heat diffusion length-scale ($L_D \sim \sqrt{D\tau} \sim$ 1 mm) is finite and is dependent on the duration of the heat release (τ). The temperature changes may not increase beyond a length-scale $l_e \gg L_D$. Further, we observe that the time it takes to reach the maximum temperature also increases with the number of cells (Figure 4.15b). Overall, we expect the transient temperature changes to be localized, limited to a region defined by the heat diffusion length-scale (L_D).

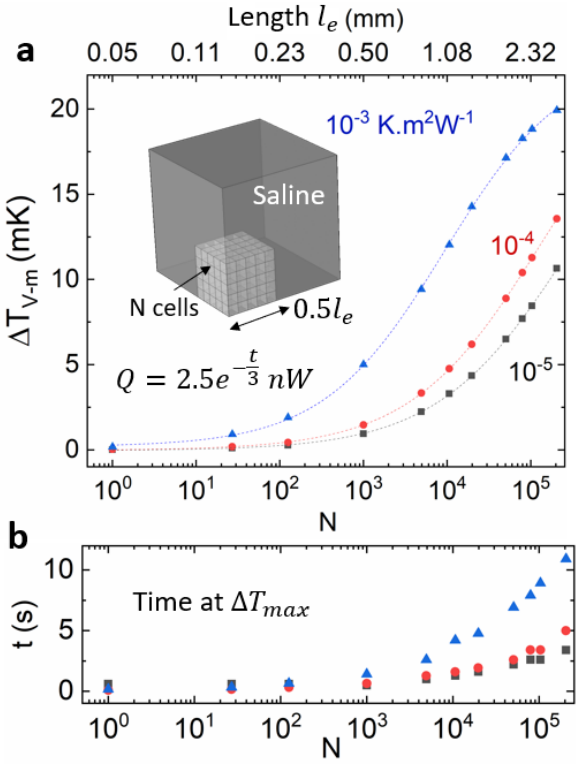

Figure 4.15 a) Maximum temperature in the volume (ΔT_{V-m}) is plotted for a transient heat release (τ=3 s) in cells across different length-scales. The inset shows the domain of simulations. Transient temperature changes saturate and do not monotonically increase with the number of cells N. The temperatures plotted here correspond to the maximum temperature change over a time t =0 to 20 s. b) The time t at which the temperature ΔT_{V-m} reaches a maximum is plotted for the same range of length-scales and R_S''. The length of a unit cell was L = 50 μm.

Given that the transient temperature changes are localized, we can expect the intracellular temperature changes to be more pronounced than the extracellular changes at smaller timescales of heat release (τ). In Figure 4.16, we plot the

intracellular (ΔT_{int}) and extracellular (ΔT_{ext}) temperatures, defined as in Figure 4.12, for a single isolated cell in an infinite medium, releasing heat Q at different timescales (τ). As expected, we find the ratio $\Delta T_{int}/\Delta T_{ext}$ to increase from 5.8 (~for steady-state conditions) to up to 18 at a timescale of τ=1 ms for the heat release. Therefore, intracellular thermometry could be useful in isolated cells *in vitro*, especially if the heat release is expected to be transient with a timescale $\ll$ 1 s.

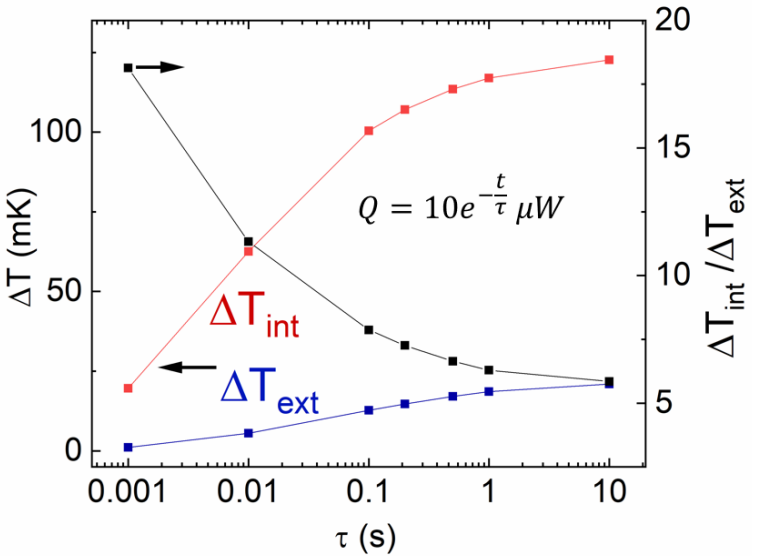

Figure 4.16: The intracellular (ΔT_{int}, red) and extracellular (ΔT_{ext}, blue) temperature changes are plotted along the left y-axis for a transient heat release in an isolated cell in an infinite saline medium. The ratio $\Delta T_{int}/\Delta T_{ext}$ (black points) are plotted along the right y-axis. The ratio $\Delta T_{int}/\Delta T_{ext}$ is independent of the magnitude of heat.

It is worthwhile to note here that we attempted to experimentally measure the transient temperature changes during an action potential in *Aplysia* neurons. We explain it in detail in Appendix B. Since the action potential generation is a recurring event, especially if stimulated by a depolarizing current, we collected the temperature data for over 20,000 action potentials from a single neuron. We repeated this for several neurons. Since the temperature measurements are noisy, we averaged the temperature changes from 20,000 action potentials by having a fixed window of time for averaging the data from an action potential. Upon averaging, we observed that the temperature changes were ~5 mK during an action potential. Even though we could obtain a signal to noise ratio of > 3 from a few neurons (n=2), for data from several other neurons (n=4), we could not measure any temperature change. Our data is likely obscured by the room temperature

fluctuations, as evident from a comparable-temperature change (~ 3 mK) even in control experiments. Overall, our attempt to measure transient temperature changes during an action potential shows us that the physiological intracellular temperature changes are < 10 mK and they are challenging to measure *in vitro,* and without any exogenous stimulation that could produce > μW of heat.

In this section, we explored different thermometry techniques to see when the temperature changes can be measurable. By exploring a range of parameters such as length-scales, timescales, and expected heat release rates, we conclude the following:

1. Intracellular thermometry could be useful in a petri dish setting for *in vitro* studies, especially if the expected intracellular heat release is stimulated exogenously and is transient in nature occurring over < 1 s.
2. Extracellular thermometry could be useful to observe physiologically relevant and endogenous thermogenesis, especially in tissue scales (> 1 mm length-scale).

In this work, in Chapters 2-3, we developed an intracellular thermometry technique and observed a transient heat release due to stimulated mitochondrial proton uncoupling, which is consistent with scenario 1 mentioned above. The latter, extracellular thermometry, has been proven useful in previous studies to map the thermoregulatory neuronal circuits [47], [48] and cancer metabolism [49]–[52], through sutured mm-scale thermometers. In the rest of this work, we attempt to advance the latter – tissue-scale extracellular thermometry. To this end, in Chapter 5, we develop a wireless thermometry technique using magnetostriction sensors to measure the temperatures at tissue-length scales. We highlight the advantages and limitations of using a magnetostriction-based technique, and in Chapter 6, we provide ways to advance this further to a tissue-scale temperature mapping.

4.6 Conclusion

In summary, we first theoretically explored the effective thermal conductivity approximation in a cellular medium to find that it may not be suitable if the local thermal interfacial resistances dominate. This is particularly true at sub-cellular length scales where local interfacial resistances can be in the order of 10^{-7}-10^{-6} $K.m^2W^{-1}$, which could result in an effective thermal conductivity (k_{eff}) substantially lower than the medium (k_{med}) and proteins (k_p). Subsequently, the

effective thermal conductivity (k_{eff}) becomes length-scale dependent owing to the interfacial resistances. We explained the reduction in thermal conductivity at lower length-scales using a cuboidal topology for the resistance network; the true functional relationship can be better elucidated if the true topology of the resistance network is known. We thus highlight the need for future studies to measure and map the thermal interfacial resistances in the cellular medium. Despite a high thermal interfacial resistance, we computationally predict the temperature changes in organelles to be less than 10 mK under physiological conditions generating few nanowatts of heat. By systematically increasing the number of cells, we show that even a few nanowatts of heat per cell can produce 1-2 K temperature change in tissues, which is typical in cold-induced thermogenesis. Through this work, we provide insight into the length-scale dependence of thermal properties and temperature changes that are vital for studies related to biocalorimetry, nanowarming, and ablation therapy. We also explored different thermometry techniques to identify the suitability for a given biochemical pathway. Specifically, we identified that intracellular thermometry under stimulated conditions, and extracellular tissue-scale thermometry could provide valuable physiological insight. To advance the latter – tissue-scale thermometry – we develop a wireless temperature measurement technique in the next Chapter.

CHAPTER 5

MAGNETOSTRICTIVE SENSORS FOR WIRELESS TEMPERATURE SENSING

This chapter is adapted in part from *Rajagopal and Sinha, Design and analysis of magnetostrictive sensors for wireless temperature sensing, Review of Scientific Instruments, in review (2021)* [165].

In the previous chapter, we discussed how extracellular thermometry could be useful to observe physiologically relevant and endogenous thermogenesis, especially in tissue scales. Extracellular thermometry, has been proven useful in previous studies to map the thermoregulatory neuronal circuits [47], [48] and cancer metabolism [49]–[52], even using through sutured mm-scale thermometers. In this chapter, we advance extracellular thermometry by developing a wireless technique to avoid invasive suturing required for typical tissue-scale temperature sensing. We utilize magnetostrictive transducers that are commonly used as actuators, sonar transducers, and in long-range non-destructive evaluation. The temperature sensitivity of resonance frequency in magnetostrictive transducers has been reported in previous studies; however, the origin of the temperature sensitivity has not been fully explored. In this work, we identify the material properties that determine the temperature sensitivity, and we provide ways to improve the sensitivity and detection technique. Further, we demonstrate an alternate temperature sensing technique that does not use the resonance frequency measurement, which can reduce the instrument complexity. Overall, we provide modeling methods and a general framework to analyze magnetostrictive materials for temperature sensing at centimeter length-scales, which can be suitably adapted for tissue-scale temperature sensing.

5.1 Introduction

Magnetostrictive sensors have a wide array of applications ranging from fluid property measurements such as pressure [166], [167], velocity [166], [168],

viscosity [169], [170], humidity [166], [171], etc. to industrial applications such as positioning actuators [172], sonar transducers [173], torque sensors [174], etc. Typical fluid properties such as pressure, viscosity, etc. affect the loading and/or damping of a resonating magnetostrictive sensor, which changes its resonance frequency [175]. On the other hand, temperature changes affect the intrinsic material properties, especially the Young's modulus of the magnetostrictive material [175]. There has been a growing interest in understanding the temperature dependence of the Young's modulus in magnetostrictive materials [176]–[180]. Previous work [176] used a simplified constitutive model to propose that the temperature-dependent anisotropy field could be the cause for the temperature dependence of Young's modulus. However, the anisotropy field's temperature dependence has neither been quantified nor been used to demonstrate any improvement to the sensitivity. Recent studies [177]–[180] have provided more detailed non-linear constitutive models that utilize fundamental material properties to model the Young's modulus as a function of temperature and bias fields. Such studies [177]–[180] report on thermo-magneto-mechanical modeling of magnetostrictive materials, but they lack direct experimental validation. Therefore, it still remains unclear how to identify new materials or new detection techniques that could improve the sensitivity of magnetostrictive sensors to temperature changes.

In this work, we modify previously reported non-linear constitutive equations [177], and use them to both analytically and computationally model a magnetostriction-based temperature sensor. We perform a sensitivity analysis, and experimentally demonstrate a 5-fold improvement to the temperature coefficient of resonance frequency (TCF). Such a wireless temperature measurement can be integrated into existing magnetostriction based actuators or transducers, which are currently used in applications such as high-pressure pipelines [181], drilling rigs [182], food packaging [183], [184], anti-theft tags [185], etc. This chapter is organized as follows. In Section 5.2, we describe our experimental setup, which we use to measure the TCF of Metglas. In Section 5.3, we report the thermo-magneto-mechanical constitutive equations that can capture the Young's modulus variation with bias field and temperature. Using the constitutive equations, we perform a sensitivity analysis to identify the material properties that determine temperature sensitivity. In Section 5.4, we use finite element simulations and a lumped circuit model to study the influence of sensor dimensions on the overall measurement. In Section 5.5, we demonstrate an improvement to the TCF using Terfenol. We also discuss an alternative sensing technique that does not require measuring the

resonance frequency to measure temperature changes. Overall, our work provides ways to improve the sensitivity and explores alternate measurement techniques for temperature sensing through new or repurposed existing magnetostrictive sensors.

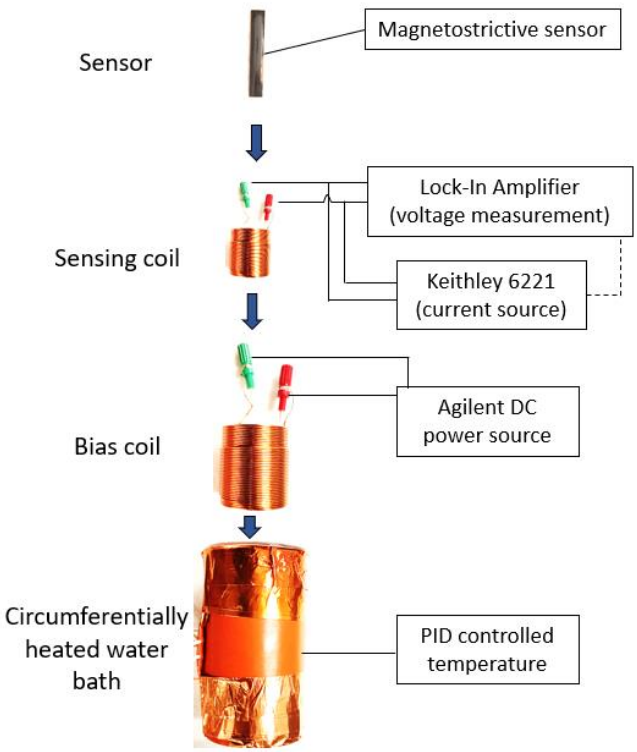

Figure 5.1: Schematic of the measurement setup used to measure the voltage response of magnetostrictive sensors at different bath temperatures.

5.2 Experimental setup

Figure 5.1 shows the schematic of the experimental setup to measure the magnetostrictive sensor response at different bath temperatures. We use Metglas 2605 TCA magnetostrictive strips (38 mm x 4 mm x 30 μm) taken from commercially available Sensormatic anti-theft tags. The Metglas strip is placed inside a sensing coil (ϕ17 mm x 25 mm) by vertically suspending the strip using a thread attached to the center. Keithley 6221 supplies the ac current to the sensing coil at a set frequency, whereas the Lock-in amplifier measures the ac voltage across the coil at the same frequency. In this configuration, the sensing coil is used to provide the actuation ac magnetic field, and also to measure the induced emf due to the sensor, simultaneously. The sensing coil is placed inside a bias coil (ϕ40 mm

x 70 mm), which provides the dc magnetic field. The coils and the sensor are placed inside a water beaker, which is attached with a flexible silicone heater to provide circumferential heating. The heater is controlled by a PID controller fitted with a thermocouple to control the temperature within the bath. Any temperature gradients axially across the heated water bath are typically less than 1 K at steady state. We use a fluxgate magnetometer (TI DRV425EVM) to measure the magnetic field.

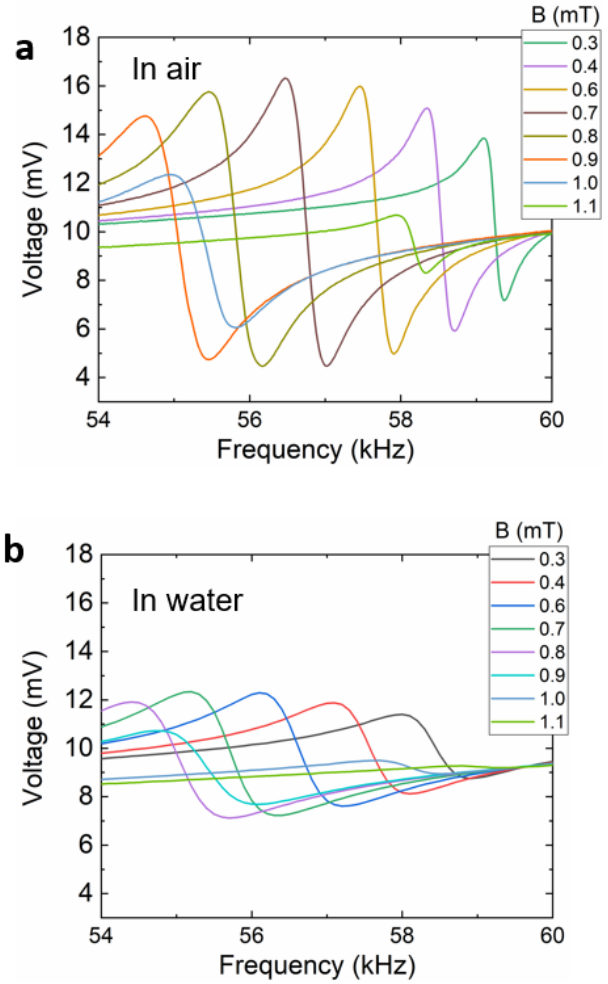

Figure 5.2: a) Voltage response of the ac coil housing the Metglas sensor in air at room temperature. b) Voltage response in water at room temperature. The resonance frequency and the voltage amplitude at resonance are a function of the dc magnetic field (bias). An ac sensing current of 100 μA was used for actuation.

Figure 5.2 shows a typical voltage response of the magnetostrictive sensor in air and water at room temperature (25°C). We discuss the characteristics of the voltage response curve in detail in Section 5.4. Briefly, the voltage response during a frequency sweep shows a peak, followed by a trough near the resonance

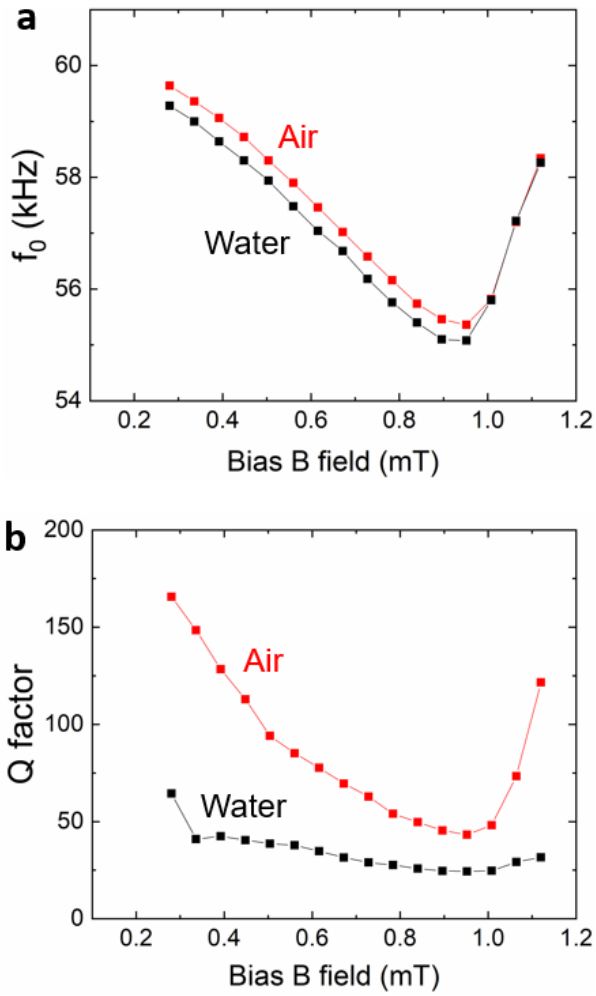

Figure 5.3 a) The resonance frequency of the magnetostrictive sensor at different dc bias fields at room temperature. b) Q-factor of the magnetostrictive sensor in air and water at different bias fields. Q-factor was calculated using the ratio of resonance frequency to the full-width half maximum of the resonance curve.

frequency. The resonance frequency and the voltage amplitude at resonance are a function of the dc magnetic field (bias) as shown in Figure 5.2 and Figure 5.3. The resonance frequency and Q factor decrease with the bias field for fields <0.18 A,

but they increase at higher bias magnetic fields (Figure 5.3). On the other hand, the voltage amplitude initially increases with the bias field but decreases at higher bias magnetic fields. When the entire setup is placed in a water bath as shown in Figure 5.1, the Q factor of the sensor reduces, especially at very low and very high bias field (Figure 5.3). We changed the temperature of the water bath to observe the resonance frequency shifts with temperature as shown in Figure 5.4. We denote the resonance frequency at T_0=30°C as f_0. The shift in resonance frequency (Δf) due to temperature change is bias-dependent. At low bias fields, the resonance frequency decreases with temperature, whereas at high bias fields it increases with temperature. At intermediate and very high bias fields, the resonance frequency does not change significantly with temperature. We note that to extract the resonance frequency, we used the trough in the voltage response (Figure 5.2) throughout this work for consistency, and the analysis does not change significantly if the peak is used instead. To characterize the temperature dependence of the resonance frequency, we define the temperature coefficient of resonance frequency (TCF) as $\Delta f/(\Delta T.f_o)$, where Δf is the change in resonance frequency from f_0 due to a change in temperature ΔT from T_0. From the data in Figure 5.4, we find that the maximum TCF for the Metglas strip we used is ~0.03 %K^{-1} at 30°C.

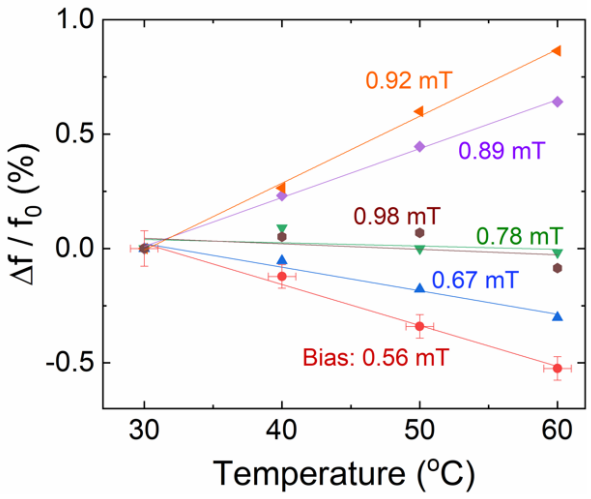

Figure 5.4: Shift in resonance frequency ($\Delta f/f_0$) in Metglas 2605 due to a temperature change in the water bath. f_0 corresponds to the resonance frequency at temperature T_0=30°C. The y-error bars correspond to 1σ fitting error in estimating the resonance frequency. The x-error bars correspond to the 1σ in temperatures measured in the heated water bath during measurement.

5.3 Thermo-magneto-mechanical model (static analysis)

In this section, we provide thermo-magneto-mechanical constitutive equations that can capture the experimentally observed variation in the resonance frequency of magnetostrictive sensors due to changes in bias fields and temperatures. The resonance frequency of our magnetostrictive sensor can be approximated to that of a free-standing slender beam, and is given by [186],

$$f_{res} = \frac{1}{2L}\sqrt{\frac{E}{\rho(1-\nu)}} \tag{4}$$

where, L is the length of the beam, ρ is the density, ν is the Poisson's ratio, and E is the Young's modulus. The Young's modulus of magnetostrictive materials are typically a function of the applied magnetic field (H), the film stress (σ), temperature, and the magnetostrictive strain (λ). The relationship between the induced strain (ϵ), magnetization (M), and the applied magnetic field (H) has been analytically modeled in 1D in previous work [177]. We use a modified version of this analytical model, which we describe in Appendix D. We show in the Appendix Figure D.1 that this analytical model can predict the experimentally measured magnetostrictive strain (λ) due to an applied magnetic field (H) for a variety of magnetostrictive materials such as Terfenol, Metglas 2605, 2801, etc. We extend this model as shown in Eqns. (5)-(6) to predict the Young's modulus of the magnetostrictive material under an applied dc magnetic field (H) and for small temperature changes ΔT from room temperature.

$$\begin{aligned}\frac{1}{E} &= \frac{1}{E_s\,(1+\gamma\Delta T)} + \left(1-\frac{M^2}{M_s^2}\right)\frac{\lambda_s}{\sigma_s}\operatorname{sech}^2\left(\frac{2\sigma}{\sigma_s}\right) \\ &+ \left(2-\tanh\left(\frac{2\sigma}{\sigma_s}\right)\right)\frac{\lambda_s M}{M_s^2}\frac{\partial M}{\partial \sigma}\end{aligned} \tag{5}$$

$$\frac{\partial M}{\partial \sigma} = 3\chi M\lambda_s\left(1-\beta\Delta T - \frac{1}{2}\tanh\left(\frac{2\sigma}{\sigma_s}\right)\right)\left(\frac{\mu_o M_s^2}{\left(\left(\frac{M_S^T}{3\chi H_{eff}}\right)^2 - \text{cosech}^2\left(\frac{3\chi H_{eff}}{M_S^T}\right)\right)} - 6\chi\sigma\lambda_s\left(1-\beta\Delta T - \frac{\sigma_s}{4\sigma}\ln\left(\cosh\left(\frac{2\sigma}{\sigma_s}\right)\right)\right)\right)^{-1} \quad (6)$$

where,

M is the magnetization of the magnetostrictive material,

M_S is the saturation magnetization at room temperature,

M_S^T is the saturation magnetization at a temperature T,

λ_S is the saturation magnetostrictive strain at room temperature,

H_{eff} is the effective applied magnetic field,

χ is the magnetic susceptibility of the magnetostrictive material,

σ is the compressive film stress,

σ_S is the stress at which magnetostrictive strain λ=λ_S [187],

ΔT is the change in temperature from a room temperature of 25°C,

β is the temperature coefficient of the magnetostrictive strain (λ), which is given by $\beta = -\frac{1}{\lambda}\frac{d\lambda}{dT}$,

γ is the temperature coefficient of the Young's modulus at magnetic saturation (E_S),

μ_0 is the vacuum permeability.

We implemented the static thermo-magneto-mechanical model for magnetostrictive materials through analytical and finite element simulations, separately. Analytically, we use the Appendix Eqns. (15)-(18) to estimate the induced magnetization (M) using the applied magnetic field (H). Since the effective applied magnetic field (H_{eff}) is also coupled to the magnetization (M), we iterate the Appendix Eqns. (15)-(18) to obtain the magnetization M for a given applied field H. We then use Eqns. (4)-(7) to predict the Young's modulus (E) and the resonance frequency (f_{res}) of the magnetostrictive sensor for different bias fields (H) and temperatures.

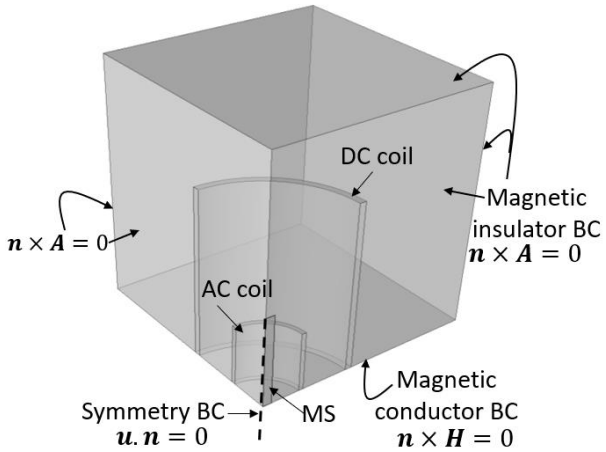

Figure 5.5: Computational domain of the finite element simulations. We model 1/8th of the system utilizing the symmetry. MS – magnetostrictive sensor. The dimensions and relative positions of the coils and sensor correspond to our experimental setup shown in Figure 5.1.

For finite element modeling, we use a computational domain shown in Figure 5.5. We model 1/8th of the system utilizing the symmetry in the computational domain. The boundary conditions are shown in Figure 5.5. A magnetic conductor ($\boldsymbol{n} \times \boldsymbol{H} = 0$, where $\boldsymbol{n}$ is the normal vector) boundary condition is applied to the bottom face of the domain, where the magnetic field is expected to be normal to the face. Magnetic insulator boundary condition ($\boldsymbol{n} \times \boldsymbol{A} = 0$) is applied to the remaining five faces of the domain where the magnetic field normal to the faces are expected to vanish. $\boldsymbol{A}$ is the magnetic vector potential. We applied symmetry boundary condition ($\boldsymbol{u}.\boldsymbol{n} = 0$, where $\boldsymbol{u}$ is the displacement vector) at the magnetostrictive sensor's two outer surfaces, which were cut to exploit the symmetry in the system. The dimensions of the coils and the sensor correspond to

the experimental setup we used, which is shown in Figure 5.1. We use COMSOL Multiphysics to solve Maxwell's equations and mechanical constitutive relations. We incorporated the Eqns. (5)-(6) and Appendix Eqns. (15)-(18) in the finite element model to capture the temperature and magnetic field dependence of Young's modulus (E) of the magnetostrictive sensor. We then used eigenfrequency analysis to extract the resonance frequency (f_{res}) of the magnetostrictive sensor.

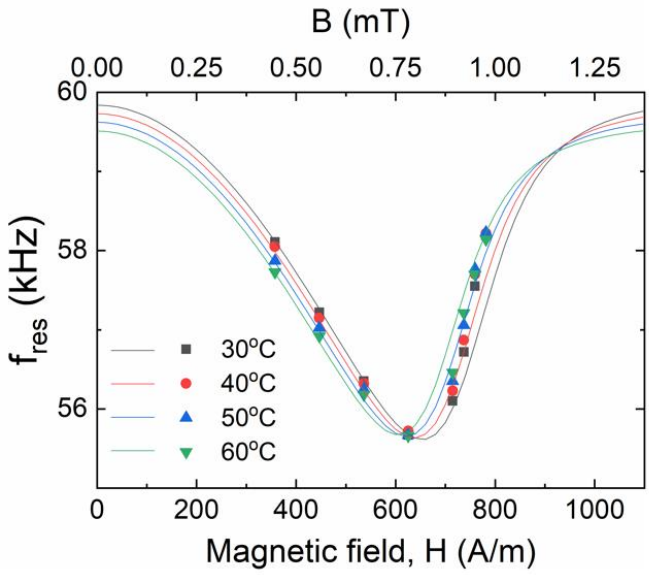

Figure 5.6: Resonance frequency of the Metglas 2605 strip at different temperatures and dc bias fields. The dots represent experimental data points. The solid lines are representative of the fitting from both the analytical model and finite element simulations separately. The fitting parameters are provided in Appendix D.

We plot the results of the thermo-magneto-mechanical models in Figure 5.6. The experimental data points are shown as dots. The lines in Figure 5.6 are representative of the results from both the analytical calculations and finite element simulations. The results from the finite element simulations do not differ from that of the analytical model. We fit our model to our experimental data using $\gamma, \beta, \chi, \sigma, \sigma_S, E_S, M_S, \lambda_S$ as fitting parameters, where the initial values for some of the material properties ($\gamma, \beta, \chi, E_S, M_S, \lambda_S$) were taken from literature [188]–[196]. We provide the fitting parameters in Appendix D. Small modifications within an order of magnitude to the literature values [188]–[196] resulted in a good fit for the experimental data as shown in Figure 5.6. At low bias magnetic fields, the resonance frequency is a strong function of the temperature. However, there is a

cross-over in the temperature dependence of the resonance frequency at a bias field of ~0.75 mT. At the cross-over point (~0.75 mT), the resonance frequency is essentially temperature independent, as also evident from Figure 5.4. Similarly, there is a second cross over at ~1.1 mT, where the resonance frequency is again temperature independent. We explain in the following Section 5.3.1. the significance and the reason behind these cross-over points. Overall, the thermo-magneto-mechanical model could qualitatively capture the experimentally observed resonance frequency variation with temperatures and bias fields.

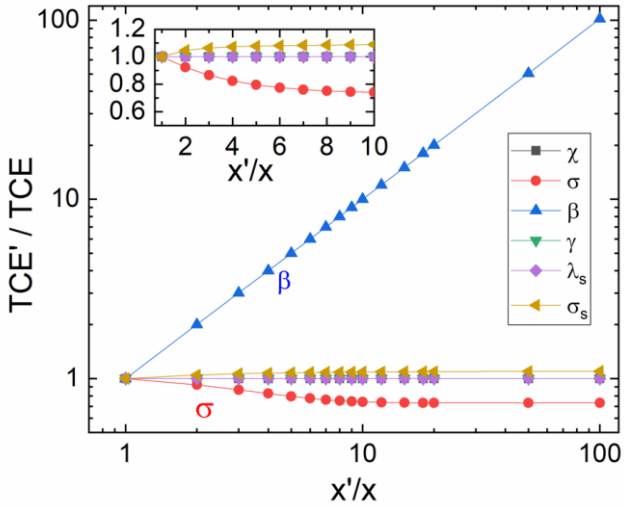

Figure 5.7: The change in temperature coefficient of Young's modulus (TCE) is plotted against the change in various material parameters at high magnetic fields (when $M \sim M_S/2$). x corresponds to one of the material and fitting parameters: $\chi, \sigma, \beta, \gamma, \lambda_s, \sigma_s$. Initial values for x were: χ=1, γ=10^{-4} K^{-1}, β= 10^{-4} K^{-1}, λ_s=10^{-6}, σ_s=10 MPa, σ=1 MPa. The inset shows the variation in TCE'/TCE for material parameters other than β.

5.3.1 Sensitivity to temperature

We use the thermo-magneto-mechanical model (Eqns. (5)-(6)) to find the material properties that influence the temperature coefficient of resonance frequency (TCF). The resonance frequency is a function of the length of the sensor (L) and the Young's modulus (E), both of which vary with the temperature. The thermal expansion coefficient (α), defined as $\alpha = \frac{1}{L}\frac{dL}{dT}$ is typically small, in the order of 10^{-6} K^{-1}, and hence does not contribute significantly to the change in the resonance frequency when $\Delta T \sim 10$ K. The temperature dependence of the Young's modulus

is therefore more dominant in causing a change in the resonance frequency. We define the temperature coefficient of Young's modulus as $TCE = \frac{1}{E}\frac{\partial E}{\partial T}$. The magnitude of the temperature coefficient of resonance frequency (TCF) is then directly proportional to TCE. As evident from Eqns. (5)-(6), E is a function of several material properties such as $\gamma, \beta, \chi, \sigma, M_S$, etc. in addition to the applied field (H) and temperature (T). To analyze the temperature dependence of E with respect to these material properties, we look at three regimes: (1) low applied magnetic field, when $M \to 0$, (2) high applied magnetic field, when $M \sim M_S/2$, and (3) at saturation magnetic fields, when $M \to M_s$.

At low magnetic fields, when $M \to 0$, the temperature coefficient of Young's modulus can be approximated as $TCE = \frac{1}{E}\frac{\partial E}{\partial T} = \gamma$ from Eqn. (5). Even though γ is the temperature coefficient of Young's modulus at magnetic saturation (E_S), γ directly influences the temperature coefficient of Young's modulus (TCE) and hence TCF even at low magnetic fields (when $M \to 0$).

At high magnetic fields, when $M \sim M_S/2$, the temperature coefficient of Young's modulus can be written as,

$$TCE = \left(\frac{1}{E}\frac{\partial E}{\partial T}\right)_{M \sim M_S/2} = -\frac{\partial\left(\frac{\partial M}{\partial \sigma}\right)}{\partial T}\frac{1}{\left(\frac{\partial M}{\partial \sigma}\right)^2}\left(\frac{\partial M}{\partial \sigma}\right)_{\Delta T=0} \tag{7}$$

For a change in a given material property from x (say) to x', we plot in Figure 5.7, the change in the corresponding temperature coefficient of Young's modulus from TCE to TCE', when the other material properties are kept constant. Here, x represents one of the material properties: $\chi, \sigma, \beta, \gamma, \lambda_S$. We find from Figure 5.7 that the temperature coefficient of magnetostriction, β, dominates the other properties in influencing the temperature coefficient of Young's modulus. The inset in Figure 5.7 shows that the compressive film stress σ could reduce the temperature coefficient of Young's modulus by up to ~20%. Other material properties or fitting parameters do not influence the temperature sensitivity significantly (<10%) at high magnetic fields. Therefore, at high magnetic fields (when $M \sim M_S/2$), the temperature coefficient of magnetostriction strain, β, directly influences the temperature coefficient of resonance frequency (TCF), whereas the film stress, σ, negatively influences the TCF.

At saturation magnetic fields (when $M \rightarrow M_S$), the temperature coefficient of Young's modulus is given by $TCE = \frac{1}{E}\frac{\partial E}{\partial T} = \gamma$ from Eqn. (5), which is similar to regime 1 (when $M \rightarrow 0$) for low applied magnetic fields. We discussed three different regimes, and they can be observed in Figure 5.6 from the two cross-over points because γ and β have opposite signs in Metglas (see Appendix D). The temperature coefficient of resonance frequency (TCF) for bias fields from 0 mT to ~0.75 mT is governed by γ; TCF for bias fields from ~0.75 mT to ~1.1 mT is governed primarily by β; and TCF for bias fields $\gg$ 1.1 mT is governed by γ. We discuss in Section 5.5 how we can use these material properties to identify magnetostrictive materials that could have higher TCF.

5.4 Lumped circuit model (dynamic analysis)

In the previous section, we performed a static thermo-magneto-mechanical analysis to predict the material property variation with bias fields and temperatures. In this section, we model the vibrating magnetostrictive sensor using a lumped circuit model that couples the magnetic and kinematic circuits. Consider a magnetostrictive rod of area A and length l wrapped with a current-carrying coil (Figure 5.8). An ac current of I is supplied to the coil and the output voltage V is measured. We consider the kinematic circuit to be a parallel RLC network. Spring constant is modeled as an equivalent resistance (R), mass of the rod is modelled as an equivalent inductor (M), and compliance (C^H) is modelled as an equivalent capacitance. Compliance at a constant magnetic field is defined as $C^H = s^H\, l/A$, where s^H is the elastic compliance defined as $s^H = \frac{\partial \epsilon}{\partial \sigma}$ at a constant field H. We perform our analysis using the mobility representation of magnetostriction [197], where θ: 1 acts as the turns ratio of an electromechanical transformer relating the mechanical force F to the electric current I, and the velocity v to the voltage in the circuit, V.

The measured output voltage V in the magnetic circuit can be written as,

$$V = IR_e + j\omega L^S I + \frac{ANd}{s^H l} v \tag{8}$$

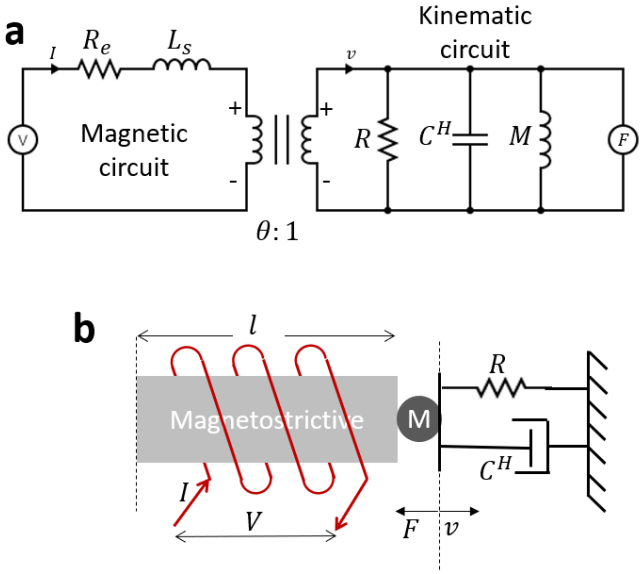

Figure 5.8: a) Equivalent circuit diagram of the electromechanical coupling between the ac coil and the magnetostrictive sensor. b) Schematic of the magnetostrictive material wrapped with a coil shown along with an equivalent free body diagram.

Where, R_e is the electrical resistance of the coil, L^S is the inductance of the coil, ω is the frequency of the ac current, N is the number of turns in the coil, v is the net velocity of the magnetostrictive rod's end surface, and d is the magnetostrictive constant defined as $d = \frac{\partial \epsilon}{\partial H}$ at a given stress. The net force in the magnetostrictive rod is given by,

$$F = \frac{-v}{\frac{1}{R} + j\omega C^H + \frac{1}{j\omega M}} + \frac{ANd}{s^H l} I \tag{9}$$

Since the magnetostrictive sensor is not constrained ($F = 0$), we can combine Eqns. (8) and (9), to get the measured output voltage V as,

$$V = IR_e + j\omega L^S I + \frac{\theta^2 R j\omega M I}{j\omega M + R(1 - \omega^2 C^H M)} \tag{10}$$

Where, $\theta = \frac{ANd}{s^H l}$ is the electromechanical coupling factor. We can also represent the output voltage as $V = V_{ns} + V_{ind}$, where V_{ns} is the voltage across the coil when there is no magnetostrictive strip inside (corresponding to the first two terms in Eqn. (10)), and V_{ind} is the induced voltage due to the vibrating magnetostrictive strip (corresponding to the last term in Eqn. (10)).

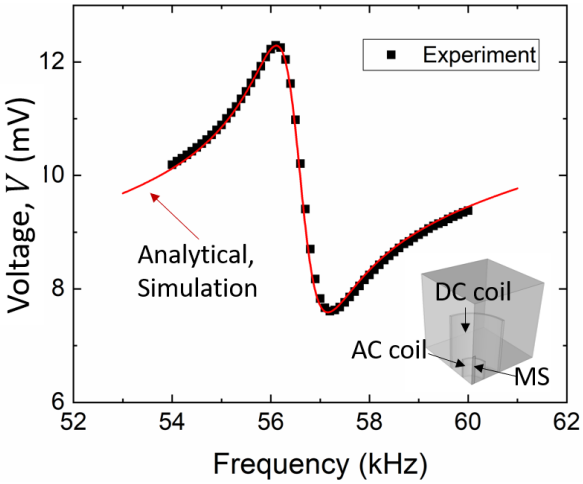

Figure 5.9: Voltage response of the ac coil housing the Metglas sensor in water at room temperature (25°C) at a dc bias field of 0.6 mT. Experimental data points are shown as black dots. The red solid line is representative of the results from both the analytical model and finite element simulations. The fitting parameters are provided in Appendix D.

We implemented the lumped circuit model analytically and using finite element simulations. First, we fit the analytical lumped circuit model (Eqn. (10)) to our experimental data as shown in Figure 5.9 using the terms in Eqn. (10) as fitting parameters. From Figure 5.9, we find that the analytical lumped circuit model could capture the voltage response of the magnetostrictive sensor during a frequency sweep. We then use the analytically estimated fit parameters R_e and L^S for the V_{ns} term in the finite element model. For the finite element model, we model the output voltage as $V = V_{ns} + \Theta V_{ind}$, where $V_{ns} = IR_e + j\omega L^S I$ uses the analytically estimated fit parameters R_e and L^S; induced voltage V_{ind} due to the magnetostrictive sensor is obtained from the Maxwell solver as $V = \oint E.dl$ across the coil, and Θ is the fitting parameter. We use a frequency domain solver to estimate the induced voltage for a range of frequencies. The Young's modulus of the material was estimated for the applied dc field using the static thermo-magneto-

mechanical model described in section 5.3. The red line in Figure 5.9 is representative of the fitting from both the analytical lumped circuit model and that of the finite element simulation. We provide details on the fitting parameters in Appendix D. Overall, both the lumped circuit model and the finite element simulations can capture the coupling between the magnetic and kinematic circuits.

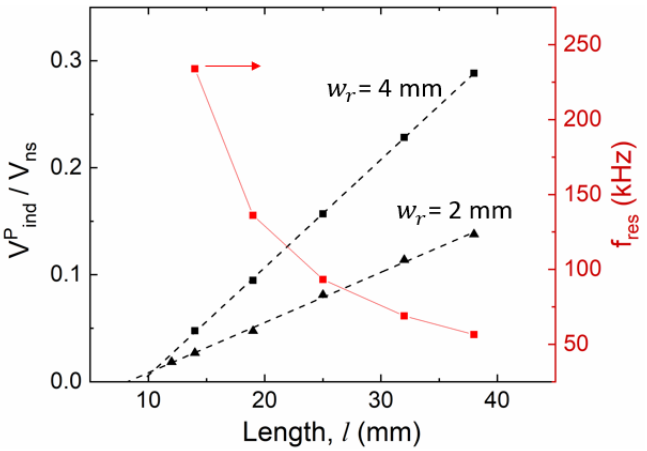

Figure 5.10: Signal-to-background ratio at the ac coil for different Metglas sensor dimensions are plotted along the left y-axis. The data points shown in dots are from simulations. The dashed lines are straight-line fits to the simulated data. The solid red line connects the corresponding data points. The coil dimensions correspond to that of the experimental setup shown in Figure 5.1

5.4.1 Length-scale dependence of induced voltage

In this section, we study the influence of the dimensions of the magnetostrictive sensor on the induced voltage in the coil. This could be useful in determining the minimum size of the sensor that can be used, and the number of sensors required. We use the validated finite element model that captured electromechanical coupling, shown in Figure 5.9. Using the same configuration of coils that we used in our experimental setup and the finite element simulations, we change the dimensions of the magnetostrictive sensor and observe the change in the peak induced voltage (denoted by V_{ind}^P) using simulations. We used the same Rayleigh damping coefficients for all the simulations. In Figure 5.10, we plot the ratio of V_{ind}^P over V_{ns}, which is representative of the signal-to-background ratio, for different lengths l and widths w_r of the sensor. The no-strip voltage, V_{ns}, is the baseline voltage that is present even without a magnetostrictive sensor. From Figure 5.10,

we find that the signal-to-background ratio (V_{ind}^{P}/V_{ns}) reaches zero when the length of the magnetostrictive sensor is ~10 mm. Similarly, the signal (V_{ind}^{P}) drops roughly by half when the width w_r of the sensor is reduced by half. Therefore, for the current configuration of measurement (Figure 5.1, Figure 5.5), we expect the signal-to-background ratio to vary linearly with the length and width of the sensor, especially when l:10-40 mm, w_r:2-4 mm.

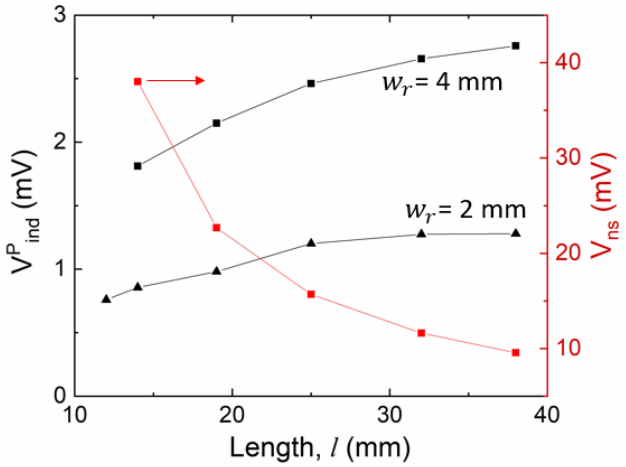

Figure 5.11: The peak induced voltage (V_{ind}^{P}) at the ac coil is plotted for different Metglas sensor dimensions on the left y-axis. The voltage at the ac coil with no magnetostrictive strip (V_{ns}) is shown on the right y-axis. The data points shown in dots are from simulations. The solid lines connect the shown data points. The coil dimensions correspond to that of the experimental setup described in Figure 5.1.

The signal-to-background ratio (V_{ind}^{P}/V_{ns}) drops to zero (in Figure 5.10) primarily because the background (V_{ns}) increases at high frequencies. The background signal is given by $V_{ns} = IR_e + j\omega L^S I$, where, $j\omega L^S$, the self-inductance component, is directly proportional to the frequency of operation, ω. When the sensor length l is reduced, the resonance frequency increases as shown in Figure 5.10, which in turn increases the background signal (V_{ns}, Figure 5.11), obscuring the signal-to-background ratio. The background signal (V_{ns}) increases 4-fold from 9.5 mV to 38 mV (Figure 5.11), when the sensor length is decreased from 38 mm to 14 mm. On the other hand, the peak induced voltage (V_{ind}^{P}) decreases ~2-fold from 2.8 mV to 1.8 mV. Therefore, when using a small sensor, the reduction in the signal-to-background (V_{ind}^{P}/V_{ns}) ratio is primarily due to the self-inductance of the ac coil at high frequencies.

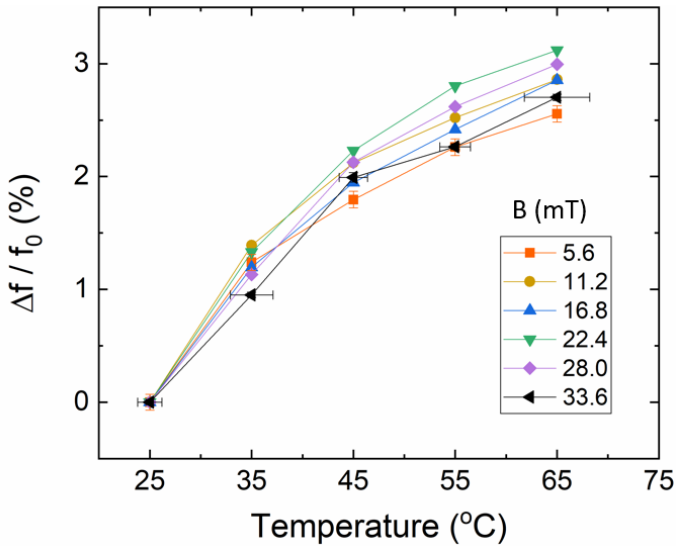

Figure 5.12: Shift in the resonance frequency ($\Delta f / f_0$) for a Terfenol rod (53 mm × 17 mm × 1.2 mm) due to a temperature change in the water bath. f_0 corresponds to the resonance frequency at temperature T_0=25°C.

5.5 Discussions

In this work, we first experimentally measured the shift in the resonance frequency of a magnetostrictive sensor due to temperature changes. We then analytically and computationally analyzed the material properties responsible for the shift in resonance frequency due to temperature changes. We also analyzed the influence of the sensor size on the overall measurement. In this section, we extend our analysis and provide ways to improve the sensitivity to temperature changes. We also discuss potential applications and limitations.

In Section 5.3.1, our sensitivity analysis revealed that the temperature coefficient of resonance frequency (TCF) is directly dependent on (1) γ – temperature coefficient of E_S, at low ($M \to 0$) and saturation ($M \to M_S$) bias magnetic fields, and (2) β – temperature coefficient of magnetostriction strain (λ), at high bias magnetic fields (when $M \sim M_S/2$). From the analytical fitting in Figure 5.6, we determined γ for the Metglas sensor to be 3.6×10^{-4} K^{-1}. Among other magnetostrictive materials, Terfenol was previously reported [179] to have a higher $\gamma \sim 4.2\times10^{-3}$ K^{-1}. We repeated our experiments using Terfenol (Figure 5.12) and found the temperature coefficient of resonance frequency (TCF) to be ~0.14% K^{-1}, which is almost 5-fold higher than that of the Metglas sensor (~0.03% K^{-1}) for a

ΔT~10 K. Even though the coefficient of magnetostriction (β) for Terfenol is comparable to that of Metglas, a higher γ potentially resulted in a higher TCF for Terfenol. Further, our thermo-magneto-mechanical model could capture the resonance frequency shifts in Terfenol as shown in Figure 5.13. We note that a previous work [176] on $Fe_{40}Ni_{40}B_{20}$ alloy reported a TCF~0.15% K^{-1}, which is comparable to the TCF we report for Terfenol. The TCF from $Fe_{40}Ni_{40}B_{20}$ is higher than the Metglas sensor we report, possibly because of a higher β, which is also evident from a wider spread in their resonance frequencies at higher magnetic fields [176]. Even though Terfenol has a higher TCF (~0.14% K^{-1}), the susceptibility χ~80 is much lower than that of Metglas (χ~50,000). Thus, Terfenol requires higher bias magnetic fields (~5-10 mT) than that required for Metglas (~0.2-0.6 mT). Future work can focus on identifying materials with a high susceptibility (χ) that also have high γ and/or β to have a higher temperature coefficient of resonance frequency (TCF) at low bias fields (<1 mT).

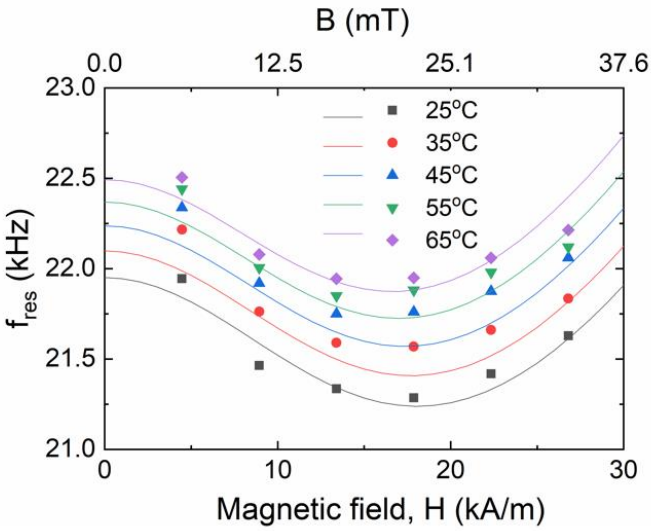

Figure 5.13. The resonance frequency of Terfenol rod at different temperatures and dc bias fields. The dots represent experimental data points. The solid lines are representative of the fitting from both the analytical model and finite element simulations separately.

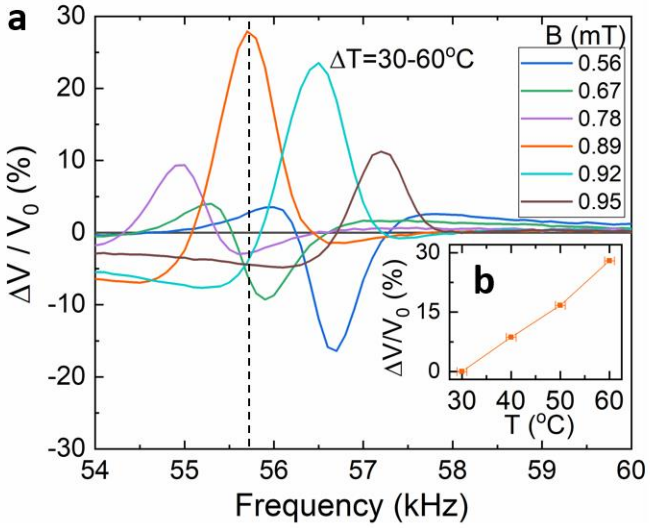

Figure 5.14: a) Shift in the voltage ($\Delta V/V_0$) at the ac coil due to a change in the temperature of the water bath plotted for different bias fields over a range of frequencies. ΔV corresponds to the change in the measured voltage due to a temperature change from 30°C to 60°C. V_0 is the measured voltage at 30°C. A Metglas sensor was used in a setup similar to Figure 5.1. b) Inset plots the voltage shifts for different temperatures at a frequency of 55.7 kHz and a bias field of 0.89 mT.

Throughout this work, we focused on the shift in resonance frequency as a potential sensing parameter to measure temperatures. However, an alternative temperature sensing technique can be developed by measuring the voltage across the ac coil at a fixed frequency near the resonance frequency of the magnetostrictive sensor. We explain it using a Metglas sensor in the same experimental setup (Figure 5.1). In Figure 5.14a, we plot the ratio $\Delta V/V_0$, where V_0 is the voltage measured at 30°C and ΔV corresponds to the difference in the measured ac voltage amplitude between 60°C and 30°C bath temperatures. The magnitude of $\Delta V/V_0$ reaches a maximum at 55.7 kHz, at a bias field of 0.89 mT. At this frequency (55.7 kHz) and bias field (0.89 mT), we plot the $\Delta V/V_0$ in the inset (Figure 5.14b). We find that the $\Delta V/V_0$ directly increases with temperature. If we define a temperature coefficient of the measured ac voltage as $TCV = \frac{\Delta V}{V_0}\frac{1}{\Delta T}$, the TCV is roughly 0.8% K^{-1}. The TCV can be maximized by choosing a frequency and a bias field where the magnitude of $\Delta V/V_0$ is the highest across the temperature range desired (Figure 5.14). Measuring the TCF can be time-consuming and require sophisticated equipment such as network analyzers, whereas TCV can be easily measured using

digital multimeters or lock-in amplifiers. The TCV can be used for temperature sensing only when the frequency shift (Δf) due to a temperature change (ΔT) is less than the width of the resonance curve. In other words, the Q-factor of the sensor must be smaller than $(TCF.\Delta T)^{-1}$. For the Metglas sensor, the Q-factor in water is ~30, whereas $(TCF.\Delta T)^{-1}$ is ~ 110 for a ΔT= 30°C, thus allowing us to use TCV for temperature sensing. Further, the TCV could be a function of the position and orientation of the sensor with respect to the ac sensing/transmit coil. Therefore, the temperature coefficient of the voltage (TCV) of the ac coil can be used for temperature sensing, especially in places where the relative position and orientation of the magnetostrictive sensor remains constant with respect to the coil.

A wireless temperature sensing technique using a magnetostrictive sensor could be useful in applications requiring remote temperature measurements such as in high-pressure pipelines [181], food packaging [183], [184], core body temperature measurements [198], etc. It could also be useful for potential concurrent temperature and fouling measurements in industrial pipelines [181], especially in low-temperature heat exchangers [149], [199], [200] to ensure profitable heat recovery. In this work, we used a concentric coil configuration to serve as proof-of-concept experiments. Helmholtz coils and/or permanent magnets can also be used instead. For instance, the bias coil can be replaced by a ferromagnet that is magnetized to provide the appropriate bias field. The magnetostrictive sensor strip can be packaged along with the ferromagnet in a manner similar to the commercially available anti-theft tags [201]. Further, the commercially available anti-theft tags can also be repurposed to measure temperatures either using the TCF- or TCV-based method. We discussed in Section 5.4.1. that the signal-to-background ratio (V_{ind}^{P}/V_{ns}) drops when the sensor dimensions are reduced. This can be overcome by two possible methods. First, two separate transmit and receive coils can be placed perpendicular to each other to decouple them and remove any self-inductance effects [196]. Second, multiple thin-film magnetostrictive sensors can be packaged together to increase the signal-to-background ratio [202]. Overall, magnetostrictive sensor packages can be suitably adapted to measure temperatures at remote locations, using either the TCF- or TCV- based technique.

Throughout this chapter, we discussed magnetostriction-based temperature sensing at remote locations for general purpose applications. For applications in biomedical sensing, magnetostriction-based sensors have previously been used in arterial stents for sludge detection [203], biliary stents for occlusion detection [196], orthopedic implants for stress detection [204], [205], etc. One of the notable

advantages of using magnetostriction-based sensors is that they are passive in nature and do not require active power sources such as batteries. This makes magnetostriction-based sensors an ideal implantable device for long-term usage. As discussed in this chapter, any existing magnetostriction-based sensor for any biomedical application [196], [203], [206], [207] can be potentially repurposed to measure temperatures using the TCF- or TCV- based techniques. Such existing magnetostrictive-based sensors for biomedical applications are typically 1 mm to 1 cm in length-scales [196], [203], [206]–[208]. Given the typical dimensions (mm-cm), magnetostriction-based sensors are not injectable-type sensors, but they are potentially implantable. Implantable type sensors can provide data only from locations where they are placed, whereas, injectable type sensors could potentially diffuse anywhere and provide data from multiple spatial locations. In the next chapter, we discuss how magnetostriction-based sensing technique (which are implantable) can be extended in future work through magnetic nanoparticles or MRI-based temperature sensing (which use injectable contrast agents).

5.6 Conclusion

In summary, we modeled and analyzed magnetostrictive materials for use in potential wireless temperature sensing systems. We first experimentally measured the temperature coefficient of resonance frequency (TCF) in a Metglas 2605 TCA strip to be ~0.03%K^{-1}. We then implemented thermo-magneto-mechanical constitutive equations using both analytical and finite element methods to model the magnetostriction-based sensing system. The analytical and computational models developed in this work provide a general framework for the sensitivity analysis of magnetostriction-based temperature sensing, and they can be suitably adapted to any configuration of the sensing scheme. Through our sensitivity analysis, we identified the material properties of interest and demonstrated a 5-fold improvement to the TCF by using Terfenol. We also explored an alternate temperature sensing scheme that reduces instrument complexity by using the temperature coefficient of ac voltage (TCV) at the coil, which could be used if the sensor and coil locations are fixed relative to each other. Overall, we provide ways to use new or repurposed existing magnetostrictive sensor packages to enable temperature measurements at remote locations. In the next chapter, we discuss how the magnetostriction-based temperature sensing forms the basis for developing future thermometry using MRI-based techniques that has the potential to provide tissue-scale spatiotemporal temperature maps.

CHAPTER 6

CONCLUSION AND FUTURE WORK

This dissertation broadly explored thermogenesis in biological systems, ranging from intracellular to tissue length-scales. We developed two thermometry techniques: 1) using a micro-thermocouple probe to invasively measure intracellular temperatures and 2) using magnetostrictive sensors for remotely measuring temperatures at tissue length-scales. We provided experimental and theoretical investigation of cellular-level temperatures changes and understood how to choose the right thermometry technique. In this chapter, we first summarize the main results of this dissertation, and then we discuss potential avenues for future explorations.

6.1 Summary

First, we developed an intracellular thermometry technique using a semiconductor-based fabrication technique. We used a 5 μm wide silicon nitride platform to support a micro-thermocouple probe with a thermocouple junction diameter of 1 μm. Since the suspended nitride platform is ~400 μm in length from the silicon substrate, the thermocouple junction is thermally isolated from the substrate temperature changes. By devising a solid-state calibration technique using micro-fabricated heater and thermistor lines, we achieved a calibration accuracy of ~1% for the micro-thermocouple probe. Numerically, we estimated the thermal time constant of the probe to be ~32 μs. Since the thermocouple leads were covered with silicon nitride, the probe is rendered chemically and electrically inert to a typical cellular environment. Such characteristics enabled the micro-fabricated thermocouple probe to be used for transient intracellular thermometry.

Using the micro-thermocouple probe, we experimentally investigated stimulated mitochondrial thermogenesis in *Aplysia* neurons. Non-shivering thermogenesis is stimulated at the mitochondria to increase the temperatures in homeotherms when exposed to cold climatic conditions. The metabolic pathway responsible for the temperature increase has widely been considered to be steady-state substrate oxidation. In this work, we analyzed a less explored mechanism –

mitochondrial proton motive force dissipation – that can potentially release transient heat during mitochondrial thermogenesis. We exogenously stimulated the mitochondria in *Aplysia* neurons using a chemical proton uncoupler BAM15. During proton uncoupling, which occurs endogenously in other cell lines, the protons are shuttled across the mitochondrial inner membrane. This proton current typically lasts for about < 1 s. By measuring the transient intracellular temperature changes during a stimulated proton uncoupling, we measured temperature changes of about ~4.7 K that lasted over 1 s, corresponding well to the expected proton current duration. Our measurements thus show the utility of intracellular thermometry in elucidating the thermochemistry of mitochondrial metabolism.

We then theoretically explored the expected temperature changes at cellular and tissue length-scales. To model the heat transfer in cellular medium, we highlighted the need to critically examine the role of thermal interfacial resistances of biomolecular complexes in the cytosol. We provided a general framework for the thermal resistance network modeling that can capture the temperature changes in both intracellular and tissue length-scales. Using this model, we predicted that the intracellular temperature changes in organelles are less than 10 mK under endogenous conditions in an isolated cell. The sub-mK intracellular temperature changes increase with the length-scale, reaching up to 1 K at ~ 1 cm long tissues. Based on these results, we concluded that the following combination of thermometry and biochemical pathways could provide useful insights:

1) Intracellular thermometry could be useful to monitor transient temperature changes over < 1 s, especially when stimulated exogenously to produce higher temperatures that may not otherwise occur endogenously.

2) Extracellular thermometry could be useful to monitor endogenously thermogenic reactions over length-scales > 1 mm, such as tissues or organs.

Since we previously performed intracellular thermometry on transient mitochondrial proton uncoupling, the rest of the work focused on the latter – extracellular thermometry.

We developed a magnetostriction-based temperature sensing technique that can remotely measure temperature changes at tissue length-scales. Traditionally, magnetostrictive materials have been used for a variety of fluid property measurements (such as pressure, viscosity, density, etc.) using the changes in the resonance frequency of the sensor. Through systematic theoretical and

computational analysis, we identified the material properties that influence the temperature coefficient of resonance frequency (TCF). Accordingly, we demonstrated a 5-fold improvement to the TCF by choosing a better material. We also identified a different mode of operation, where the temperature coefficient of ac coil voltage (TCV) can be calibrated against temperatures. Magnetostrictive sensors have been used in applications ranging from high-pressure pipelines to anti-theft tags to biomedical instrumentation. By repurposing or repackaging existing magnetostrictive sensors, we can enable temperature measurement at remote locations through the TCF- or TCV-based techniques.

6.2 Future work

We attempted to measure the temperature changes during an action potential as described in Appendix B. We explained the challenges we faced and highlighted potential ways to overcome them (in Appendix B). Such an experiment could help to identify the contribution of individual ions (Na^+, K^+, Ca^{2+}) and the ion pump (Na^+/K^+-ATPase) in the overall energy exchange during an action potential. The contribution of individual ions can be determined through exogenous blocking agents. For instance, cobalt chloride [209] could block the Ca^{2+} channels, and tetrodotoxin [209] could block the Na^+ component. Similarly, ouabain [210] could be used to block the ion pump Na^+/K^+-ATPase. The use of such toxins could increase the complexity and PPE requirements for the experiments. On the other hand, changing the concentration of the ions in the buffer solution [209], [211], [212] is a simpler way to identify the contribution of individual ions to the total energy change. For instance, in a Na^+-free (or Na^+ reduced) buffer solution, the action potential energy changes would include all ions except Na^+.

Temperature changes across synaptic clefts have been hypothesized to assist synaptic transmission [12], [27], [213], [214]. Specifically, in the hypothalamus neurons of mice, Ghrelin activates the uncoupling protein (UCP2) [213], which is found to be in abundant quantity near the synaptic clefts of hypothalamus neurons [27]. Similarly, previous studies have reported that the synaptic delay – the latency between pre- and post-synaptic membrane currents – decreases at high temperatures [215]. Together, these reports warrant an investigation of the thermochemistry of synaptic transmission. This can be experimentally established indirectly by measuring the excitatory postsynaptic potentials between two neurons under circumstances such as high/low ATP

concentration, exogenous BAM15 supply to stimulate local heat production, and high/low bath temperatures.

The metabolic pathway of tumor progression can be probed using intracellular thermometry through intermittent mitochondrial stimulation. For instance, MCF10A are normal breast epithelial cell lines. When they undergo HRAs oncogenic transformation to MCF10-AT, the flux through the pentose pathway and TCA cycle is increased [216]. After metastasis (MCF10-CA), the flux through glycolysis and pentose pathway is further increased [216], producing more lactate and proline. Such changes in the metabolic pathway during the tumor progression can be observed through intracellular thermometry by the use of exogenous mitochondrial proton uncoupling. Similarly, thermometry can be used to probe the mechanical regulation of glycolysis in cancer-associated fibroblasts. Such fibroblasts release activin A in a substrate stiffness-dependent manner [217]. Intermediate-stiffness substrates typically result in higher levels of activin A, which in turn leads to epithelial to mesenchymal transition (EMT), which is the hallmark of metastasis. On a similar note, a recent study [218] reported that the mechanics of cellular microenvironment can modulate glycolysis during tumor progression. Consequently, we can expect intracellular thermometry using stimulated proton uncoupling to identify the mechanical regulation of metabolic pathways during tumor progression.

Recently, there have been several reports of noninvasive intracellular thermometry [4], [21]–[23], [74], [135], [219]–[223]. However, some of the upconverting nanoparticles have also been known to have apparent self-heating effects [63]. One of the notable noninvasive thermometry studies utilized nanodiamond based sensors, using which the study reported the intracellular thermal conductivity [135]. The measured intracellular thermal conductivity ranges from 0.07 to 0.13 $Wm^{-1}K^{-1}$ [135], which is less than that of typical proteins. This warrants an investigation of the intracellular thermal interfacial resistances from the various intracellular biomolecular complexes, as we discussed in Chapter 4. On the other hand, extracellular tissue-scale temperature mapping can be advanced by extending the magnetostriction-based techniques that we discussed in Chapter 5. We observed that the signal amplitude drops with the length-scale of the sensor. To overcome the signal reduction, the number of sensors can be increased [202]. Extending this further, we find that the magnetostriction based technique has similarities with nuclear magnetic resonance imaging (MRI). In MRI, the nucleus of the hydrogen atom acts as the sensor, which is present in large enough quantities in a given voxel to overcome the signal-to-noise ratio. Future work can extend the

magnetostriction-based temperature measurement technique to small length-scales through magnetic nanoparticle based thermometry [224]–[226] or through lab-scale MRI [227] based temperature measurement [228] using contrast agents [229] that can be injected into tissues for a spatiotemporal temperature map.

APPENDIX A

FABRICATION RECIPE FOR THE MICRO-THERMOCOUPLE PROBE

Preparing the wafer

1. Use 300 μm thick silicon wafer, which is double side polished and p-doped. Resistivity must be 10-20 Ω.cm. KOH etch rate highly depends on this doping concentration.
2. RCA SC-1 clean for 10 min. Keep the temperature of the hotplate to about 100 deg C. It should result in a bath temperature of 75 deg C
3. Oxygen plasma descum at 1 kW for 4 min.
4. Deposit PECVD nitride approximately 1 μm thick. Typical deposition rate is 12.1 nm/min, when the recipe "SINHA_MF" is used.
    a. Use dummy silicon samples, preferably big to stop the wafer from sliding inside the PECVD chamber.
5. Then, cut the wafer into individual pieces. Diced samples should be 9 cm X 2.5 cm.

Photolithographically patterning electrodes, and heater lines

6. Use the mask shown schematically in Figure A.1 for the electrodes and heaters.
7. Start with gold electrode patterning. Photolithography recipe follows
    a. Acetone, methanol, IPA, DI, IPA, N2 blow dry.
    b. Dehydration bake: 140 deg C for 1 min.
    c. Oxygen plasma 1 kW, 4 mins.
    d. For spin-coating PR, use the 2" wafer chuck.
        i. Recipe for spin-coating: HMDS, PR: 3000 rpm 5s, 6000 rpm 50 s. Followed by 100 deg C soft-bake for 1 min.

e. Clean mask with a tissue soaked in IPA.

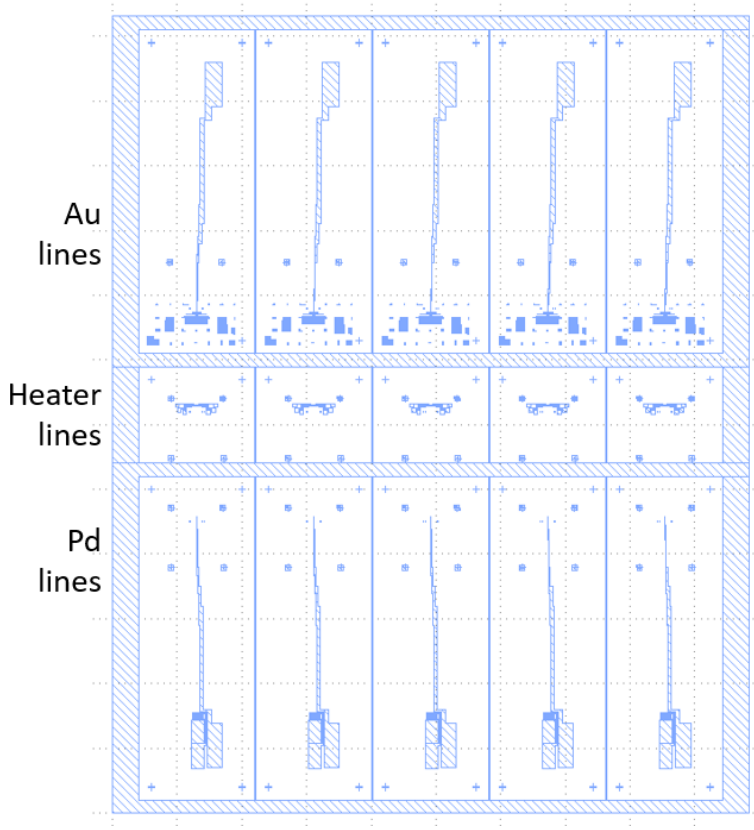

Figure A.1 Mask design for the electrodes and heater lines.

f. While setting up the mask aligner, blow-dry the samples to prevent the sample from sticking to the mask.

g. This is the first photolithography pattern. Align the mask to roughly match the crystallographic orientation of the sample.

h. 13 seconds of exposure in MJB3 to reach 120 mJ/cm2.

i. Develop for 24 seconds in AZ 400K 5:1.

    i. Wash with DI

    ii. Develop again for 4 seconds

    iii. Wash with DI

j. Oxygen plasma descum for 45 seconds at 500 W.

k. Load the sample onto the E-beam metal deposition carrier wafer. Place Kapton tape on unnecessary borders. There should be no metal deposition in the unwanted borders of the sample.

8. E-beam evaporation – metal deposition recipe:
    a. Deposit 7 nm Cr/ 70 nm Au.
    b. To remove the sample from the carrier wafer, place it inside an acetone bath, and soak it overnight.
    c. Then, sonicate it in acetone for 2-3 s.
9. Thorough clean: acetone, methanol, IPA, DI, IPA, oxygen plasma 1 kW 4 mins.
10. Photolithography recipe for patterning Palladium:
    a. Repeat the spin-coating recipe. During mask alignment, ensure that the mask is aligned well to the previously deposited alignment markers.
    b. Check for alignment and adjust it using 5x, 10x, 20x objectives one-by-one.
11. E-beam metal evaporation of Palladium. Same recipe as above. Use 7 nm Cr/ 70 nm Pd
12. Photolithography pattering of the heater and thermometer lines:
    a. Clean the sample: Acetone, Methanol, IPA, DI, IPA, oxygen plasma 1kW 4 mins.
    b. Align the mask using previously deposited patterns. Use the alignment marks on the farthest ends of the sample to get the best alignment throughout.
    c. 13 seconds exposure in MJB3 at 9mW/cm2 giving about 120mJ/cm2
    d. Just under 20 seconds of development. At 5:1 DI:400K.
    e. Clean with DI repeatedly.
    f. Oxygen plasma. 250 W 30 s.

g. Check under a microscope to confirm the alignment. Map the image onto the KLayout drawing to ensure that the patterns are in the right location.

13. E-beam metal evaporation for heater and thermometer lines.
    a. Cover the regions where metal should not be deposited, using microscope glass slides.
    b. Recipe: 10 nm of Cr and 300 nm of Au
    c. Lift-off will be difficult since the heater lines are very close to each other. Use AZ 400T at 130 deg C for 1 min.
14. Dice the samples into individual pieces (2.5 cm x 1 cm).

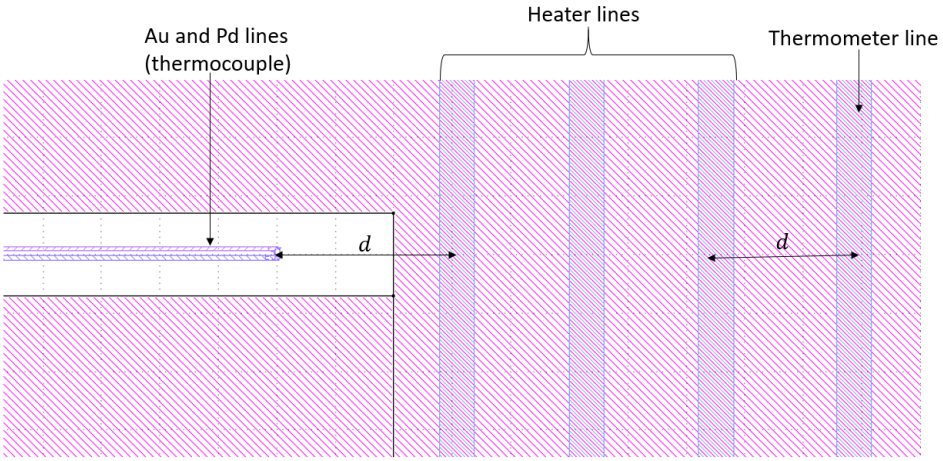

Figure A.2 E-beam lithography layout must ensure that the distance d between the thermocouple junction and the heater is the same as the distance d between the heater and thermometer lines. Every sample image must be mapped to a KLayout drawing and the Au/Pd line must be drawn accordingly.

E-beam lithography to pattern the thermocouple junction

15. Spin coat PMMA 950A4:
    a. 500 rpm 5s, 2200 rpm 70s. Bake at 180 deg C for 10 mins
16. Map the optical image onto the KLayout file to draw the thermocouple junctions as shown in Figure A.2.

17. E-beam lithography (Raith) recipe; first for gold electrode:
    a. Scratch at the corner close to the clip.
    b. 20 kV, 30-micron aperture, 100-micron write-field.
    c. Start with the faraday cup, measure current, it should be around 0.30 nA.
    d. Go to a clip position, find an alignment marker diamond to focus on.
    e. Focus and correct stigma up to 100 nm or less scale bar.
    f. Align UVW axes to the GDS file.
        i. Choose markers separated > 2mm
    g. Start a position-list, move, expose 63, layer 2, layer 21. Dose – 1, 1.3, 1.1 respectively.
18. PMMA development:
    a. Developer: MIBK: DI at 5:1.
    b. Development time: 1 min 50 s.
    c. Rinse with IPA.
19. Metal deposition step – same as above
20. Liftoff:
    a. Acetone + sonication not more than 5 mins.
    b. Use remover PG, heat at 110 deg C in hotplate.
    c. Sonicate it after heating.
21. Clean using acetone, methanol, IPA, DI, IPA, oxygen plasma 4 mins at 1 kW.
22. Repeat it for the palladium electrode.
23. Verify the connection using a multimeter. The probe should be roughly 1 kΩ.

Calibrating the thermocouple on-chip

24. Wire bond the sample for calibration and load it into the cryostat
25. Calibration details:

a. The resistance of heater ~ 50 Ω. The resistance of thermometer ~30 Ω.

b. Use a 10 kΩ HPR to send 10 μA of ac current to the 4pp line. Use the ground of sine out from lock-in by splitting it.

c. First, calibrate the TCR of the resistor.

d. Then, ramp the heating current from 0 to 35 mA, multiple times.

26. Repeat calibration for each sample.

27. Remove the ball bonds by using the wire bond capillary. Gently scratch it out. This is to ensure that the sample remains flat.

28. Deposit 200-400 nm of PECVD nitride for protecting the electrodes.

    a. Use photolithography and Freon RIE to remove the nitride from contact pads of the thermocouple.

Suspending the micro-thermocouple probe

29. Photolithography to pattern the probe profile.

    a. Use the same spin coating recipe.

    b. Use a mask aligner to align the probe profile with the sample electrodes.

    c. Development: under-develop it. Do it for 24 seconds.

    d. Then manually remove the undeveloped PR to ensure PR is removed from unwanted regions.

    e. Wash with DI multiple times.

    f. Hard bake at 120 deg C for 2 mins.

30. Freon RIE:

    a. 70% flow, 35mTorr CF4 only. Do gas evacuation

    b. Process time of 17.8 mins to remove the nitride from everywhere except the probe.

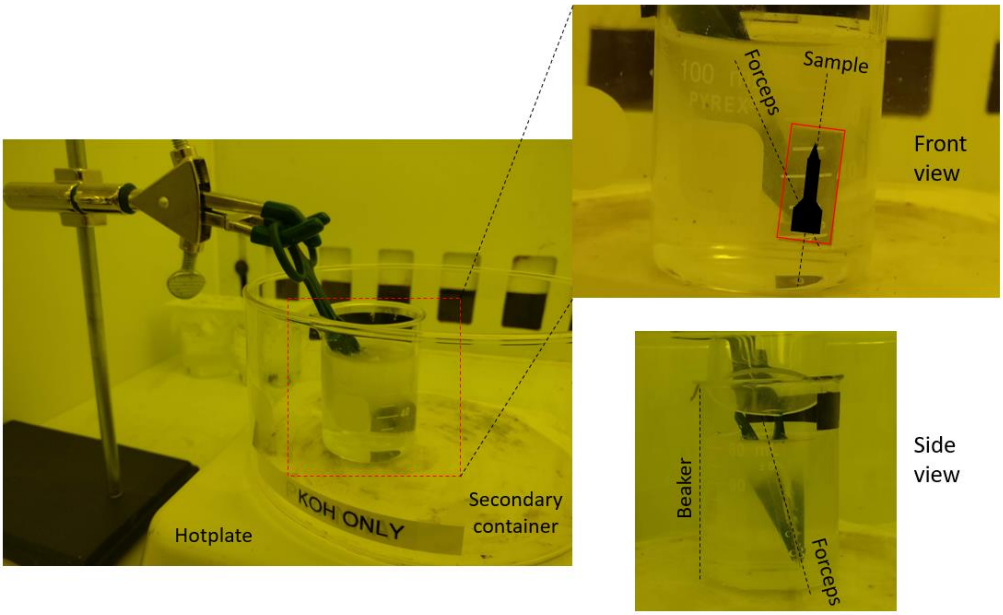

Figure A.3. Optical photograph of the setup used for KOH bulk-Si etching during probe suspension. The relative angles between the forceps, sample, and beaker were optimized to ensure that the products of the KOH etching, especially hydrogen bubbles, escape out without damaging the probe tip.

31. KOH etching recipe:

    a. Use a Pyrex beaker, fill 60 ml of DI water, add 49.09 g of KOH pellets. Roughly 45% KOH.

    b. The total solution will be ~ 82 ml.

    c. Use a secondary container to catch any spills.

    d. Keep the hot plate to about 220 deg C.

    e. Using forceps lock down the bottom portion of the probe making an angle of 20 -30 deg between the probe and forceps axis. A photograph of the setup is shown in Figure A.3.

    f. Place the support stand to hold the forceps that has the sample.

    g. The probe should be inclined sufficient enough to let the bubbles near the forceps go away from the sample. Make an angle of 5-10 degree from vertical, to assist the breaking Si substrate to curve away from the cantilever,

h. For these conditions, the KOH bath temperature could be around 80 deg C.

i. At about 30 mins, the solution level will be a little less than 80 ml.

j. Use a transfer pipette to add DI to increase the solution level to above 80 ml.

k. It takes about 45 mins to completely etch away the substrate which is around 300 microns thick.

l. Add 2 more fillers of DI water. Increase the temp to 225 deg C momentarily and decrease again.

m. Remove the forceps from the KOH bath the moment all the Si is etched away, and the probe is completely suspended. This happens at around 45-50 min of KOH etching.

n. Gently transfer the probe into a pre-prepared package. The package is explained in detail below.

Packaging the micro-thermocouple probe

32. Package details (Figure A.4):

    a. Use a 3D printed mount that can be easily fixed into any micro-manipulator stage.

    b. Affix two dummy silicon chips at the tip.

    c. Use a gold deposited dummy silicon as a contact pad for soldering external wires directly onto it.

    d. Place the fabricated probe onto adjacent dummy silicon.

    e. Wire bond the probe's contact pad onto the gold deposited dummy silicon, which is also soldered to the external connections.

33. Wire bonding:

    a. Use the micromanipulator to hold the probe and its 3D printed mount.

    b. Increase the force, time, power for the second contact.

    c. Use a dummy probe to check and adjust the height of the stage

d. Before wire bonding, stick an insulation tape across the probe and contact pad edges to avoid contact with silicon edges, which are conductive in nature.

e. Once the probe contact pads are connected, verify the connection using a Lock-in amplifier with 150 nA of current. The resistance of the probe should be roughly 1 kΩ.

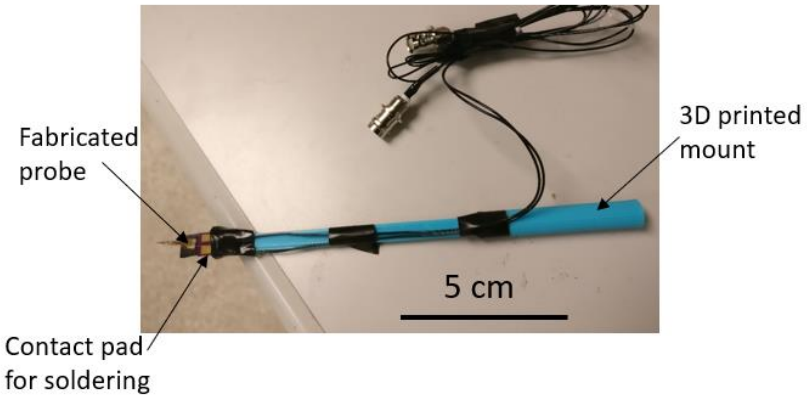

Figure A.4. Photograph of a packaged micro-thermocouple on its mount.

APPENDIX B

TEMPERATURE MEASUREMENT OF ACTION POTENTIALS IN *APLYSIA* NEURONS

The presence of small temperature gradients over large distances within the brain is essential for its functional activities. For instance, a recent MRSI scan of the brain temperature map [26] shows a maximum temperature difference of around 3 K between the frontal and parietal lobes. Moreover, small temperature gradients at the axon terminals have been understood to influence pre- and post-synaptic events [12]. Any external disturbances can lead to coupled changes in temperature, ion concentrations, and the resulting action potentials. Subsequently, the motivation for the proposed work is to measure and understand the coupling between temperature and the action potential generation in a single neuron. This requires simultaneous measurement of temperature and electrical activity of a single neuron. Since the expected temperature rise during an action potential is in the order of ∼1 mK, we statistically average the temperature data over > 10,000 action potentials to overcome the room temperature fluctuations.

B. 1. Experiment details

We used neurons from the abdominal ganglion of *Aplysia californica*. The ganglion was first proteased to assist in de-sheathing. The abdominal ganglion was then placed in a culture dish filled with room-temperature saline (composition, in mM: 420 NaCl, 10 KCl, 25 $MgCl_2$, 25 $MgSO_4$, 10 $CaCl_2$, 10 HEPES buffer, pH = 7.5) and secured using insect pins. After microdissection and de-sheathing, the cells were accessible to the electrodes. The ventral aspect of the ganglion was carefully dissected to provide access to the neurons of interest. Intracellular voltage recordings were made using borosilicate microelectrodes filled with 3 M KCl and pulled to a resistance of 11–16 MΩ. Intracellular microelectrodes were connected to an intracellular amplifier (Model 1600, A-M Systems, Sequim, WA), which were in turn connected to a data acquisition system (PowerLab 8/30, ADInstruments, Dunedin, New Zealand). To measure intracellular temperature changes, we first penetrated the target neuron with a voltage electrode. We then placed the thermal

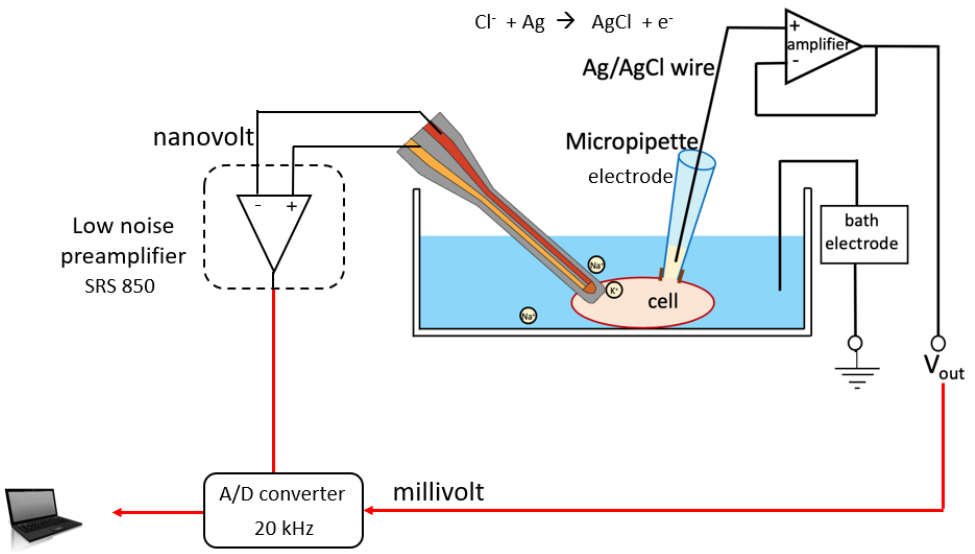

Figure B.1 Schematic of the experimental setup used for measuring the temperature changes during action potential generation.

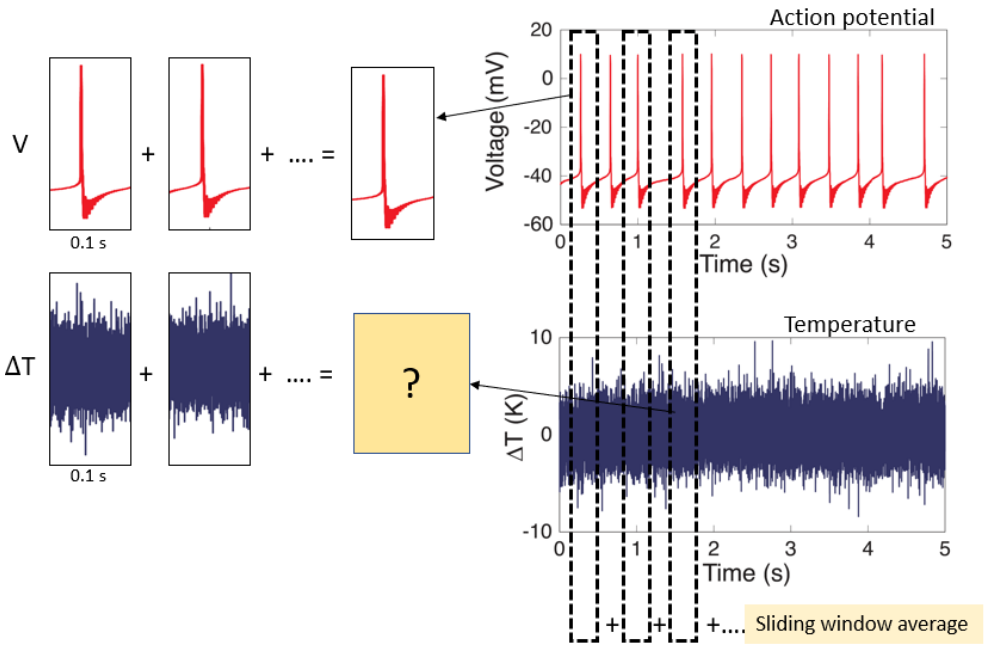

Figure B.2 Representative action potential and temperature measurement from a neuron. The temperature data corresponds to the Seebeck voltage from the micro-thermocouple (Seebeck coefficient = 1.18 μV/K).

probe on the surface of the same neuron. We used a low noise preamplifier (SR 850), whose output was connected to the same data acquisition system (PowerLab 8/30, ADInstruments). We show the schematic of the measurement setup in Figure B.1. Real-time voltage and temperature recordings were digitized and recorded in LabChart 7.3 (ADInstruments) at a sampling rate of 20 kHz.

B. 2. Results and discussion

The micro-thermocouple's Seebeck voltage (open circuit voltage) across the metal lines is calibrated against temperature changes. Given that the calibration constant (the Seebeck coefficient) is ~1.18 μV/K, we expect voltage changes in the order of nano-volts if the temperature oscillations are in the milli-Kelvin range. At high bandwidths, the open-circuit voltage measurement is subject to Johnson-Nyquist noise, given by $v_n = \sqrt{4k_B TR\Delta f}$, where T is the temperature, R is the resistance of the probe, and Δf is the bandwidth. For our measurements, v_n is on the order of ~1 μV. Therefore, the temperature measurement at 20 kHz is typically dominated by Johnson-Nyquist noise as also evident from Figure B.2.

Temperature signal can be extracted mathematically using bandpass filters or lock-in techniques if the frequency of the action potentials is known and periodic. However, the neurons in our experiments are either naturally firing or the spiking activity is induced by a constant depolarizing current. We do not use extracellular (nerve) stimulation to avoid high voltages (~1 V) in close proximity to the thermal probe. The depolarizing current generates a train of action potentials that are aperiodic as shown in Figure B.2. To extract the temperature signal during one action potential, we used a data-driven approach using the corresponding time-synchronized electrical data as shown schematically in Figure B.2. We used a sliding window to average temperature data.

We performed simultaneous measurement of temperature and voltage of action potentials over 4 hours from a neuron, resulting in data from 20,000 spikes. The voltage and temperature readings are individually averaged. Statistically, this is expected to change the power of noise by 1/N, where N is the number of action potential windows that were averaged. However, this statistical signal extraction process is dependent on the noise floor in the temperature signal. Given that we do not know the expected signal magnitude, we cannot directly determine the signal-to-noise ratio. We instead perform a simulation in MATLAB to estimate the improvement we can expect for a given noise floor. We begin with a known signal

($\vec{s}$, say 5 Hz) that is added to a random noise ($\vec{n}$) from both white and pink (1/f) sources. The new resultant signal, $\vec{r}$, simulates our raw temperature data. We then average this resultant signal N times. We define a parameter $P_N/P_{N=0}$, as the ratio of the power of the signal $\vec{r}$ after the Nth average, to its initial power (N=0). Results from simulated data are shown in Figure B.3a, and data from neurons are shown in Figure B.3b. From Figure B.3b, we see that the signal-to-noise ratio in our experiments can be greater than 3 if we average > 10,000 action potentials. Further, by comparing the noise from simulated data, we see that the noise in our experiments is roughly 36 dB.

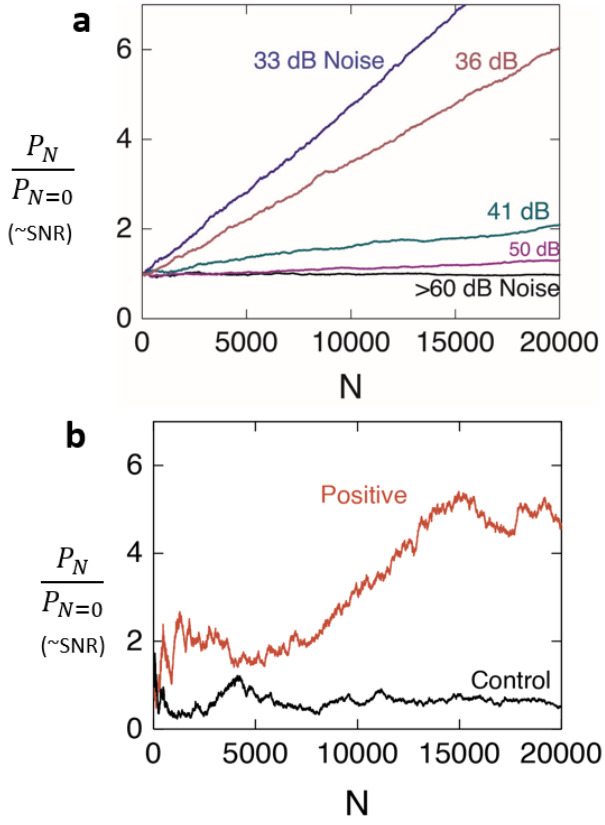

Figure B.3 a) Simulated statistical averaging to improve the signal. b) Statistical averaging improves the experimental temperature data from neurons. N represents the number of action potentials that were averaged.

In Figure B.4, we show the results of averaging the temperatures from N action potentials of a neuron. The left-panel in Figure B.4 corresponds to the temperature taken at the surface of a neuron, and the right-panel corresponds to a

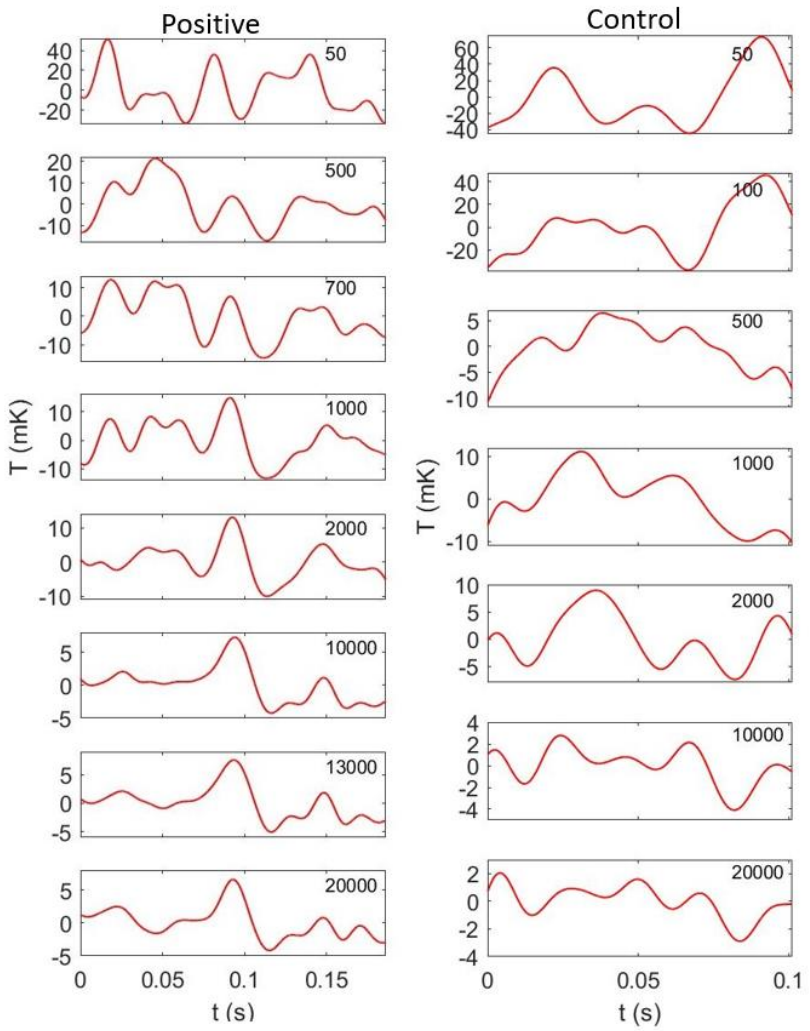

Figure B.4. The left-panel shows a series of averaged temperature data during an action potential. The number on the right corner represents the number of action potentials N that were used to generate the plot. The right-panel shows temperature data from a separate control experiment, during which the temperature probe was placed farther away (> 1 cm) from the actively firing neuron.

separate control experiment where the temperature probe was placed farther away from the firing neuron. The window of averaging was chosen based on the action potential data (not shown). The number on the top-right corner of each figure shows the number of action potentials averaged to obtain the corresponding plot. We see that the temperature fluctuations (for the positive data) are about 40 mK from 50 averaged action potentials. However, the magnitude of temperature fluctuations

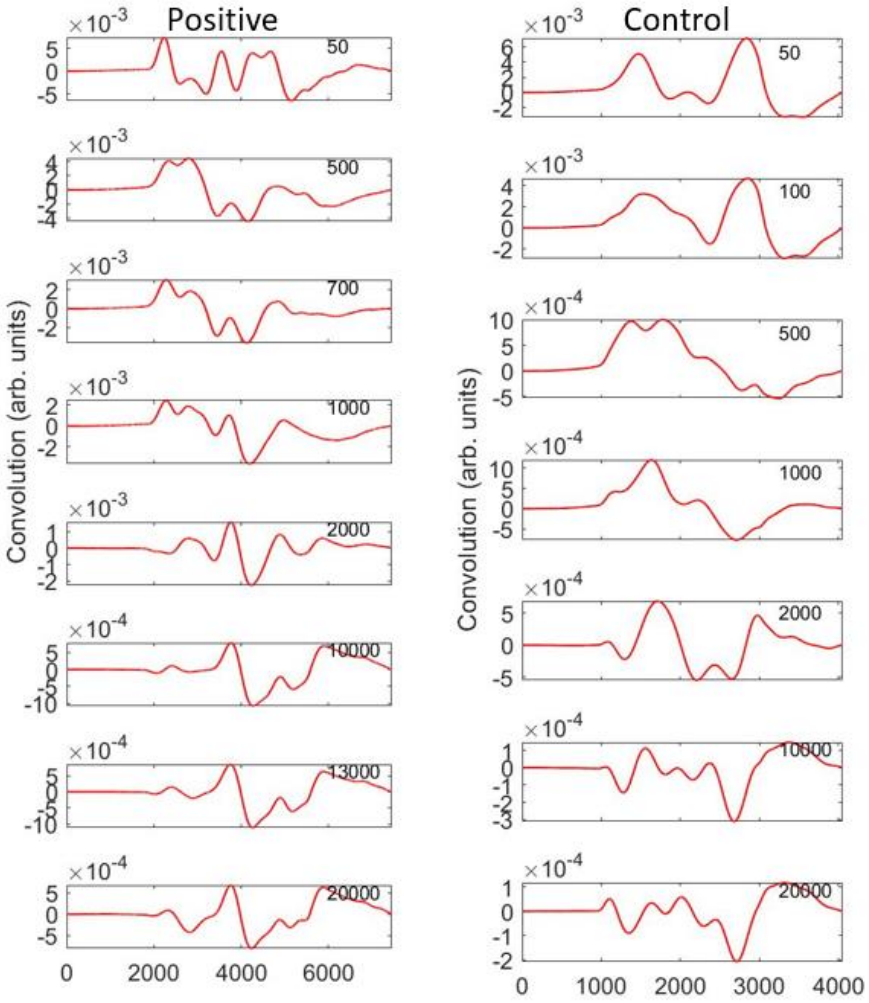

Figure B.5. The left-panel shows a series of averaged signal convolution data during an action potential. The number on the right corner represents the number of action potentials N that were used to generate the plot. The right-panel shows convolution data from a separate control experiment, during which the temperature probe was placed farther away (> 1 cm) from the actively firing neuron. For these plots, we performed signal convolution between the action potential voltage data and the corresponding temperature data. The units for x- and y-axis are arbitrary.

reduces as we average a greater number of action potentials. The magnitude of ΔT starts to saturate beyond 10,000 to about $\sim \pm 5$ mK, especially near the center of the window of time-averaging, which corresponds to the peak in the action potential. On the other hand, the control data starts with about 60 mK fluctuations at N=50, and reduces to around 3 mK, in an incoherent manner, in the sense that

there is no similarity in the temperature fluctuations from N=1,000 to 20,000 averages. To further analyze the data, we use signal convolution between the action potential voltage (say, f) and the corresponding temperature (say, T). The signal convolution between f and T is defined as: $\int_{-\infty}^{\infty} f(t-\tau)T(\tau)d\tau$. Signal convolution will help to identify features of the impulse response (f) on the signal (T). The higher the magnitude of the signal convolution, the higher is the effect of f on T. We performed signal convolution between the action potential voltage and the corresponding temperature data. The results of signal convolution are shown in Figure B.5. For the positive data, we find that the magnitude of signal convolution is around 5×10^{-4} near the mid-point of the time window, whereas the control data has a maximum convolution magnitude of ~3×10^{-4}. Even though both the temperature data and the signal convolution suggest that the temperature changes during an action potential are slightly higher than that of control, the overall data is not statistically significant enough. We were able to obtain a similar result only for a total of n=2 biologically independent neurons, out of n=12 neurons.

Our data may have been obscured by some of the following issues. We briefly discuss the issues and some ways to overcome them for future experiments. The room temperature fluctuations and vibrations need to be minimized. To this end, we typically performed all the experiments in the night. However, it may be helpful to perform the experiments in an air-floated experimental bench, in a basement. Further, we're able to get a maximum of 20,000 action potentials over 4 hours from a neuron before it depolarized permanently. If we could sustain a neuron to elicit >20,000 action potentials over a short period (~6 hours), it will help to better overcome the noise in the data. Last but not least, the hum noise (60 Hz), which is a dominant noise source in our data, can be electrically suppressed in real-time by using a humbug noise eliminator.

APPENDIX C

CELLULAR- AND TISSUE-SCALE HEAT TRANSFER SIMULATIONS

Throughout this work, especially in Chapter 4, we use finite element analysis using COMSOL Multiphysics. Here, we first validate the finite element analysis for a generalized scenario involving transient heat release from a cell placed in an infinite medium. We then use the validated model to fit our previously published experimental results to obtain the fitting parameters R_s'' and Q.

C. 1. Validation

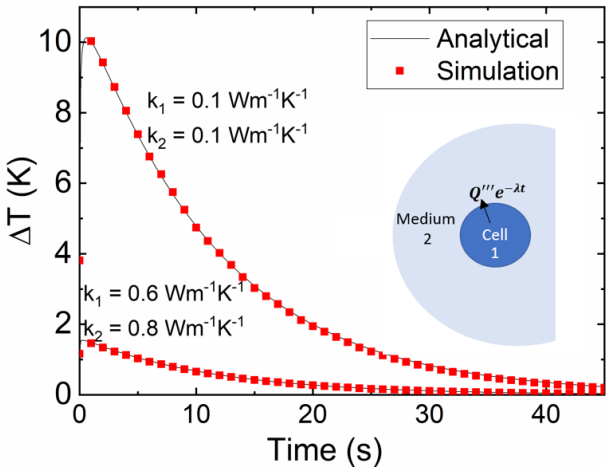

Figure C.1. Validating the finite element model for a generalized transient heat. The transient temperature change (ΔT) at the center of the cell is plotted. The temperature changes for two different combinations of cell (k_1) and medium (k_2) thermal conductivity are shown. The inset schematically depicts the domain of analysis, which is a cell of radius a, dissipating heat in an infinite medium.

Consider a transient heat $Q'''e^{-\lambda t}$ (W/m^3) diffusing from a cell (represented by 1) of radius a, in an infinite medium (represented by 2), shown schematically in Figure

C.1. The heat diffusion equation in spherical coordinates at a radius $r < a$ is given by:

$$\frac{1}{r^2}\frac{\partial}{\partial r}\left(r^2 k_1 \frac{\partial T}{\partial r}\right) + \ Q'''e^{-\lambda t} = \rho_1 C_1 \frac{\partial T}{\partial t} \tag{11}$$

where, T is the temperature, ρ_1 is the cell's density, C_1 is the cell-specific heat capacity, t is the time and r is the distance from the center of the cell. At a radius $r > a$, the heat diffusion equation is:

$$\frac{1}{r^2}\frac{\partial}{\partial r}\left(r^2 k_2 \frac{\partial T}{\partial r}\right) = \rho_2 C_2 \frac{\partial T}{\partial t} \tag{12}$$

where, ρ_2 is the medium's density, C_2 is the specific heat capacity of the surrounding medium. The temperature boundary condition at a radius $r = a$, is given by,

$$k_1 \left|\frac{\partial T}{\partial r}\right|_{r=a^-} = k_2 \left|\frac{\partial T}{\partial r}\right|_{r=a^+} \tag{13}$$

We use the Laplace transformation technique described in a similar previous work [230] to solve equations (11)-(13) to obtain the temperature distribution inside the cell ($r < a$) as:

$$\begin{aligned} &T(r,t) \\ &= \frac{a^2 Q'''}{k_1}\left\{\left(\frac{1}{3}\frac{k_1}{k_2} + \frac{1}{6}\right.\right. \\ &\left.\left. - \frac{r^2}{6a^2}\right)e^{-\lambda t} - \frac{2ab}{r\pi}\int_0^\infty \frac{e^{-\frac{y^2 t}{\gamma_1}}}{(y^2 - \lambda\gamma_1)}\frac{(\sin y \ - y\cos y)\sin\frac{ry}{a}\, dy}{[\,(c\sin y \ - y\cos y)^2 + b^2 y^2 \sin^2 y]}\right\} \end{aligned} \tag{14}$$

Where, a is the radius of the cell, $b = \frac{k_2}{k_1}\sqrt{\frac{\alpha_1}{\alpha_2}}$, α is the thermal diffusivity, $c = 1 - k_2/k_1$. We compare the results of the analytical model with that of a 3D finite element model in Figure C.1. The specific heat capacity for the cell and medium were taken to be 2900 J.kg^{-1}K^{-1} and 4100 J.kg^{-1}K^{-1}, respectively [114], [231]. The

density of the cell and medium were 1000 kg.m^{-3} and 1010 kg.m^{-3}, respectively. We considered a cell of radius 30 μm dissipating 300 $e^{-t/10}$ μW of heat. For different combinations of k_1 and k_2, we show in Figure C.1Figure that the finite element model matches the analytically predicted temperature change at the center of the cell. This validated finite element model is representative of all the simulations reported in this work. We also performed mesh convergence tests to identify the required mesh density such that all the results shown in this work are independent of the mesh.

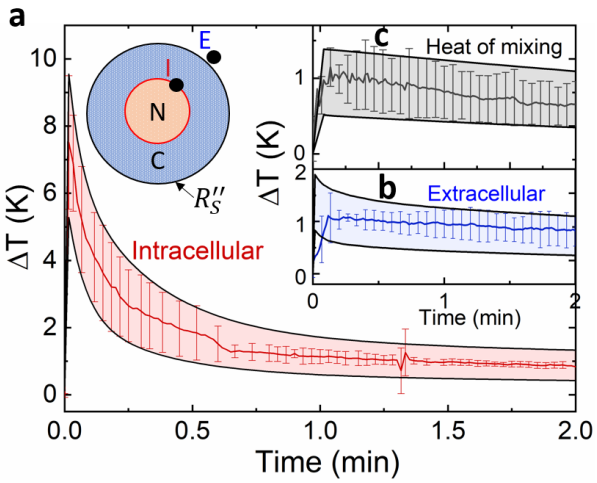

Figure C.2. Transient temperature change during BAM15 stimulated proton uncoupling is fit using finite element analysis to extract Q and R_s''. a) Intracellular data is representative of the temperature measured at the point *I*, as shown in the schematic. b) Extracellular temperature is representative of the temperature measured at the point *E*. c) Heat of mixing is the temperature change in the absence of cells due to the mixing of BAM15 and saline. Experimental data [*Rajagopal et al., Comms. Bio. 2019*] are shown with s.d. as error bars; only a few error bars are shown for clarity. The curves bounding the shaded regions are the upper and lower bound predictions from the computational model. N- nucleus, C- cytosol, I-intracellular, E-extracellular.

C. 2. Obtaining fitting parameters from our previous experiments

We use the validated finite element model to analyze our previously published experimental data [20]. Specifically, we use finite element models to fit three experimental temperature measurements: (1) heat of mixing (2) extracellular, and (3) intracellular. First, we use the temperature rise due to the heat of mixing BAM15 with saline to estimate the volumetric heat (Q'''_{HOM}) that is released everywhere during the process. To this end, we use a 1 mm x 1 mm x 1 mm domain with no cells, but with 4 adiabatic boundaries and 2 isothermal ($T = T_{ambient}$= 25°C) boundaries to match the measured ΔT and obtain a range of Q'''_{HOM}. The temperature fit is shown as black shaded region in Figure C.2c. Next, we use the obtained range of Q'''_{HOM} in the following models (Figure C.3) as a uniform volumetric heat source throughout the domain, since they are always present whenever BAM15 is used to stimulate the mitochondrial heat production.

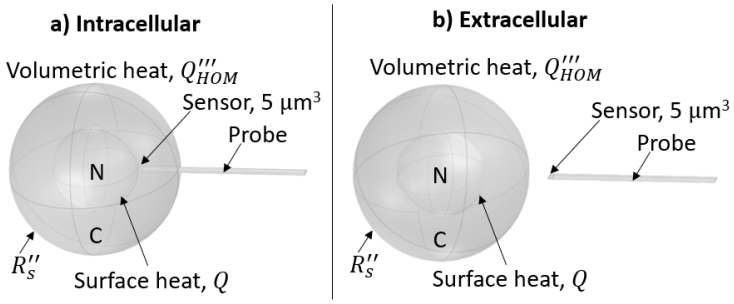

Figure C.3. The computational domains that were used to model the experiments. a) For intracellular analysis, the temperature probe is placed near the nucleus (N), where the temperature change is the highest. The mitochondrial heat production is modeled as a surface heat (Q) around the nucleus. b) For extracellular analysis, the probe is placed roughly 15 µm away from the cell. The measured temperatures are assumed to be an averaged temperature from a 5 µm^3 volume at the tip of the probe. We only model a 5×1×100 µm^3 volume of the micro-thermocouple probe since the probe is predominantly made of a thermally insulating suspended silicon nitride cantilever. The cells are placed in saline, which is not shown in the schematic. N-nucleus, C-cytosol.

The computational domains are schematically represented in Figure C.3. Below, we first list the assumptions involved in this computation model. We later discuss the validity and influence of these assumptions. We assumed the cells to be of ~100 μm diameter, representative of the *Aplysia* cells we used in the previous work. The nucleus (N) was assumed to be ~50 μm in diameter, roughly consistent with the proportion for a ~100 μm cell based on previous reports [108]. We also assumed that the mitochondria, the primary heat source in our experiments, to be uniformly distributed along the surface of the nucleus (N) [108]. We therefore use a surface heat flux boundary to introduce a heat Q at the surface of the nucleus, representing the heat release from proton-uncoupled mitochondria stimulated by BAM15. Our experimental measurements are representative of an averaged temperature measured at the probe's tip over a volume of 5×1×1 μm^3, which houses the thermocouple junction of ~1 μm diameter in a tip of width 5 μm and thickness ~1 μm [46]. The cells are assumed to be in a medium of 1 mm x 1 mm x 1 mm (not shown in Figure C.3) with 4 adiabatic boundaries and 2 isothermal ($T = T_{ambient}$= 25°C) boundaries. We fixed the thermal conductivity of the cell to be 0.58 Wm^{-1}K^{-1}. The boundary of the cell is assumed to have an equivalent surface resistance R_s''.

We iteratively fit the extracellular (point: E) and intracellular (point: I) temperatures simultaneously to obtain the fitting parameters: surface heat Q and resistance R_s'', for the data in Figure C.2. Since we use two temperatures measured at two spatially separated locations, our fitting could provide a unique solution for Q and R_s''. We used the following thermal properties. Probe: k_{probe}=0.8 Wm^{-1}K^{-1}, C_{probe}=370 J.kg^{-1}K^{-1}, ρ_{probe}=3100 kg.m^{-3}; cell: k_{cell}=0.58 Wm^{-1}K^{-1}, C_{cell}=2900 J.kg^{-1}K^{-1}, ρ_{cell}=1000 kg.m^{-3}; saline: k_{saline} = 0.6 Wm^{-1}K^{-1}, C_{saline}= 4100 J.kg^{-1}K^{-1}, ρ_{saline}=1010 kg.m^{-3} [114], [231]. The fitted temperatures are shown in Figure C.2 using the shaded regions. For each experimentally measured temperature, we computational fit both the upper and the lower limit of the measured temperatures. Thus, we obtain a range for the fitted surface heat Q, with a lower limit of $140\,e^{\left(-\frac{t}{4}\right)} + 75e^{\left(-\frac{t}{19}\right)}$ μW and an upper limit of $160\,e^{\left(-\frac{t}{3}\right)} + 200e^{\left(-\frac{t}{19}\right)}$ μW. For these of range of Q, we assumed a fixed R_s'', which from fitting was 7×10^{-4} K.m^{2}W^{-1} for a length-scale L~ 100 μm. A conservative upper limit for R_s'' can be estimated from the fact that a weak cell produced an intracellular ΔT~2.31 K [20] which can be assumed to be from a uniform volumetric heat Q_{HOM}''' but with a mitochondrial heat Q ~ 0. This provides an upper limit for R_s'' as 1.4×10^{-3} K.m^{2}W^{-1} at a length-scale L~ 100 μm. It is a conservative upper limit since the surface heat Q may not be zero even for a weak cell, in which case the extracted R_s'' can be lower than

1.4×10^{-3} K.m^{2}W^{-1}. The *Aplysia* cells used in our previous work were typically 100 μm; however, typical BAT cells that were the focus of the Chapter 4 are about ~50 μm. Since the resistance R_s'' (defined in Chapter 4) scales with the length-scales, the extracted equivalent surface resistance R_s'' at a length-scale of ~50 μm is 3×10^{-4} K.m^{2}W^{-1} - 7×10^{-4} K.m^{2}W^{-1}.

We fit our experimentally measured intracellular and extracellular temperatures separately to extract a lower and upper limit, respectively, for the effective thermal conductivity, k_{eff}, of the cell. We use the heat release Q estimated above (using k_{med} and R_s'') to extract a range of possible equivalent effective thermal conductivity. As discussed in Chapter 4, a single thermal property (k_{eff}) cannot capture both the surface maximum (≈extracellular) temperature and volume maximum (≈intracellular) temperature of a cell. Therefore, we separately fit the extracellular and intracellular temperatures using the same heat Q, to extract a range of the possible effective thermal conductivity for the cell, k_{eff}= 0.05 – 0.07 Wm^{-1}K^{-1}. The fact that a single k_{eff} cannot capture the intracellular and extracellular temperature changes simultaneously further supports the assumption of using a combination of k_{med} and surface resistance R_s'', suggesting that the local interfacial resistances cannot be ignored.

We now discuss the influence and validity of other assumptions used in this computational model. The size of the cell and the nucleus influences the extracted heat Q, but its effect on the equivalent resistance R_s'' is negligible, since it scales with the length-scale. We assumed that the mitochondria are uniformly distributed around the nucleus based on previous reports. However, if the mitochondria were concentrated at locations closer to the probe, then the true R_s'' could have been lower than that extracted from our model. We assumed that the equivalent resistance R_s'' is independent of temperature. However, it is known that the lipid layer undergoes a phase change at room temperature [152], [153]. Phase changes at cellular and organelle membranes could have increased the estimated resistance R_s'' by absorbing some of the heat without a corresponding temperature change. Given these assumptions, the extracted resistance R_s'' may be representative of the cellular resistance in experiments within an order of magnitude and possibly represents an upper bound. Similarly, the extracted effective thermal conductivity k_{eff} is representative of a lower bound. Further, our experiments were performed on *Aplysia* neurons, which were modeled as spheres in the computational domain; however, throughout Chapter 4, we focused on BAT cells with a cuboidal resistance network. Therefore, the R_s'' and k_{eff} extracted from our previous experiments with

Aplysia serve to provide an order of magnitude comparison to the results presented in this work, especially in Chapter 4.

C. 3. Length-scale dependent thermal properties

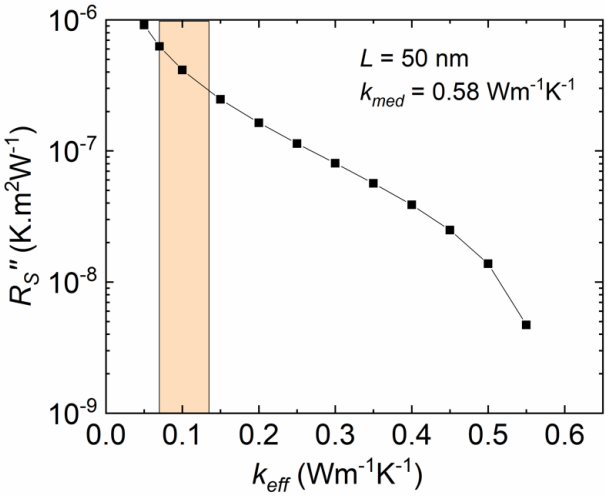

Figure C.4. The equivalent resistance R_s'' that is responsible for reducing the effective thermal conductivity k_{eff} is plotted for different k_{eff}. The R_s'' shown here corresponds to a length-scale L=50 nm and k_{med}=0.58 Wm^{-1}K^{-1}. The shaded region corresponds to a k_{eff}: 0.07 – 0.13 Wm^{-1}K^{-1}, which was recently reported [135] to be the range of effective thermal conductivity at intracellular regions.

C. 4. Bio-heat transport model for tissues

The bio-heat transport model is useful to study heat transport in tissues that are far from large blood vessels. In such tissues, the blood flow is assumed to result in uniform volumetric heat production, $Q_b''' = \rho_b \omega_b C_b (T_b - T)$, where ρ_b is the density, C_b is the specific heat of the blood, T_b= 37.1°C is the arterial blood temperature, T is the local tissue temperature, and ω_b is the blood perfusion rate at the tissue [136], [137]. Physiologically, the blood perfusion sustains the nutrient supply to the tissue to maintain a metabolic heat, Q_{met}''' at the tissue, and also functions to stabilize the temperature (thermoregulation) in the tissue. We model the BAT deposit near the skin of the supraclavicular region. The physical and

thermal properties of the tissues are summarized in Table C.1. We used the following blood properties: density (1043 $kg.m^{-3}$), and specific heat (3825 $J.kg^{-1}K^{-1}$) [232].

Table C.1: List of thermal and physical properties of the tissues. Refer [137], [151] for more details.

Tissue	**Density ($kg.m^{-3}$)**	**Specific heat ($J.kg^{-1}K^{-1}$)**	**Thermal conductivity ($Wm^{-1}K^{-1}$)**	**Metabolic heat, Q'''_{met} ($W.m^{-3}$)**	**Blood perfusion rate, ω_b (s^{-1})**	**Size**
Skin	1109	3391	0.37	1827	1.97×10^{-3}	1.5 mm (*t*)
WAT	911	2127	0.18	462	4.98×10^{-4}	10 mm (*t*)
BAT	911	2503	0.26	2579	1.17×10^{-3}	2 cm (*a*) 1 cm (*b*)
Muscle	1090	3421	0.49	1052	7.15×10^{-4}	0.2 cm (*t*)

Figure C.5a shows the computational model representative of the supraclavicular region BAT deposits. BAT volumes vary depending on age, location, and weight of the individual. Here, we use a 2 cm^3 BAT as an example to identify the typical temperature changes expected in a tissue of length-scale ~20 mm [137], [163], [164]. Under cold stimulation ($T_{ambient}$=15°C), the BAT metabolism can be expected to increase by up to 25-fold in humans [233], [234]. In Figure C.5b, we show the temperature contour for a 25-fold increase in BAT metabolism. Figure 4.11 in Chapter 4 shows the temperature change for 5, 10,15, 20, 25-fold increase in BAT metabolism. The blood perfusion rate (ω_b) is also correspondingly increased, since it is the source of nutrients to sustain the

metabolism. Further, we assume that the blood perfusion is reduced by 60% due to cold exposure [235]. A convective heat transfer boundary condition (h=5 $Wm^{-2}K^{-1}$) is used at the skin. The remaining boundaries are treated as adiabatic. Additional details on this bio-heat transport model can be found in other studies [136], [137].

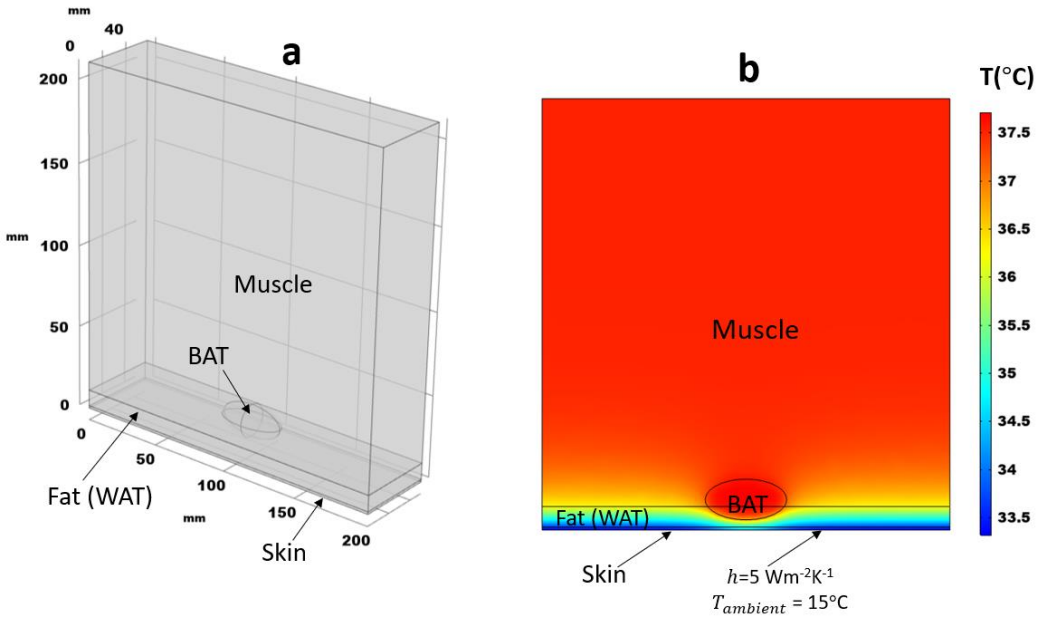

Figure C.5. a) A schematic of the computational domain used for the bio-heat transport model of the supraclavicular region. The dimensions and physical properties are given in Table C.1. b) A cross-sectional temperature contour of the tissues under cold stimulation with a 25-fold increase in BAT metabolism.

APPENDIX D

THERMO-MAGNETO-MECHANICAL MODEL FOR MAGNETOSTRICTIVE MATERIALS

The following equations represent the 1D constitutive relations between the strain (ϵ), magnetization (M), and the applied magnetic field (H). We modify previously reported constitutive relations [177] to include the temperature dependence of Young's modulus at magnetic saturation (E_s).

$$\epsilon = \frac{\sigma}{E_s(1+\gamma\Delta T)} + \alpha\Delta T - \frac{\lambda_s \beta \Delta T M^2}{M_S^2} + \begin{cases} \lambda_S \tanh\left(\frac{\sigma}{\sigma_s}\right) + \frac{\left(1-\tanh\left(\frac{\sigma}{\sigma_s}\right)\right)\lambda_S M^2}{M_S^2}, & \frac{\sigma}{\sigma_s} \geq 0 \\ \frac{\lambda_S}{2}\tanh\left(\frac{2\sigma}{\sigma_s}\right) + \frac{\left(2-\tanh\left(\frac{2\sigma}{\sigma_s}\right)\right)\lambda_S M^2}{2M_S^2}, & \frac{\sigma}{\sigma_s} < 0 \end{cases} \quad (15)$$

$$M = M_S^T \left(\coth\left(\frac{3\chi H_{eff}}{M_S^T}\right) - \frac{M_S^T}{3\chi H_{eff}}\right) \quad (16)$$

$$M_S^T = M_S \sqrt{\frac{\left(1-\frac{\Delta T + T_r}{T_C}\right)}{\left(1-\frac{T_r}{T_C}\right)}} \quad (17)$$

$$H_{eff} = H - \frac{2\lambda_S \beta \Delta T \sigma M}{\mu_0 M_S^2} + \begin{cases} \frac{\left[2\sigma - 2\sigma_S \ln\left(cosh\left(\frac{\sigma}{\sigma_S}\right)\right)\right]\lambda_S M}{\mu_0 M_S^2}, & \frac{\sigma}{\sigma_S} \geq 0 \\ \frac{\left[4\sigma - \sigma_S \ln\left(cosh\left(\frac{2\sigma}{\sigma_S}\right)\right)\right]\lambda_S M}{2\mu_0 M_S^2}, & \frac{\sigma}{\sigma_S} < 0 \end{cases} \quad (18)$$

Where,

ϵ is the strain in the magnetostrictive material,

M is the magnetization of the magnetostrictive material,

M_S is the saturation magnetization at room temperature,

M_S^T is the saturation magnetization at a temperature T,

λ_S is the saturation magnetostrictive strain at room temperature,

H is the applied magnetic field,

H_{eff} is the effective applied magnetic field,

χ is the magnetic susceptibility of the magnetostrictive material,

σ is the compressive film stress,

σ_S is the stress at which magnetostrictive strain λ=λ_S (ref),

ΔT is the change in temperature from a room temperature of 25°C,

T_r is the reference or room temperature,

T_C is the Curie temperature,

α is the thermal coefficient of expansion, which is given by $\alpha = \frac{1}{L}\frac{dL}{dT}$,

β is the temperature coefficient of the magnetostrictive strain (λ), which is given by $\beta = -\frac{1}{\lambda}\frac{d\lambda}{dT}$,

γ is the temperature coefficient of the Young's modulus at magnetic saturation (E_S),

μ_0 is the vacuum permeability.

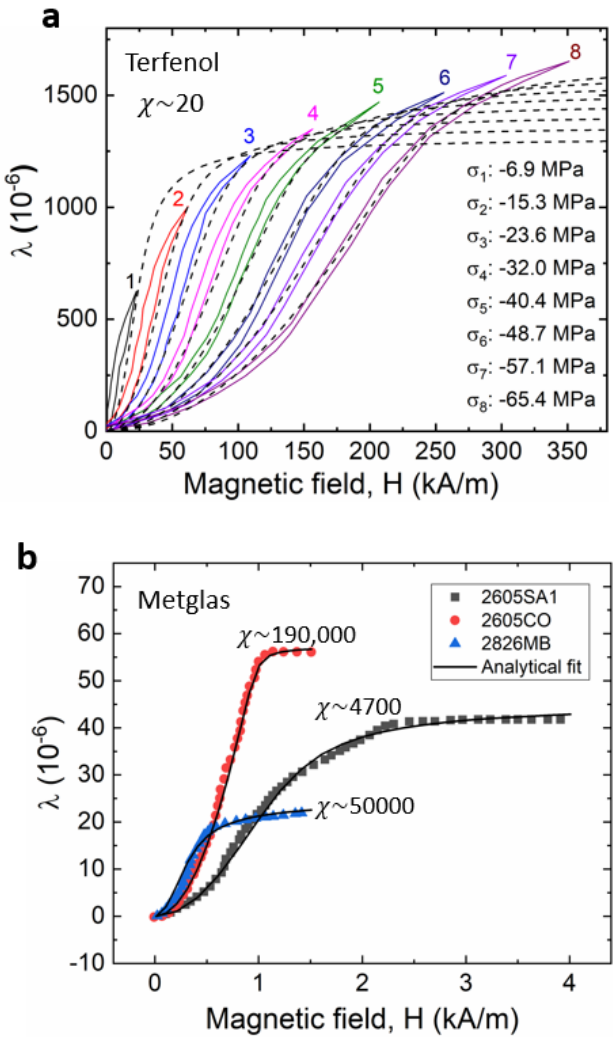

Figure D.1. a) Magnetostrictive strain (λ) of Terfenol rods are shown for different bias fields and compressive stresses. The solid lines correspond to previous experimental data, whereas the dashed lines represent the analytical fit. No fitting parameters were used. The material properties and experimental data we used can be found in Ref. [177], [236], [237]. b) Magnetostrictive strain (λ) of Metglas rods are shown for different bias fields. Dots represent experimental points from previous reports [192], [193], [238]. Solid lines represent the analytical fits. The extracted susceptibility (χ) values are shown in the graph. The corresponding fitted stress (σ) values were 18 MPa, 28 MPa, 25 MPa for 2826, 2605SA, 2605CO, respectively. Other material properties can be found in [188]–[196]. The magnetic susceptibility (χ) is dependent on the annealing conditions [239]–[241], and the obtained susceptibilities from the fit are within the expected order of magnitude based on previous reports [188]–[196].

Fitting parameters:

For Figure 5.6:

Fit parameters:

E_s=84 MPa,

γ=-3.6×10^{-4} K^{-1}, β=1.4×10^{-3} K^{-1},

λ_s=18 ppm,

σ=17 MPa, σ_S=17 MPa,

T_C= 395°C,

M_S=1 T,

χ=50000,

ρ=7900 kg/m^3.

The fit material parameters ($E_s, \gamma, \beta, \lambda_S, T_C, M_S, \chi, \rho$) are in good agreement within an order of magnitude of previously reported values [188]–[196]. The stress values (σ, σ_s) were the only other fit parameters, and they strongly depend on the sensor strip fabrication process. They are typically measured through a stress (σ) vs. magnetostrictive strain curve (λ) [187] and are not known a priori for our magnetostrictive samples.

For Figure 5.9:

Electrical circuit fit parameters: R_e=1 Ω, L^S=0.27 mH (these are in good agreement with the measured values for the ac coil used in the experiment)

Kinematic circuit fit parameters: R=5400 N.m^{-1}s, M=0.3 N.m^{-1}s^2, C^H=28 N^{-1}m, θ=0.09 N.A^{-1}; for finite element simulations: Θ=26, ξ= 0.018 (damping factor).

For Figure 5.13:

The extracted fitting parameters were: E_s=72 MPa, γ=4.2×10^{-3} K^{-1}, β=10^{-3} K^{-1}, λ_s=800 ppm, σ=1 MPa, σ_S=30 MPa, T_C= 380°C, M_S=1.2 T, χ=25, ρ= 9200 kg/m^3. The material parameters used for fitting are in close agreement within an order of magnitude of previously reported values [177], [236], [237]. Any deviation could be attributed to the use of a thin layer (5 μm) of Parylene that we deposited on the Terfenol laminates to prevent corrosion.

REFERENCES

[1] H. Wang *et al.*, “Brain temperature and its fundamental properties: a review for clinical neuroscientists,” *Front. Neurosci.*, vol. 8, Oct. 2014, doi: 10.3389/fnins.2014.00307.

[2] Z. Mariak, “Intracranial temperature recordings in human subjects. The contribution of the neurosurgeon to thermal physiology,” *J. Therm. Biol.*, vol. 27, no. 3, pp. 219–228, Jun. 2002, doi: 10.1016/S0306-4565(01)00087-0.

[3] S. R. Coleshaw, R. N. Van Someren, A. H. Wolff, H. M. Davis, and W. R. Keatinge, “Impaired memory registration and speed of reasoning caused by low body temperature,” *J. Appl. Physiol.*, vol. 55, no. 1, pp. 27–31, Jul. 1983, doi: 10.1152/jappl.1983.55.1.27.

[4] R. Tanimoto *et al.*, “Detection of Temperature Difference in Neuronal Cells,” *Sci. Rep.*, vol. 6, p. 22071, Mar. 2016, doi: 10.1038/srep22071.

[5] Y. Zhao and J. A. Boulant, “Temperature effects on neuronal membrane potentials and inward currents in rat hypothalamic tissue slices,” *J. Physiol.*, vol. 564, no. Pt 1, Art. no. Pt 1, Apr. 2005, doi: 10.1113/jphysiol.2004.075473.

[6] A. El Hady and B. B. Machta, “Mechanical surface waves accompany action potential propagation,” *Nat. Commun.*, vol. 6, no. 1, Art. no. 1, Mar. 2015, doi: 10.1038/ncomms7697.

[7] M. K. Sato *et al.*, “Temperature Changes in Brown Adipocytes Detected with a Bimaterial Microcantilever,” *Biophys. J.*, vol. 106, no. 11, pp. 2458–2464, Jun. 2014, doi: 10.1016/j.bpj.2014.04.044.

[8] N. Inomata, M. Toda, M. Sato, A. Ishijima, and T. Ono, “Pico calorimeter for detection of heat produced in an individual brown fat cell,” *Appl. Phys. Lett.*, vol. 100, no. 15, p. 154104, Apr. 2012, doi: 10.1063/1.3701720.

[9] J.-S. Kang, “Theoretical model and characteristics of mitochondrial thermogenesis,” *Biophys. Rep.*, vol. 4, no. 2, Art. no. 2, Apr. 2018, doi: 10.1007/s41048-018-0054-2.

[10] B. B. Lowell and B. M. Spiegelman, “Towards a molecular understanding of adaptive thermogenesis,” *Nature*, vol. 404, no. 6778, Art. no. 6778, Apr. 2000, doi: 10.1038/35007527.

[11] L. JANSKý, “Non-Shivering Thermogenesis and Its Thermoregulatory Significance,” *Biol. Rev.*, vol. 48, no. 1, Art. no. 1, 1973, doi: 10.1111/j.1469-185X.1973.tb01115.x.

[12] Z. B. Andrews, S. Diano, and T. L. Horvath, “Mitochondrial uncoupling proteins in the cns: in support of function and survival,” *Nat. Rev. Neurosci.*, vol. 6, no. 11, Art. no. 11, Nov. 2005, doi: 10.1038/nrn1767.

[13] H. Kondo, R. Harano, M. Nakaya, and S. Watabe, “Characterization of goldfish heat shock protein–30 induced upon severe heat shock in cultured cells,” *Cell Stress Chaperones*, vol. 9, no. 4, Art. no. 4, Oct. 2004, doi: 10.1379/CSC-55R.1.

[14] A. K. Velichko, E. N. Markova, N. V. Petrova, S. V. Razin, and O. L. Kantidze, “Mechanisms of heat shock response in mammals,” *Cell. Mol. Life Sci. CMLS*, vol. 70, no. 22, Art. no. 22, Nov. 2013, doi: 10.1007/s00018-013-1348-7.

[15] J. A. Bartz and J. K. Brecht, *Postharvest physiology and pathology of vegetables*, vol. 123. CRC Press, 2002.

[16] P. R. Rich, “The molecular machinery of Keilin’s respiratory chain,” *Biochem. Soc. Trans.*, vol. 31, no. 6, pp. 1095–1105, Dec. 2003, doi: 10.1042/bst0311095.

[17] L. Squire, D. Berg, F. E. Bloom, S. Du Lac, A. Ghosh, and N. C. Spitzer, *Fundamental neuroscience*. Academic Press, 2012.

[18] B. Korzeniewski and W. Froncisz, “An extended dynamic model of oxidative phosphorylation,” *Biochim. Biophys. Acta BBA - Bioenerg.*, vol. 1060, no. 2, Art. no. 2, Oct. 1991, doi: 10.1016/S0005-2728(09)91009-X.

[19] B. M. Kenwood *et al.*, “Identification of a novel mitochondrial uncoupler that does not depolarize the plasma membrane,” *Mol. Metab.*, vol. 3, no. 2, Art. no. 2, Apr. 2014, doi: 10.1016/j.molmet.2013.11.005.

[20] M. C. Rajagopal *et al.*, “Transient heat release during induced mitochondrial proton uncoupling,” *Commun. Biol.*, vol. 2, no. 1, Art. no. 1, Jul. 2019, doi: 10.1038/s42003-019-0535-y.

[21] K. Okabe, N. Inada, C. Gota, Y. Harada, T. Funatsu, and S. Uchiyama, “Intracellular temperature mapping with a fluorescent polymeric thermometer and fluorescence lifetime imaging microscopy,” *Nat. Commun.*, vol. 3, p. 705, Feb. 2012, doi: 10.1038/ncomms1714.

[22] S. Kiyonaka *et al.*, “Genetically encoded fluorescent thermosensors visualize subcellular thermoregulation in living cells,” *Nat. Methods*, vol. 10, no. 12, Art. no. 12, Dec. 2013, doi: 10.1038/nmeth.2690.

[23] T. Tsuji, K. Ikado, H. Koizumi, S. Uchiyama, and K. Kajimoto, “Difference in intracellular temperature rise between matured and precursor brown adipocytes in response to uncoupler and β-adrenergic agonist stimuli,” *Sci. Rep.*, vol. 7, no. 1, Art. no. 1, Oct. 2017, doi: 10.1038/s41598-017-12634-7.

[24] G. Baffou, H. Rigneault, D. Marguet, and L. Jullien, “A critique of methods for temperature imaging in single cells,” *Nat. Methods*, vol. 11, no. 9, Art. no. 9, Sep. 2014, doi: 10.1038/nmeth.3073.

[25] A. Fedorenko, P. V. Lishko, and Y. Kirichok, “Mechanism of fatty-acid-dependent UCP1 uncoupling in brown fat mitochondria,” *Cell*, vol. 151, no. 2, Art. no. 2, Oct. 2012, doi: 10.1016/j.cell.2012.09.010.

[26] M. J. Thrippleton *et al.*, “Reliability of MRSI brain temperature mapping at 1.5 and 3 T,” *NMR Biomed.*, vol. 27, no. 2, pp. 183–190, 2014, doi: 10.1002/nbm.3050.

[27] T. L. Horvath, C. H. Warden, M. Hajos, A. Lombardi, F. Goglia, and S. Diano, “Brain Uncoupling Protein 2: Uncoupled Neuronal Mitochondria Predict Thermal Synapses in Homeostatic Centers,” *J. Neurosci.*, vol. 19, no. 23, pp. 10417–10427, Dec. 1999, doi: 10.1523/JNEUROSCI.19-23-10417.1999.

[28] B. C. Abbott, A. V. Hill, and J. V. Howarth, “The positive and negative heat production associated with a nerve impulse,” *Proc. R. Soc. Lond. Ser. B - Biol. Sci.*, vol. 148, no. 931, pp. 149–187, Feb. 1958, doi: 10.1098/rspb.1958.0012.

[29] J. V. Howarth, R. D. Keynes, and J. M. Ritchie, “The origin of the initial heat associated with a single impulse in mammalian non-myelinated nerve fibres,” *J. Physiol.*, vol. 194, no. 3, pp. 745–793, Feb. 1968.

[30] J. M. Ritchie and R. D. Keynes, “The production and absorption of heat associated with electrical activity in nerve and electric organ,” *Q. Rev. Biophys.*, vol. 18, no. 4, pp. 451–476, Nov. 1985, doi: 10.1017/S0033583500005382.

[31] I. Tasaki, K. Kusano, and P. M. Byrne, “Rapid mechanical and thermal changes in the garfish olfactory nerve associated with a propagated impulse,” *Biophys. J.*, vol. 55, no. 6, pp. 1033–1040, Jun. 1989, doi: 10.1016/S0006-3495(89)82902-9.

[32] K. Nag, *Structure and dynamics of membranous interfaces*. Wiley Hoboken, 2008.

[33] D. G. Margineanu and E. Schoffeniels, “Molecular events and energy changes during the action potential,” *Proc. Natl. Acad. Sci.*, vol. 74, no. 9, pp. 3810–3813, Sep. 1977, doi: 10.1073/pnas.74.9.3810.

[34] K. Kusano and I. Tasaki, “Heat generation associated with synaptic transmission in the mammalian superior cervical ganglion,” *J. Neurosci. Res.*, vol. 25, no. 2, pp. 249–255, 1990, doi: 10.1002/jnr.490250214.

[35] J. V. Howarth, R. D. Keynes, J. M. Ritchie, and A. von Muralt, “The heat production associated with the passage of a single impulse in pike olfactory nerve fibres.,” *J. Physiol.*, vol. 249, no. 2, pp. 349–368, 1975, doi: 10.1113/jphysiol.1975.sp011019.

[36] A. L. Hodgkin and A. F. Huxley, “A quantitative description of membrane current and its application to conduction and excitation in nerve,” *J. Physiol.*, vol. 117, no. 4, pp. 500–544, 1952, doi: 10.1113/jphysiol.1952.sp004764.

[37] T. Heimburg and A. D. Jackson, “On soliton propagation in biomembranes and nerves,” *Proc. Natl. Acad. Sci.*, vol. 102, no. 28, pp. 9790–9795, Jul. 2005, doi: 10.1073/pnas.0503823102.

[38] L. D. Mosgaard, A. D. Jackson, and T. Heimburg, “Chapter Two - Low-Frequency Sound Propagation in Lipid Membranes,” in *Advances in Planar Lipid Bilayers and Liposomes*, vol. 16, A. Iglič, Ed. Academic Press, 2012, pp. 51–74.

[39] K. Kaufmann, “Action potentials and electrochemical coupling in the macroscopic chiral phospholipid membrane. Caruaru, Brazil,” 1989.

[40] I. Tasaki and P. M. Byrne, “Heat Production Associated with a Propagated Impulse in Bullfrog Myelinated Nerve Fibers,” *Jpn. J. Physiol.*, vol. 42, no. 5, pp. 805–813, 1992, doi: 10.2170/jjphysiol.42.805.

[41] S. Hong *et al.*, “Sub-nanowatt microfluidic single-cell calorimetry,” *Nat. Commun.*, vol. 11, no. 1, Art. no. 1, Jun. 2020, doi: 10.1038/s41467-020-16697-5.

[42] S. Hur, R. Mittapally, S. Yadlapalli, P. Reddy, and E. Meyhofer, “Sub-nanowatt resolution direct calorimetry for probing real-time metabolic activity of individual C. elegans worms,” *Nat. Commun.*, vol. 11, no. 1, Art. no. 1, Jun. 2020, doi: 10.1038/s41467-020-16690-y.

[43] J. R. Yeager and R. J. Erdman, *Low Level Measurements: For Effective Low Current, Low Voltage, and High Impedance Measurements*. Keithley Instruments, 1984.

[44] L. M. Dell’Acqua-Bellavitis, “Lab-on-a-chip devices with nanophase surface topography for neural electrophysiological applications,” Rensselaer Polytechnic Institute, 2007.

[45] A. V. Hill and J. V. Howarth, “The initial heat production of stimulated nerve,” *Proc. R. Soc. Lond. Ser. B - Biol. Sci.*, vol. 149, no. 935, pp. 167–175, Dec. 1958, doi: 10.1098/rspb.1958.0059.

[46] M. C. Rajagopal, K. V. Valavala, D. Gelda, J. Ma, and S. Sinha, “Fabrication and characterization of thermocouple probe for use in intracellular thermometry,” *Sens. Actuators Phys.*, vol. 272, pp. 253–258, Apr. 2018, doi: 10.1016/j.sna.2018.02.004.

[47] S. F. Morrison, C. J. Madden, and D. Tupone, “Central Neural Regulation of Brown Adipose Tissue Thermogenesis and Energy Expenditure,” *Cell Metab.*, vol. 19, no. 5, pp. 741–756, May 2014, doi: 10.1016/j.cmet.2014.02.007.

[48] R. C. Rogers, M. J. Barnes, and G. E. Hermann, “Leptin ‘gates’ thermogenic action of thyrotropin-releasing hormone in the hindbrain,” *Brain Res.*, vol. 1295, pp. 135–141, Oct. 2009, doi: 10.1016/j.brainres.2009.07.063.

[49] R. K. Jain, S. A. Shah, and P. L. Finney, “Continuous Noninvasive Monitoring of pH and Temperature in Rat Walker 256 Carcinoma During Normoglycemia and Hyperglycemia,” *JNCI J. Natl. Cancer Inst.*, vol. 73, no. 2, pp. 429–436, Aug. 1984, doi: 10.1093/jnci/73.2.429.

[50] R. K. Jain, F. H. Grantham, and P. M. Gullino, “Blood Flow and Heat Transfer in Walker 256 Mammary Carcinoma,” *JNCI J. Natl. Cancer Inst.*, vol. 62, no. 4, pp. 927–933, Apr. 1979, doi: 10.1093/jnci/62.4.927.

[51] P. M. Gullino, P.-N. Yi, and F. H. Grantham, “Relationship Between Temperature and Blood Supply or Consumption of Oxygen and Glucose by Rat Mammary Carcinomas,” *JNCI J. Natl. Cancer Inst.*, vol. 60, no. 4, pp. 835–847, Apr. 1978, doi: 10.1093/jnci/60.4.835.

[52] P. M. Gullino, R. K. Jain, and F. H. Grantham, “Temperature Gradients and Local Perfusion in a Mammary Carcinoma,” *JNCI J. Natl. Cancer Inst.*, vol. 68, no. 3, pp. 519–533, Mar. 1982, doi: 10.1093/jnci/68.3.519.

[53] P. G. Heytler, “Uncouplers of oxidative phosphorylation,” in *Methods in Enzymology*, vol. 55, Academic Press, 1979, pp. 462–472.

[54] S. W. Perry, J. P. Norman, J. Barbieri, E. B. Brown, and H. A. Gelbard, “Mitochondrial membrane potential probes and the proton gradient: a practical usage guide,” *BioTechniques*, vol. 50, no. 2, Art. no. 2, Feb. 2011, doi: 10.2144/000113610.

[55] R. C. Scaduto and L. W. Grotyohann, “Measurement of mitochondrial membrane potential using fluorescent rhodamine derivatives.,” *Biophys. J.*, vol. 76, no. 1 Pt 1, Art. no. 1 Pt 1, Jan. 1999.

[56] M. Suzuki, V. Zeeb, S. Arai, K. Oyama, and S. Ishiwata, “The 105 gap issue between calculation and measurement in single-cell thermometry,” *Nat. Methods*, vol. 12, no. 9, Art. no. 9, Sep. 2015, doi: 10.1038/nmeth.3551.

[57] S. Kiyonaka, R. Sakaguchi, I. Hamachi, T. Morii, T. Yoshizaki, and Y. Mori, “Validating subcellular thermal changes revealed by fluorescent thermosensors,” *Nat. Methods*, vol. 12, no. 9, Art. no. 9, Sep. 2015, doi: 10.1038/nmeth.3548.

[58] W. Tian *et al.*, “A high precision apparatus for intracellular thermal response at single-cell level,” *Nanotechnology*, vol. 26, no. 35, Art. no. 35, Aug. 2015, doi: 10.1088/0957-4484/26/35/355501.

[59] C. Wang *et al.*, “Determining intracellular temperature at single-cell level by a novel thermocouple method,” *Cell Res.*, vol. 21, no. 10, Art. no. 10, Oct. 2011, doi: 10.1038/cr.2011.117.

[60] S. Arai, S.-C. Lee, D. Zhai, M. Suzuki, and Y. T. Chang, “A Molecular Fluorescent Probe for Targeted Visualization of Temperature at the Endoplasmic Reticulum,” *Sci. Rep.*, vol. 4, no. 1, Art. no. 1, Oct. 2014, doi: 10.1038/srep06701.

[61] Y. Takei *et al.*, “A Nanoparticle-Based Ratiometric and Self-Calibrated Fluorescent Thermometer for Single Living Cells,” *ACS Nano*, vol. 8, no. 1, pp. 198–206, Jan. 2014, doi: 10.1021/nn405456e.

[62] A. Vyšniauskas, M. Qurashi, N. Gallop, M. Balaz, H. L. Anderson, and M. K. Kuimova, “Unravelling the effect of temperature on viscosity-sensitive

fluorescent molecular rotors," *Chem. Sci.*, vol. 6, no. 10, pp. 5773–5778, 2015, doi: 10.1039/C5SC02248G.

[63] A. D. Pickel, A. Teitelboim, E. M. Chan, N. J. Borys, P. J. Schuck, and C. Dames, "Apparent self-heating of individual upconverting nanoparticle thermometers," *Nat. Commun.*, vol. 9, no. 1, Art. no. 1, Nov. 2018, doi: 10.1038/s41467-018-07361-0.

[64] I. Watanabe and S. Okada, "Effects of temperature on growth rate of cultured mammalian cells (l5178y)," *J. Cell Biol.*, vol. 32, no. 2, Art. no. 2, Feb. 1967, doi: 10.1083/jcb.32.2.309.

[65] L. A. Sonna, J. Fujita, S. L. Gaffin, and C. M. Lilly, "Invited review: Effects of heat and cold stress on mammalian gene expression," *J. Appl. Physiol. Bethesda Md 1985*, vol. 92, no. 4, Art. no. 4, Apr. 2002, doi: 10.1152/japplphysiol.01143.2001.

[66] P. L. Privalov and N. N. Khechinashvili, "A thermodynamic approach to the problem of stabilization of globular protein structure: A calorimetric study," *J. Mol. Biol.*, vol. 86, no. 3, Art. no. 3, Jul. 1974, doi: 10.1016/0022-2836(74)90188-0.

[67] G. N. Somero, "Proteins and Temperature," *Annu. Rev. Physiol.*, vol. 57, no. 1, Art. no. 1, Oct. 1995, doi: 10.1146/annurev.ph.57.030195.000355.

[68] E. Tanaka, M. Yamamura, A. Yamakawa, T. Fujise, and S. Nakano, "Microcalorimetric measurements of heat production in isolated rat brown adipocytes," *Biochem. Int.*, vol. 26, no. 5, Art. no. 5, Apr. 1992.

[69] U. R. Acharya, E. Y. K. Ng, J.-H. Tan, and S. V. Sree, "Thermography based breast cancer detection using texture features and Support Vector Machine," *J. Med. Syst.*, vol. 36, no. 3, Art. no. 3, Jun. 2012, doi: 10.1007/s10916-010-9611-z.

[70] A. Helmy, M. Holdmann, and M. Rizkalla, "Application of thermography for non-invasive diagnosis of thyroid gland disease," *IEEE Trans. Biomed. Eng.*, vol. 55, no. 3, Art. no. 3, Mar. 2008, doi: 10.1109/TBME.2008.915731.

[71] C. Guy, F. Kaplan, J. Kopka, J. Selbig, and D. K. Hincha, "Metabolomics of temperature stress," *Physiol. Plant.*, vol. 132, no. 2, Art. no. 2, Feb. 2008, doi: 10.1111/j.1399-3054.2007.00999.x.

[72] I. Tasaki and T. Nakaye, "Heat generated by the dark-adapted squid retina in response to light pulses," *Science*, vol. 227, no. 4687, Art. no. 4687, Feb. 1985, doi: 10.1126/science.3969556.

[73] S. Gupta and P. Kulhara, "Cellular and molecular mechanisms of drug dependence: An overview and update," *Indian J. Psychiatry*, vol. 49, no. 2, Art. no. 2, 2007, doi: 10.4103/0019-5545.33253.

[74] J. S. Donner, S. A. Thompson, M. P. Kreuzer, G. Baffou, and R. Quidant, "Mapping Intracellular Temperature Using Green Fluorescent Protein," *Nano Lett.*, vol. 12, no. 4, Art. no. 4, Apr. 2012, doi: 10.1021/nl300389y.

[75] G. Fish *et al.*, “Ultrafast response micropipette-based submicrometer thermocouple,” *Rev. Sci. Instrum.*, vol. 66, no. 5, Art. no. 5, May 1995, doi: 10.1063/1.1145498.

[76] M. Watanabe, N. Kakuta, K. Mabuchi, and Y. Yamada, “Micro-thermocouple probe for measurement of cellular thermal responses,” in *Conference proceedings: ... Annual International Conference of the IEEE Engineering in Medicine and Biology Society. IEEE Engineering in Medicine and Biology Society. Annual Conference*, 2005, vol. 2005, pp. 4858–4861, doi: 10.1109/IEMBS.2005.1615560.

[77] R. Shrestha, T.-Y. Choi, W. Chang, and D. Kim, “A High-Precision Micropipette Sensor for Cellular-Level Real-Time Thermal Characterization,” *Sensors*, vol. 11, no. 9, Art. no. 9, Sep. 2011, doi: 10.3390/s110908826.

[78] L. Tauc, “Site of Origin and Propagation of Spike in the Giant Neuron of Aplysia,” *J. Gen. Physiol.*, vol. 45, no. 6, Art. no. 6, Jul. 1962.

[79] S. Herth, M. Giesguth, W. Wedel, G. Reiss, and K.-J. Dietz, “Thermomicrocapillaries as temperature biosensors in single cells,” *Appl. Phys. Lett.*, vol. 102, no. 10, Art. no. 10, Mar. 2013, doi: 10.1063/1.4795289.

[80] G. S. Wilson and R. Gifford, “Biosensors for real-time in vivo measurements,” *Biosens. Bioelectron.*, vol. 20, no. 12, Art. no. 12, Jun. 2005, doi: 10.1016/j.bios.2004.12.003.

[81] F. Yu *et al.*, “Design, fabrication, and characterization of polymer-based cantilever probes for atomic force microscopes,” *J. Vac. Sci. Technol. B*, vol. 34, no. 6, Art. no. 6, Nov. 2016, doi: 10.1116/1.4960726.

[82] R. K. Ulrich, W. D. Brown, S. S. Ang, S. Yi, J. Sweet, and D. Peterson, “PECVD silicon and nitride postbond films for protecting bondpads, bonds and bondwires from corrosion failure,” in *1991 Proceedings 41st Electronic Components Technology Conference*, May 1991, pp. 738–744, doi: 10.1109/ECTC.1991.163962.

[83] E. Cianci, A. Coppa, and V. Foglietti, “Young’s modulus and residual stress of DF PECVD silicon nitride for MEMS free-standing membranes,” *Microelectron. Eng.*, vol. 84, no. 5, Art. no. 5, May 2007, doi: 10.1016/j.mee.2007.01.056.

[84] A. A. Sharp, A. M. Ortega, D. Restrepo, D. Curran-Everett, and K. Gall, “In Vivo Penetration Mechanics and Mechanical Properties of Mouse Brain Tissue at Micrometer Scales,” *IEEE Trans. Biomed. Eng.*, vol. 56, no. 1, Art. no. 1, Jan. 2009, doi: 10.1109/TBME.2008.2003261.

[85] G. P. Szakmany, P. M. Krenz, L. C. Schneider, A. O. Orlov, G. H. Bernstein, and W. Porod, “Nanowire Thermocouple Characterization Platform,” *IEEE Trans. Nanotechnol.*, vol. 12, no. 3, pp. 309–313, May 2013, doi: 10.1109/TNANO.2013.2247057.

[86] G. Langer, J. Hartmann, and M. Reichling, “Thermal conductivity of thin metallic films measured by photothermal profile analysis,” *Rev. Sci. Instrum.*, vol. 68, no. 3, Art. no. 3, Mar. 1997, doi: 10.1063/1.1147638.

[87] S.-M. Lee and D. G. Cahill, “Heat transport in thin dielectric films,” *J. Appl. Phys.*, vol. 81, no. 6, Art. no. 6, Mar. 1997, doi: 10.1063/1.363923.

[88] “Thor labs thermally conductive double-sided tape specifications Sheet TCDT1.” https://www.thorlabs.com/thorproduct.cfm?partnumber=TCDT1.

[89] S. Huang, X. Ruan, X. Fu, and H. Yang, “Measurement of the thermal transport properties of dielectric thin films using the micro-Raman method,” *J. Zhejiang Univ.-Sci. A*, vol. 10, no. 1, Art. no. 1, Jan. 2009, doi: 10.1631/jzus.A0820493.

[90] T. Jeong, J.-G. Zhu, S. Chung, and M. R. Gibbons, “Thermal boundary resistance for gold and CoFe alloy on silicon nitride films,” *J. Appl. Phys.*, vol. 111, no. 8, Art. no. 8, Apr. 2012, doi: 10.1063/1.3703571.

[91] M. Chertok *et al.*, “Thermal and Tensile Strength Testing of Thermally-Conductive Adhesives and Carbon Foam,” *J. Instrum.*, vol. 12, no. 01, Art. no. 01, Jan. 2017, doi: 10.1088/1748-0221/12/01/P01010.

[92] X. J. Hu, A. Jain, and K. E. Goodson, “Investigation of the natural convection boundary condition in microfabricated structures,” *Int. J. Therm. Sci.*, vol. 47, no. 7, Art. no. 7, Jul. 2008, doi: 10.1016/j.ijthermalsci.2007.07.011.

[93] D. W. Denlinger *et al.*, “Thin film microcalorimeter for heat capacity measurements from 1.5 to 800 K,” *Rev. Sci. Instrum.*, vol. 65, no. 4, Art. no. 4, Apr. 1994, doi: 10.1063/1.1144925.

[94] B. L. Zink and F. Hellman, “Specific heat and thermal conductivity of low-stress amorphous Si–N membranes,” *Solid State Commun.*, vol. 129, no. 3, Art. no. 3, Jan. 2004, doi: 10.1016/j.ssc.2003.08.048.

[95] A. Okhotin, A. Pushkarskij, and V. Gorbachev, “Thermophysical properties of semiconductors,” 1972.

[96] S. Sinha and M. C. Rajagopal, “Microscale thermocouple probe for intracellular temperature measurements,” US20200249103A1, Aug. 06, 2020.

[97] M. Klingenspor, “Cold-induced recruitment of brown adipose tissue thermogenesis,” *Exp. Physiol.*, vol. 88, no. 1, Art. no. 1, Jan. 2003, doi: 10.1113/eph8802508.

[98] D. G. Nicholls and R. M. Locke, “Thermogenic mechanisms in brown fat.,” *Physiol. Rev.*, vol. 64, no. 1, Art. no. 1, Jan. 1984, doi: 10.1152/physrev.1984.64.1.1.

[99] G. Baffou, H. Rigneault, D. Marguet, and L. Jullien, “Reply to: ‘Validating subcellular thermal changes revealed by fluorescent thermosensors’ and ‘The 10 5 gap issue between calculation and measurement in single-cell

thermometry,'" *Nat. Methods*, vol. 12, no. 9, Art. no. 9, Sep. 2015, doi: 10.1038/nmeth.3552.

[100] A. M. Bertholet *et al.*, "Mitochondrial Patch Clamp of Beige Adipocytes Reveals UCP1-Positive and UCP1-Negative Cells Both Exhibiting Futile Creatine Cycling," *Cell Metab.*, vol. 25, no. 4, Art. no. 4, Apr. 2017, doi: 10.1016/j.cmet.2017.03.002.

[101] T. Durand, M.-C. Delmas-Beauvieux, P. Canioni, and J.-L. Gallis, "Role of Intracellular Buffering Power on the Mitochondria-Cytosol pH Gradient in the Rat Liver Perfused at 4°C," *Cryobiology*, vol. 38, no. 1, pp. 68–80, Feb. 1999, doi: 10.1006/cryo.1999.2152.

[102] D. Poburko, J. Santo-Domingo, and N. Demaurex, "Dynamic Regulation of the Mitochondrial Proton Gradient during Cytosolic Calcium Elevations," *J. Biol. Chem.*, vol. 286, no. 13, pp. 11672–11684, Apr. 2011, doi: 10.1074/jbc.M110.159962.

[103] T.-R. Xie, C.-F. Liu, and J.-S. Kang, "Dye-based mito-thermometry and its application in thermogenesis of brown adipocytes," *Biophys. Rep.*, vol. 3, no. 4, Art. no. 4, Dec. 2017, doi: 10.1007/s41048-017-0039-6.

[104] T.-R. Xie, C.-F. Liu, and J.-S. Kang, "Sympathetic transmitters control thermogenic efficacy of brown adipocytes by modulating mitochondrial complex V," *Signal Transduct. Target. Ther.*, vol. 2, no. 1, Art. no. 1, Nov. 2017, doi: 10.1038/sigtrans.2017.60.

[105] F. Yang *et al.*, "Measurement of local temperature increments induced by cultured HepG2 cells with micro-thermocouples in a thermally stabilized system," *Sci. Rep.*, vol. 7, no. 1, Art. no. 1, May 2017, doi: 10.1038/s41598-017-01891-1.

[106] L. L. Moroz, "Aplysia," *Curr. Biol. CB*, vol. 21, no. 2, Art. no. 2, Jan. 2011, doi: 10.1016/j.cub.2010.11.028.

[107] M. Mandrioli, L. Mola, B. Cuoghi, and D. Sonetti, "Endoreplication: a molecular trick during animal neuron evolution," *Q. Rev. Biol.*, vol. 85, no. 2, Art. no. 2, Jun. 2010, doi: 10.1086/652341.

[108] C. H. Lee, J. J. Flint, B. Hansen, and S. J. Blackband, "Investigation of the subcellular architecture of L7 neurons of Aplysia californica using magnetic resonance microscopy (MRM) at 7.8 microns," *Sci. Rep.*, vol. 5, Jun. 2015, doi: 10.1038/srep11147.

[109] J. Rosenbluth, "The visceral ganglion of Aplysia Californica," *Z. Für Zellforsch. Mikrosk. Anat.*, vol. 60, no. 2, Art. no. 2, Mar. 1963, doi: 10.1007/BF00350477.

[110] H. Terada, "The interaction of highly active uncouplers with mitochondria," *Biochim. Biophys. Acta BBA - Rev. Bioenerg.*, vol. 639, no. 3, Art. no. 3, Dec. 1981, doi: 10.1016/0304-4173(81)90011-2.

[111] D. W. Summers, A. DiAntonio, and J. Milbrandt, “Mitochondrial dysfunction induces Sarm1-dependent cell death in sensory neurons,” *J. Neurosci. Off. J. Soc. Neurosci.*, vol. 34, no. 28, Art. no. 28, Jul. 2014, doi: 10.1523/JNEUROSCI.0877-14.2014.

[112] J. H. Yang, R. L. Gross, S. F. Basinger, and S. M. Wu, “Apoptotic cell death of cultured salamander photoreceptors induced by cccp: CsA-insensitive mitochondrial permeability transition,” *J. Cell Sci.*, vol. 114, no. 9, Art. no. 9, May 2001.

[113] C. M. Hickey, J. E. Geiger, C. J. Groten, and N. S. Magoski, “Mitochondrial Ca2+ activates a cation current in Aplysia bag cell neurons,” *J. Neurophysiol.*, vol. 103, no. 3, Art. no. 3, Mar. 2010, doi: 10.1152/jn.01121.2009.

[114] R. T. ElAfandy *et al.*, “Nanomembrane-Based, Thermal-Transport Biosensor for Living Cells,” *Small Weinh. Bergstr. Ger.*, vol. 13, no. 7, Art. no. 7, 2017, doi: 10.1002/smll.201603080.

[115] K. K. Badal *et al.*, “Synapse Formation Activates a Transcriptional Program for Persistent Enhancement in the Bi-directional Transport of Mitochondria,” *Cell Rep.*, vol. 26, no. 3, Art. no. 3, 15 2019, doi: 10.1016/j.celrep.2018.12.073.

[116] H. R. Gillette, *Microstructural and Ultrastructural Studies on Identified Neurons of the Abdominal Ganglion of Aplysia Californica*. Thesis (Ph.D.)--University of Toronto, 1974.

[117] V. M. Sukhorukov, D. Dikov, A. S. Reichert, and M. Meyer-Hermann, “Emergence of the Mitochondrial Reticulum from Fission and Fusion Dynamics,” *PLOS Comput. Biol.*, vol. 8, no. 10, Art. no. 10, Oct. 2012, doi: 10.1371/journal.pcbi.1002745.

[118] P. F. Drake and R. J. Lasek, “Regional differences in the neuronal cytoskeleton,” *J. Neurosci.*, vol. 4, no. 5, Art. no. 5, May 1984, doi: 10.1523/JNEUROSCI.04-05-01173.1984.

[119] T. Kreiner, W. Sossin, and R. H. Scheller, “Localization of Aplysia neurosecretory peptides to multiple populations of dense core vesicles,” *J. Cell Biol.*, vol. 102, no. 3, Art. no. 3, Mar. 1986, doi: 10.1083/jcb.102.3.769.

[120] Y. Tai *et al.*, “Mitochondrial uncoupler BAM15 inhibits artery constriction and potently activates AMPK in vascular smooth muscle cells,” *Acta Pharm. Sin. B*, vol. 8, no. 6, Art. no. 6, Oct. 2018, doi: 10.1016/j.apsb.2018.07.010.

[121] R. I. Morimoto, “Cells in stress: transcriptional activation of heat shock genes,” *Science*, vol. 259, no. 5100, Art. no. 5100, Mar. 1993, doi: 10.1126/science.8451637.

[122] B. Hildebrandt *et al.*, “The cellular and molecular basis of hyperthermia,” *Crit. Rev. Oncol. Hematol.*, vol. 43, no. 1, Art. no. 1, Jul. 2002, doi: 10.1016/s1040-8428(01)00179-2.

[123] R. San Gil, L. Ooi, J. J. Yerbury, and H. Ecroyd, “The heat shock response in neurons and astroglia and its role in neurodegenerative diseases,” *Mol.*

Neurodegener., vol. 12, no. 1, Art. no. 1, 18 2017, doi: 10.1186/s13024-017-0208-6.

[124] C. Mailhos, M. K. Howard, and D. S. Latchman, "Heat shock protects neuronal cells from programmed cell death by apoptosis," *Neuroscience*, vol. 55, no. 3, Art. no. 3, Aug. 1993, doi: 10.1016/0306-4522(93)90428-i.

[125] C. Jolly, Y. Usson, and R. I. Morimoto, "Rapid and reversible relocalization of heat shock factor 1 within seconds to nuclear stress granules," *Proc. Natl. Acad. Sci.*, vol. 96, no. 12, Art. no. 12, Jun. 1999, doi: 10.1073/pnas.96.12.6769.

[126] A. S. Verkman, "Solute and macromolecule diffusion in cellular aqueous compartments," *Trends Biochem. Sci.*, vol. 27, no. 1, pp. 27–33, Jan. 2002, doi: 10.1016/S0968-0004(01)02003-5.

[127] M. Suzuki and T. Plakhotnik, "The challenge of intracellular temperature," *Biophys. Rev.*, vol. 12, no. 2, pp. 593–600, Apr. 2020, doi: 10.1007/s12551-020-00683-8.

[128] P. Kapitza, "The study of heat transfer in helium II," *J PhysMoscow*, vol. 4, p. 181, 1941.

[129] Z. Ge, D. G. Cahill, and P. V. Braun, "AuPd Metal Nanoparticles as Probes of Nanoscale Thermal Transport in Aqueous Solution," *J. Phys. Chem. B*, vol. 108, no. 49, pp. 18870–18875, Dec. 2004, doi: 10.1021/jp048375k.

[130] O. M. Wilson, X. Hu, D. G. Cahill, and P. V. Braun, "Colloidal metal particles as probes of nanoscale thermal transport in fluids," *Phys. Rev. B*, vol. 66, no. 22, p. 224301, Dec. 2002, doi: 10.1103/PhysRevB.66.224301.

[131] Z. Ge, D. G. Cahill, and P. V. Braun, "Thermal Conductance of Hydrophilic and Hydrophobic Interfaces," *Phys. Rev. Lett.*, vol. 96, no. 18, p. 186101, May 2006, doi: 10.1103/PhysRevLett.96.186101.

[132] H. M. Duong, D. V. Papavassiliou, K. J. Mullen, B. L. Wardle, and S. Maruyama, "A numerical study on the effective thermal conductivity of biological fluids containing single-walled carbon nanotubes," *Int. J. Heat Mass Transf.*, vol. 52, no. 23, pp. 5591–5597, Nov. 2009, doi: 10.1016/j.ijheatmasstransfer.2009.06.016.

[133] A. Lervik, F. Bresme, S. Kjelstrup, D. Bedeaux, and J. M. Rubi, "Heat transfer in protein – water interfaces," *Phys. Chem. Chem. Phys.*, vol. 12, no. 7, pp. 1610–1617, 2010, doi: 10.1039/B918607G.

[134] B. M. Foley *et al.*, "Protein Thermal Conductivity Measured in the Solid State Reveals Anharmonic Interactions of Vibrations in a Fractal Structure," *J. Phys. Chem. Lett.*, vol. 5, no. 7, pp. 1077–1082, Apr. 2014, doi: 10.1021/jz500174x.

[135] S. Sotoma *et al.*, "In situ measurement of intracellular thermal conductivity using heater-thermometer hybrid diamond nanosensor," *bioRxiv*, p. 2020.06.03.126789, Jun. 2020, doi: 10.1101/2020.06.03.126789.

[136] J. Crezee and J. J. W. Lagendijk, “Experimental verification of bioheat transfer theories: measurement of temperature profiles around large artificial vessels in perfused tissue,” *Phys. Med. Biol.*, vol. 35, no. 7, pp. 905–923, Jul. 1990, doi: 10.1088/0031-9155/35/7/007.

[137] D. B. Rodrigues *et al.*, “Numerical 3D modeling of heat transfer in human tissues for microwave radiometry monitoring of brown fat metabolism,” *Proc. SPIE*, vol. 8584, Feb. 2013, doi: 10.1117/12.2004931.

[138] K. Khosla, L. Zhan, A. Bhati, A. Carley-Clopton, M. Hagedorn, and J. Bischof, “Characterization of Laser Gold Nanowarming: A Platform for Millimeter-Scale Cryopreservation,” *Langmuir*, vol. 35, no. 23, pp. 7364–7375, Jun. 2019, doi: 10.1021/acs.langmuir.8b03011.

[139] N. Manuchehrabadi *et al.*, “Improved tissue cryopreservation using inductive heating of magnetic nanoparticles,” *Sci. Transl. Med.*, vol. 9, no. 379, Mar. 2017, doi: 10.1126/scitranslmed.aah4586.

[140] E. M. Knavel and C. L. Brace, “Tumor Ablation: Common Modalities and General Practices,” *Tech. Vasc. Interv. Radiol.*, vol. 16, no. 4, pp. 192–200, Dec. 2013, doi: 10.1053/j.tvir.2013.08.002.

[141] G. Poggi, N. Tosoratti, B. Montagna, and C. Picchi, “Microwave ablation of hepatocellular carcinoma,” *World J. Hepatol.*, vol. 7, no. 25, pp. 2578–2589, Nov. 2015, doi: 10.4254/wjh.v7.i25.2578.

[142] D. Li, J. Kang, B. J. Golas, V. W. Yeung, and D. C. Madoff, “Minimally invasive local therapies for liver cancer,” *Cancer Biol. Med.*, vol. 11, no. 4, pp. 217–236, Dec. 2014, doi: 10.7497/j.issn.2095-3941.2014.04.001.

[143] M. P. Clausen, H. Colin-York, F. Schneider, C. Eggeling, and M. Fritzsche, “Dissecting the actin cortex density and membrane-cortex distance in living cells by super-resolution microscopy,” *J. Phys. Appl. Phys.*, vol. 50, no. 6, p. 064002, Jan. 2017, doi: 10.1088/1361-6463/aa52a1.

[144] C. M. O’Connor, J. U. Adams, and J. Fairman, “Essentials of cell biology,” *Camb. MA NPG Educ.*, vol. 1, p. 54, 2010.

[145] H. C. Chang *et al.*, “Composite Structured Surfaces for Durable Dropwise Condensation,” *Int. J. Heat Mass Transf.*, vol. 156, p. 119890, Aug. 2020, doi: 10.1016/j.ijheatmasstransfer.2020.119890.

[146] A. R. N. Bastos *et al.*, “Thermal Properties of Lipid Bilayers Determined Using Upconversion Nanothermometry,” *Adv. Funct. Mater.*, vol. 29, no. 48, p. 1905474, 2019, doi: 10.1002/adfm.201905474.

[147] C. E. Hagberg *et al.*, “Flow Cytometry of Mouse and Human Adipocytes for the Analysis of Browning and Cellular Heterogeneity,” *Cell Rep.*, vol. 24, no. 10, pp. 2746-2756.e5, Sep. 2018, doi: 10.1016/j.celrep.2018.08.006.

[148] M. C. Rajagopal, T. Man, A. Agrawal, G. Kuntumalla, and S. Sinha, “Intrinsic thermal interfacial resistance measurement in bonded metal–polymer

foils," *Rev. Sci. Instrum.*, vol. 91, no. 10, p. 104901, Oct. 2020, doi: 10.1063/5.0012404.

[149] M. C. Rajagopal *et al.*, "Materials-to-device design of hybrid metal-polymer heat exchanger tubes for low temperature waste heat recovery," *Int. J. Heat Mass Transf.*, vol. 143, p. 118497, Nov. 2019, doi: 10.1016/j.ijheatmasstransfer.2019.118497.

[150] M. D. Johnson, J. Völker, H. V. Moeller, E. Laws, K. J. Breslauer, and P. G. Falkowski, "Universal constant for heat production in protists," *Proc. Natl. Acad. Sci.*, vol. 106, no. 16, pp. 6696–6699, Apr. 2009, doi: 10.1073/pnas.0902005106.

[151] R. P. Chhabra, *CRC Handbook of Thermal Engineering*. CRC Press, 2017.

[152] S. Youssefian, N. Rahbar, C. R. Lambert, and S. Van Dessel, "Variation of thermal conductivity of DPPC lipid bilayer membranes around the phase transition temperature," *J. R. Soc. Interface*, vol. 14, no. 130, p. 20170127, May 2017, doi: 10.1098/rsif.2017.0127.

[153] J. A. Kenar, "The use of lipids as phase change materials for thermal energy storage," *Lipid Technol.*, vol. 26, no. 7, pp. 154–156, 2014, doi: 10.1002/lite.201400037.

[154] J. A. Tomko *et al.*, "Tunable thermal transport and reversible thermal conductivity switching in topologically networked bio-inspired materials," *Nat. Nanotechnol.*, vol. 13, no. 10, Art. no. 10, Oct. 2018, doi: 10.1038/s41565-018-0227-7.

[155] M. A. Ezzat, "Fractional thermo-viscoelastic response of biological tissue with variable thermal material properties," *J. Therm. Stress.*, vol. 43, no. 9, pp. 1120–1137, Sep. 2020, doi: 10.1080/01495739.2020.1770643.

[156] M. C. Rajagopal and S. K. Das, "Analyses of drag on viscoelastic liquid infused bio-inspired patterned surfaces," *J. Non-Newton. Fluid Mech.*, vol. 228, pp. 17–30, Feb. 2016, doi: 10.1016/j.jnnfm.2015.09.001.

[157] R. Prasher, "Thermal Interface Materials: Historical Perspective, Status, and Future Directions," *Proc. IEEE*, vol. 94, no. 8, pp. 1571–1586, Aug. 2006, doi: 10.1109/JPROC.2006.879796.

[158] S. D. Lubner, S. Kaur, Y. Fu, V. Battaglia, and R. S. Prasher, "Identification and characterization of the dominant thermal resistance in lithium-ion batteries using operando 3-omega sensors," *J. Appl. Phys.*, vol. 127, no. 10, p. 105104, Mar. 2020, doi: 10.1063/1.5134459.

[159] K. V. Valavala, K. D. Coulson, M. C. Rajagopal, D. Gelda, and S. Sinha, "Chapter 4 - Thermal Engineering at the Limits of the CMOS Era," in *Handbook of Thin Film Deposition (Fourth Edition)*, William Andrew Publishing, 2018, pp. 63–101.

[160] A. Gaitonde, A. Nimmagadda, and A. Marconnet, “Measurement of interfacial thermal conductance in Lithium ion batteries,” *J. Power Sources*, vol. 343, pp. 431–436, Mar. 2017, doi: 10.1016/j.jpowsour.2017.01.019.

[161] G. Kucsko *et al.*, “Nanometre-scale thermometry in a living cell,” *Nature*, vol. 500, no. 7460, Art. no. 7460, Aug. 2013, doi: 10.1038/nature12373.

[162] G. Baffou *et al.*, “Photoinduced Heating of Nanoparticle Arrays,” *ACS Nano*, vol. 7, no. 8, pp. 6478–6488, Aug. 2013, doi: 10.1021/nn401924n.

[163] P. Lee, K. K. Y. Ho, P. Lee, J. R. Greenfield, K. K. Y. Ho, and J. R. Greenfield, “Hot fat in a cool man: infrared thermography and brown adipose tissue,” *Diabetes Obes. Metab.*, vol. 13, no. 1, pp. 92–93, Jan. 2011, doi: 10.1111/j.1463-1326.2010.01318.x.

[164] W. D. van Marken Lichtenbelt *et al.*, “Cold-Activated Brown Adipose Tissue in Healthy Men,” *N. Engl. J. Med.*, vol. 360, no. 15, pp. 1500–1508, Apr. 2009, doi: 10.1056/NEJMoa0808718.

[165] M. C. Rajagopal and S. Sinha, “Design and analysis of magnetostrictive sensors for wireless temperature sensing,” *Rev. Sci. Instrum.*, vol. in review, 2021.

[166] C. A. Grimes and D. Kouzoudis, “Remote query measurement of pressure, fluid-flow velocity, and humidity using magnetoelastic thick-film sensors,” *Sens. Actuators Phys.*, vol. 84, no. 3, pp. 205–212, Sep. 2000, doi: 10.1016/S0924-4247(00)00306-X.

[167] D. Kouzoudis and C. A. Grimes, “The frequency response of magnetoelastic sensors to stress and atmospheric pressure,” *Smart Mater. Struct.*, vol. 9, no. 6, pp. 885–889, Nov. 2000, doi: 10.1088/0964-1726/9/6/320.

[168] D. Kouzoudis and C. A. Grimes, “Remote query fluid-flow velocity measurement using magnetoelastic thick-film sensors (invited),” *J. Appl. Phys.*, vol. 87, no. 9, pp. 6301–6303, Apr. 2000, doi: 10.1063/1.372686.

[169] C. A. Grimes, D. Kouzoudis, and C. Mungle, “Simultaneous measurement of liquid density and viscosity using remote query magnetoelastic sensors,” *Rev. Sci. Instrum.*, vol. 71, no. 10, pp. 3822–3824, Sep. 2000, doi: 10.1063/1.1315352.

[170] K. T. Loiselle and C. A. Grimes, “Viscosity measurements of viscous liquids using magnetoelastic thick-film sensors,” *Rev. Sci. Instrum.*, vol. 71, no. 3, pp. 1441–1446, Mar. 2000, doi: 10.1063/1.1150477.

[171] M. K. Jain, S. Schmidt, K. G. Ong, C. Mungle, and C. A. Grimes, “Magnetoacoustic remote query temperature and humidity sensors,” *Smart Mater. Struct.*, vol. 9, no. 4, pp. 502–510, Aug. 2000, doi: 10.1088/0964-1726/9/4/314.

[172] Y. Yamamoto, T. Makino, and H. Matsui, “Micro-positioning and actuation devices using giant magnetostriction materials,” in *Proceedings 2000 ICRA. Millennium Conference. IEEE International Conference on Robotics and*

Automation. Symposia Proceedings (Cat. No.00CH37065), Apr. 2000, vol. 4, pp. 3635–3640 vol.4, doi: 10.1109/ROBOT.2000.845298.

[173] M. J. Dapino, "On magnetostrictive materials and their use in adaptive structures," *Struct. Eng. Mech.*, vol. 17, no. 3_4, pp. 303–329, 2004, doi: 10.12989/sem.2004.17.3_4.303.

[174] F. Claeyssen, N. Lhermet, R. Le Letty, and P. Bouchilloux, "Actuators, transducers and motors based on giant magnetostrictive materials," *J. Alloys Compd.*, vol. 258, no. 1, pp. 61–73, Aug. 1997, doi: 10.1016/S0925-8388(97)00070-4.

[175] C. A. Grimes *et al.*, "Wireless Magnetoelastic Resonance Sensors: A Critical Review," *Sensors*, vol. 2, no. 7, Art. no. 7, Jul. 2002, doi: 10.3390/s20700294.

[176] A. García-Arribas, D. De Cos, J. Gutiérrez, and J. M. Barandiarán, "Selectable temperature sensitivity of the magnetoelastic resonance," *Sens. Actuators Phys.*, vol. 106, no. 1, pp. 111–116, Sep. 2003, doi: 10.1016/S0924-4247(03)00146-8.

[177] X. J. Zheng and L. Sun, "A nonlinear constitutive model of magneto-thermo-mechanical coupling for giant magnetostrictive materials," *J. Appl. Phys.*, vol. 100, no. 6, p. 063906, Sep. 2006, doi: 10.1063/1.2338834.

[178] K. Jin, Y. Kou, and X. Zheng, "A nonlinear magneto-thermo-elastic coupled hysteretic constitutive model for magnetostrictive alloys," *J. Magn. Magn. Mater.*, vol. 324, no. 12, pp. 1954–1961, Jun. 2012, doi: 10.1016/j.jmmm.2012.01.028.

[179] Y. Liang and X. Zheng, "Experimental researches on magneto-thermo-mechanical characterization of Terfenol-D," *Acta Mech. Solida Sin.*, vol. 20, no. 4, pp. 283–288, Dec. 2007, doi: 10.1007/s10338-007-0733-x.

[180] Y. Xiao, H.-M. Zhou, and X.-L. Cui, "Nonlinear resonant magnetoelectric coupling effect with thermal, stress and magnetic loadings in laminated composites," *Compos. Struct.*, vol. 128, pp. 35–41, Sep. 2015, doi: 10.1016/j.compstruct.2015.03.039.

[181] S. Vinogradov and J. L. Fisher, "New Magnetostrictive Transducers and Applications for SHM of Pipes and Vessels," presented at the ASME 2019 Pressure Vessels & Piping Conference, Nov. 2019, doi: 10.1115/PVP2019-94078.

[182] M. Wiercigroch, V. Vaziri, and M. Kapitaniak, "RED: Revolutionary Drilling Technology for Hard Rock Formations," presented at the SPE/IADC Drilling Conference and Exhibition, Mar. 2017, doi: 10.2118/184665-MS.

[183] A. L. Brody, "State of the art of active/intelligent food packaging," *Inst. Food Technol. Food Packag. Summit*, 2006.

[184] S. Li, A. Simonian, and B. A. Chin, “Sensors for Agriculture and the Food Industry,” *Electrochem. Soc. Interface*, vol. 19, no. 4, p. 41, Jan. 2010, doi: 10.1149/2.F05104if.

[185] G. Herzer, “Magnetic materials for electronic article surveillance,” *J. Magn. Magn. Mater.*, vol. 254–255, pp. 598–602, Jan. 2003, doi: 10.1016/S0304-8853(02)00930-7.

[186] C. Liang, S. Morshed, and B. C. Prorok, “Correction for longitudinal mode vibration in thin slender beams,” *Appl. Phys. Lett.*, vol. 90, no. 22, p. 221912, May 2007, doi: 10.1063/1.2745262.

[187] “A nonlinear constitutive model for Terfenol-D rods: Journal of Applied Physics: Vol 97, No 5,” Accessed: Aug. 20, 2020. [Online]. Available: https://aip.scitation.org/doi/10.1063/1.1850618.

[188] A. P. Thomas and M. R. J. Gibbs, “Anisotropy and magnetostriction in metallic glasses,” *J. Magn. Magn. Mater.*, vol. 103, no. 1, pp. 97–110, Jan. 1992, doi: 10.1016/0304-8853(92)90242-G.

[189] “Materials from Metglas®, Inc.,” *Metglas, Inc.* https://metglas.com/magnetic-materials/ (accessed Aug. 21, 2020).

[190] R. Schulz, N. Alexandrov, J. Tétreault, R. Simoneau, and R. Roberge, “Development and application of amorphous core-distribution transformers in Québec,” *J. Mater. Eng. Perform.*, vol. 4, no. 4, pp. 430–434, Aug. 1995, doi: 10.1007/BF02649303.

[191] G. H. Hayes, W. A. Hines, D. P. Yang, and J. I. Budnick, “Low field magnetic anisotropy in Metglas 2605 CO ribbons,” *J. Appl. Phys.*, vol. 57, no. 8, pp. 3511–3513, Apr. 1985, doi: 10.1063/1.335044.

[192] J. Zhai, S. Dong, Z. Xing, J. Li, and D. Viehland, “Giant magnetoelectric effect in Metglas/polyvinylidene-fluoride laminates,” *Appl. Phys. Lett.*, vol. 89, no. 8, p. 083507, Aug. 2006, doi: 10.1063/1.2337996.

[193] M. H. Kim, K. S. Lee, and S. H. Lim, “Magnetostriction measurements of metallic glass ribbon by fiber-optic Mach–Zehnder interferometry,” *J. Magn. Magn. Mater.*, vol. 191, no. 1, pp. 107–112, Jan. 1999, doi: 10.1016/S0304-8853(98)00310-2.

[194] B. Kundys, Y. Bukhantsev, H. Szymczak, M. R. J. Gibbs, and R. Zuberek, “Temperature dependence of saturation magnetostriction measured for Fe81Si3.5B13.5C2 amorphous films by a bending method based on the Villari effect,” *J. Phys. Appl. Phys.*, vol. 35, no. 11, pp. 1095–1098, May 2002, doi: 10.1088/0022-3727/35/11/301.

[195] Z. Turgut, H. Kosai, T. Bixel, J. Scofield, S. L. Semiatin, and J. Horwath, “Hysteresis loss analysis of soft magnetic materials under direct current bias conditions,” *J. Appl. Phys.*, vol. 117, no. 17, p. 17A508, May 2015, doi: 10.1063/1.4919228.

[196] S. R. Green and Y. B. Gianchandani, “Wireless Magnetoelastic Monitoring of Biliary Stents,” *J. Microelectromechanical Syst.*, vol. 18, no. 1, pp. 64–78, Feb. 2009, doi: 10.1109/JMEMS.2008.2008568.

[197] G. Engdahl, *Handbook of Giant Magnetostrictive Materials*. Elsevier, 2000.

[198] “CorTemp Sensor,” *HQ, Inc.* https://hqinc.net/home/cortemp/cortemp-products/cortemp-sensor/ (accessed Aug. 21, 2020).

[199] X. Chen, Y. Su, D. Reay, and S. Riffat, “Recent research developments in polymer heat exchangers – A review,” *Renew. Sustain. Energy Rev.*, vol. 60, pp. 1367–1386, Jul. 2016, doi: 10.1016/j.rser.2016.03.024.

[200] S. Sundar *et al.*, “Fouling modeling and prediction approach for heat exchangers using deep learning,” *Int. J. Heat Mass Transf.*, vol. 159, p. 120112, Oct. 2020, doi: 10.1016/j.ijheatmasstransfer.2020.120112.

[201] “Sensormatic APX sheet label anti-theft tag specifications.” https://storage.googleapis.com/sensormatic-ecomm/Product%20Docs/shop/ZLAPXS_EN_APX_Sheet_Label.pdf.

[202] J. Tang, S. R. Green, and Y. B. Gianchandani, “Scalable, high-performance magnetoelastic tags using frame-suspended hexagonal resonators,” *J. Micromechanics Microengineering*, vol. 24, no. 6, p. 065006, Apr. 2014, doi: 10.1088/0960-1317/24/6/065006.

[203] A. Viswanath, S. R. Green, J. Kosel, and Y. B. Gianchandani, “Metglas–Elgiloy bi-layer, stent cell resonators for wireless monitoring of viscosity and mass loading,” *J. Micromechanics Microengineering*, vol. 23, no. 2, p. 025010, Dec. 2012, doi: 10.1088/0960-1317/23/2/025010.

[204] D. E. Mouzakis, D. Dimogianopoulos, and D. Giannikas, “Contact-Free Magnetoelastic Smart Microsensors With Stochastic Noise Filtering for Diagnosing Orthopedic Implant Failures,” *IEEE Trans. Ind. Electron.*, vol. 56, no. 4, pp. 1092–1100, Apr. 2009, doi: 10.1109/TIE.2008.2007548.

[205] N. P. Oess, B. Weisse, and B. J. Nelson, “Magnetoelastic Strain Sensor for Optimized Assessment of Bone Fracture Fixation,” *IEEE Sens. J.*, vol. 9, no. 8, pp. 961–968, Aug. 2009, doi: 10.1109/JSEN.2009.2025575.

[206] C. A. Grimes, D. Kouzoudis, K. G. Ong, and R. Crump, “Thin-Film Magnetoelastic Microsensors for Remote Query Biomedical Monitoring,” *Biomed. Microdevices*, vol. 2, no. 1, pp. 51–60, Feb. 1999, doi: 10.1023/A:1009907316867.

[207] L. Ren, K. Yu, and Y. Tan, “Applications and Advances of Magnetoelastic Sensors in Biomedical Engineering: A Review,” *Materials*, vol. 12, no. 7, Art. no. 7, Jan. 2019, doi: 10.3390/ma12071135.

[208] V. Pepakayala, “Micromachined Magnetoelastic Sensors and Actuators for Biomedical Devices and Other Applications.,” University of Michigan, 2015.

[209] D. Geduldig and D. Junge, “Sodium and calcium components of action potentials in Aplysia giant neurone,” *J. Physiol.*, vol. 199, no. 2, pp. 347–365, 1968, doi: 10.1113/jphysiol.1968.sp008657.

[210] W. B. Veldhuis *et al.*, “In Vivo Excitotoxicity Induced by Ouabain, a Na+/K+-ATPase Inhibitor,” *J. Cereb. Blood Flow Metab.*, vol. 23, no. 1, pp. 62–74, Jan. 2003, doi: 10.1097/01.WCB.0000039287.37737.50.

[211] C.-S. Lim and B.-K. Kaang, “Partial anatomical and physiological characterization and dissociated cell culture of the nervous system of the marine mollusc Aplysia kurodai.,” *Mol. Cells Springer Sci. Bus. Media BV*, vol. 7, no. 3, 1997.

[212] M. F. Shuba, “The effect of sodium-free and potassium-free solutions, ionic current inhibitors and ouabain on electrophysiological properties of smooth muscle of guinea-pig ureter.,” *J. Physiol.*, vol. 264, no. 3, pp. 837–851, 1977, doi: 10.1113/jphysiol.1977.sp011697.

[213] Z. B. Andrews *et al.*, “UCP2 mediates ghrelin’s action on NPY/AgRP neurons by lowering free radicals,” *Nature*, vol. 454, no. 7206, Art. no. 7206, Aug. 2008, doi: 10.1038/nature07181.

[214] S. Diano and T. L. Horvath, “Mitochondrial uncoupling protein 2 (UCP2) in glucose and lipid metabolism,” *Trends Mol. Med.*, vol. 18, no. 1, pp. 52–58, Jan. 2012, doi: 10.1016/j.molmed.2011.08.003.

[215] B. Katz and R. Miledi, “The effect of temperature on the synaptic delay at the neuromuscular junction.,” *J. Physiol.*, vol. 181, no. 3, pp. 656–670, 1965, doi: 10.1113/jphysiol.1965.sp007790.

[216] A. D. Richardson, C. Yang, A. Osterman, and J. W. Smith, “Central carbon metabolism in the progression of mammary carcinoma,” *Breast Cancer Res. Treat.*, vol. 110, no. 2, p. 297, Sep. 2007, doi: 10.1007/s10549-007-9732-3.

[217] J. Bauer *et al.*, “Increased stiffness of the tumor microenvironment in colon cancer stimulates cancer associated fibroblast-mediated prometastatic activin A signaling,” *Sci. Rep.*, vol. 10, no. 1, Art. no. 1, Jan. 2020, doi: 10.1038/s41598-019-55687-6.

[218] J. S. Park *et al.*, “Mechanical regulation of glycolysis via cytoskeleton architecture,” *Nature*, vol. 578, no. 7796, Art. no. 7796, Feb. 2020, doi: 10.1038/s41586-020-1998-1.

[219] R. Piñol *et al.*, “Real-Time Intracellular Temperature Imaging Using Lanthanide-Bearing Polymeric Micelles,” *Nano Lett.*, Jul. 2020, doi: 10.1021/acs.nanolett.0c02163.

[220] C.-F. Liu *et al.*, “Ultra-sensitive hybrid diamond nanothermometer,” *ArXiv191212097 Cond-Mat Physicsquant-Ph*, Dec. 2019, Accessed: Sep. 04, 2020. [Online]. Available: http://arxiv.org/abs/1912.12097.

[221] A. Tymiński, E. Śmiechowicz, I. R. Martín, and T. Grzyb, “Ultraviolet- and Near-Infrared-Excitable LaPO4:Yb3+/Tm3+/Ln3+ (Ln = Eu, Tb)

Nanoparticles for Luminescent Fibers and Optical Thermometers," *ACS Appl. Nano Mater.*, vol. 3, no. 7, pp. 6541–6551, Jul. 2020, doi: 10.1021/acsanm.0c01025.

[222] T. Sugimura, S. Kajimoto, and T. Nakabayashi, "Label-Free Imaging of Intracellular Temperature by Using the O−H Stretching Raman Band of Water," *Angew. Chem.*, vol. 132, no. 20, pp. 7829–7834, 2020, doi: 10.1002/ange.201915846.

[223] K. Oyama *et al.*, "Single-cell temperature mapping with fluorescent thermometer nanosheets," *J. Gen. Physiol.*, vol. 152, no. 8, Aug. 2020, doi: 10.1085/jgp.201912469.

[224] S. Wang, P. Zhang, W. Liu, S. Guo, and Y. Zhang, "High-resolution magnetic nanoparticle temperature measurement method based on dual-frequency magnetic field excitation," *Meas. Sci. Technol.*, 2020, doi: 10.1088/1361-6501/abb9e6.

[225] J. Zhong, W. Liu, Z. Du, P. C. de Morais, Q. Xiang, and Q. Xie, "A noninvasive, remote and precise method for temperature and concentration estimation using magnetic nanoparticles," *Nanotechnology*, vol. 23, no. 7, p. 075703, Jan. 2012, doi: 10.1088/0957-4484/23/7/075703.

[226] J. Zhong, W. Liu, L. Kong, and P. C. Morais, "A new approach for highly accurate, remote temperature probing using magnetic nanoparticles," *Sci. Rep.*, vol. 4, no. 1, Art. no. 1, Oct. 2014, doi: 10.1038/srep06338.

[227] D. Issadore, C. Min, M. Liong, J. Chung, R. Weissleder, and H. Lee, "Miniature magnetic resonance system for point-of-care diagnostics," *Lab. Chip*, vol. 11, no. 13, pp. 2282–2287, Jun. 2011, doi: 10.1039/C1LC20177H.

[228] C. Bohris *et al.*, "Quantitative MR temperature monitoring of high-intensity focused ultrasound therapy," *Magn. Reson. Imaging*, vol. 17, no. 4, pp. 603–610, May 1999, doi: 10.1016/S0730-725X(98)00196-9.

[229] D. V. Hingorani, A. S. Bernstein, and M. D. Pagel, "A review of responsive MRI contrast agents: 2005–2014," *Contrast Media Mol. Imaging*, vol. 10, no. 4, pp. 245–265, 2015, doi: 10.1002/cmmi.1629.

[230] T. A. Balasubramaniam and H. F. Bowman, "Temperature Field Due to a Time Dependent Heat Source of Spherical Geometry in an Infinite Medium," *J. Heat Transf.*, vol. 96, no. 3, pp. 296–299, Aug. 1974, doi: 10.1115/1.3450195.

[231] M. H. Sharqawy, J. H. L. V, and S. M. Zubair, "Thermophysical properties of seawater: a review of existing correlations and data," *Desalination Water Treat.*, vol. 16, no. 1–3, pp. 354–380, Apr. 2010, doi: 10.5004/dwt.2010.1079.

[232] K. Arunachalam, P. F. Maccarini, O. I. Craciunescu, J. L. Schlorff, and P. R. Stauffer, "Thermal characteristics of thermobrachytherapy surface applicators for treating chest wall recurrence," *Phys. Med. Biol.*, vol. 55, no. 7, pp. 1949–1969, Mar. 2010, doi: 10.1088/0031-9155/55/7/011.

[233] K. A. Virtanen *et al.*, “Functional Brown Adipose Tissue in Healthy Adults,” *http://dx.doi.org/10.1056/NEJMoa0808949*, Dec. 2009, doi: 10.1056/NEJMoa0808949.

[234] A. M. Cypess *et al.*, “Identification and Importance of Brown Adipose Tissue in Adult Humans,” *http://dx.doi.org/10.1056/NEJMoa0810780*, Dec. 2009, doi: 10.1056/NEJMoa0810780.

[235] V. Vuksanović, L. W. Sheppard, and A. Stefanovska, “Nonlinear Relationship between Level of Blood Flow and Skin Temperature for Different Dynamics of Temperature Change,” *Biophys. J.*, vol. 94, no. 10, pp. L78–L80, May 2008, doi: 10.1529/biophysj.107.127860.

[236] “Terfenol-D - ETREMA Products, Inc.,” *TdVib, LLC*. http://tdvib.com/terfenol-d/ (accessed Aug. 21, 2020).

[237] M. B. Moffett, A. E. Clark, M. Wun-Fogle, J. Linberg, J. P. Teter, and E. A. McLaughlin, “Characterization of Terfenol-D for magnetostrictive transducers,” *J. Acoust. Soc. Am.*, vol. 89, no. 3, pp. 1448–1455, Mar. 1991, doi: 10.1121/1.400678.

[238] A. E. Clark and M. Wun-Fogle, “A new method of magnetostrictivity and magnetostriction measurement,” *IEEE Trans. Magn.*, vol. 25, no. 5, pp. 3611–3613, Sep. 1989, doi: 10.1109/20.42378.

[239] M. Brouha and J. van der Borst, “The effect of annealing conditions on the magneto-mechanical properties of Fe-B-Si amorphous ribbons,” *J. Appl. Phys.*, vol. 50, no. B11, pp. 7594–7596, Nov. 1979, doi: 10.1063/1.326769.

[240] A. Houzali, F. Alves, J. C. Perron, and R. Barrué, “A new technique for dynamic annealing of amorphous alloys using Joule effect with controlled mechanical tensile stress,” *Rev. Sci. Instrum.*, vol. 66, no. 9, pp. 4671–4675, Sep. 1995, doi: 10.1063/1.1145305.

[241] M. Mouhamad, C. Elleau, F. Mazaleyrat, C. Guillaume, and B. Jarry, “Physicochemical and Accelerated Aging Tests of Metglas 2605SA1 and Metglas 2605HB1 Amorphous Ribbons for Power Applications,” *IEEE Trans. Magn.*, vol. 47, no. 10, pp. 3192–3195, Oct. 2011, doi: 10.1109/TMAG.2011.2158295.